



저작자표시-비영리-변경금지 2.0 대한민국

이용자는 아래의 조건을 따르는 경우에 한하여 자유롭게

- 이 저작물을 복제, 배포, 전송, 전시, 공연 및 방송할 수 있습니다.

다음과 같은 조건을 따라야 합니다:



저작자표시. 귀하는 원저작자를 표시하여야 합니다.



비영리. 귀하는 이 저작물을 영리 목적으로 이용할 수 없습니다.



변경금지. 귀하는 이 저작물을 개작, 변형 또는 가공할 수 없습니다.

- 귀하는, 이 저작물의 재이용이나 배포의 경우, 이 저작물에 적용된 이용허락조건을 명확하게 나타내어야 합니다.
- 저작권자로부터 별도의 허가를 받으면 이러한 조건들은 적용되지 않습니다.

저작권법에 따른 이용자의 권리는 위의 내용에 의하여 영향을 받지 않습니다.

이것은 [이용허락규약\(Legal Code\)](#)을 이해하기 쉽게 요약한 것입니다.

[Disclaimer](#)

공학박사학위논문

**Membrane-based Chemomechanical
Transducer System for the Detection of
Molecular Interactions**

분자결합 측정을 위한 박막 화학기계변환 시스템

2014 년 2 월

서울대학교 대학원

기계항공공학부

최 준 규

분자결합 측정을 위한 박막 화학기계변환 시스템

Membrane-based Chemomechanical Transducer
System for the Detection of Molecular Interactions

지도교수 이 정 훈

이 논문을 공학박사 학위논문으로 제출함

2014 년 11 월

서울대학교 대학원

기계항공공학부

최 준 규

최준규의 공학박사 학위논문을 인준함

2013 년 12 월

위 원 장 : 조 맹 효 (인)

부위원장 : 이 정 훈 (인)

위 원 : 박 영 준 (인)

위 원 : 오 흥 범 (인)

위 원 : 김 태 송 (인)

Abstract

Membrane-based Chemomechanical Transducer System for the Detection of Molecular Interactions

Jun-Kyu Choi

School of Mechanical and Aerospace Engineering

Seoul National University

Biological and chemical events detection enabled by chemo-mechanical transduction brings forth a new era of development in genomics and proteomics. Chemo-mechanical transduction offers unique advantages such as label-free assay, real-time monitoring and the potential for a compact device. Various approaches towards chemo-mechanical transduction have been introduced depending on the structures, materials and the sensing mechanisms. Micro cantilevers have been the mainstream of chemo-mechanical transducer and detect a variety of useful reactions such as DNA hybridization, various antigen-antibody binding and even cellular binding. These approaches were, however, hardly realized into a compact device due to the bulky optical equipment and it has trouble at opaque analytes. In any of the cantilever-based approaches one of the most critical issues is the fact that the cantilever immersed in analyte, produces undesired motions and deformations due to the interaction with the fluidic flow and the nonspecific adsorption of the backside.

Membrane-based approaches have emerged in order to overcome these issues and also they have several advantages. In case of membrane based transducers, the detection surface is physically isolated from the sensing surface, so it can be easily adapted to various electronic readout techniques. Secondly, membrane structures are more robust and therefore can be easily functionalized and probed using commercially available printing techniques. Finally, isolated sensing surface is capable of handling both liquid and gas samples. Although previous membrane transducer demonstrated the chemo-mechanical transduction of various biomolecular interactions but there are reliable problems associated with membrane material. The polymer materials in wet environments make different torsion due to swelling and low melting temperature and the silicon material is vulnerable to crack the surface of thin film.

In this work, a highly reliable thin membrane transducer (TMT) system has been developed. The system lead to breakthrough applications in the fields of diagnostics, threat evaluation and gas sensors with the integrated platform of membrane sensor, capacitance measuring electronics and aptamer receptor. Most of all, the MEMS sensor fabricated with monolithic process bring high reliability about the system. The special feature of this membrane transducer is the first use of a silicon nitride membrane material which is highly chemical inertness, thermal stability and bio-compatibility. Sacrificial layer process, utilizing photoresist material, leads to uniform distance for the pair of electrodes and the dimple structure fabricated with one step increases the reliability of transducer. The process of double layer of photoresist for the electroplating is strictly developed to build up thick rigid electrode with low stress. Furthermore, the self-aligned

proximate shadow mask is developed to deposit exquisite reaction-gold surface on the membrane, 500 μm below the contact surface. Finally, the entire fabrication uses standard low temperature processes for CMOS integration.

One of the key challenges of the membrane-based chemo-mechanical transduction is effective suppression of external disturbance. This membrane transducer system utilizes common mode rejection technique to nullify the effects of major environment disturbances such as hydraulic pressure, temperature and even common chemistry. Parallel metal structures on the membrane transducer connect the mechanical sensor to the highly sensitive differential capacitive electronics. Furthermore, the printed circuit boards (PCB) are designed to realize compact membrane transducer system.

This thesis demonstrates the feasibility of bio-molecular detection with the membrane-based chemo-mechanical transducer system. The specially designed molecular structure of a DNA aptamer is achieved to sensitive detection of thrombin protein. 11-mercaptopundecanoic acid (MUA) molecules are immobilized on the reaction gold and this choice of molecule is very advantageous. Not only MUA can withstand harsh packaging conditions but it also help in rejecting ground noise signal due to its high grafting density. Through peptide bonding Maleimide molecule is attached to MUA for highly selective binding with thiolated end of the receptor aptamer. The grafting density of probe DNA aptamer has been optimized with respect to the length of linker molecule to increase the surface stress on the membrane. Furthermore, through the study of molecular chemistry, molecular

interaction use appropriate base buffers such as peptide bonding and aptamer buffer for epitope conformation.

The membrane transducer can detect a cation in the buffer without chemo-electrical signal and recognize thrombin protein. In the result of 500 nM thrombin experiments, the largest center deflection of membrane is 24 nm calculated with integrating the infinitesimal area element of capacitance electrode. The amount of deflections is 3.2~8 times higher than that predicted with the analysis of finite element simulation (ABAQUS), which could be due to incomprehensible effects. However, this membrane-based chemo-mechanical transducer system holds a promising future in bio-chemical detection and disease diagnosis.

Keywords: Chemo-mechanical transduction, thin membrane transduction, surface stress, molecular diagnosis, capacitive sensor, common mode rejection

Student Number: 2008-30201

Table of Contents

Abstract	i
Table of Contents	v
List of Tables	viii
List of Figures	ix
Chapter 1 Introduction	1
1.1 Introductory Remark	1
1.2 References	6
Chapter 2 Theoretical Background.....	9
2.1 Principle of Chemo Mechanical Transduction	1 1
2.1.1 Surface Stress	1 1
2.1.2 Thin Plate Theory.....	1 4
2.1.2.1 Small Deflection Theory	1 6
2.1.2.2 Large Deflection Theory	1 9
2.2 Chemo Mechanical Transducer.....	2 1
2.2.1 Cantilever Transducer	2 4
2.2.2 Membrane Transducer.....	2 8
2.3 Surface Sensitization Technique	3 2
2.3.1 Surface Sensitization	3 2
2.3.2 Molecular Immobilization on Solid Surface	3 4
2.3.3 Aptamer.....	3 6
2.3.4 Dissociation Constant.....	4 0
2.4 Reference	4 1

Chapter 3 System Design and Manufacturing.....	4 7
3.1 Thin Membrane Transducer	4 9
3.1.1 MEMS Fabrication.....	5 1
3.1.1.1 Sensor Design and Simulation	5 1
3.1.1.2 Double Layer of Photoresist.....	6 1
3.1.2 Sensitivity Enhancement.....	6 8
3.1.2.1 Fluorocarbon SAM Coating	6 8
3.1.2.2 Self-aligned Proximate Shadow Mask	7 0
3.1.3 MEMS Sensor Packaging.....	7 7
3.2 Receptor Molecular Structure	8 2
3.2.1 Self-Assembly Monolayer.....	8 3
3.2.2 Effect of Gold Surface.....	8 7
3.2.3 Molecular Immobilization.....	9 1
3.3 Capacitive Measurement System	9 6
3.3.1 Analogue to Digital Convertor	9 6
3.3.2 Capacitive Measurement Circuit.....	1 0 1
3.4 References	1 0 6
Chapter 4 Chemo-Mechanical Detection	1 1 0
4.1 Membrane Transducer System.....	1 1 0
4.1.1 Temperature Response	1 1 0
4.1.2 Pressure Response	1 1 2
4.2 Common Mode Rejection	1 1 4
4.3 Ion Detection with Membrane Transducer System	1 2 1
4.3.1 Chemo-Electrical Detection	1 2 1

4.3.2	Chemo-Mechanical Design	1 2 4
4.3.3	Cation Detection.....	1 2 6
4.4	Molecular Recognition with Aptamer Receptor.....	1 2 8
4.4.1	Thrombin Protein and Thrombin Binding Aptamer	1 2 9
4.4.2	Immobilization of Thrombin Binding Aptamer	1 3 1
4.4.3	Thrombin Protein Detection and FE Simulation.....	1 3 6
4.5	Reference	1 4 2
Chapter 5 Conclusion and outlook.....		1 4 5
5.1	Conclusion	1 4 5
5.2	Future Work	1 4 7
5.2.1	Sensitivity Enhancement with Gold Nano Rod.....	1 4 7
5.2.2	Sensitivity Compensation for Quantitative Detection.....	1 5 3
5.3	Reference	1 6 4
Appendix.....		1 6 5
A.	Data polishing	1 6 5
B.	Membrane deflection according to Capacitance change.....	1 6 8
C.	Dissociation Constant	1 7 1
D.	The code of sensitivity compensation factor.....	1 7 6
국문초록.....		1 8 1

List of Tables

TABLE 1. CONDITIONS OF PLATE THEORY FOR SMALL AND LARGE DEFLECTION..	1 4
TABLE 2. A VARIETY OF BINDING ASSAY USING CHEMO-MECHANICAL TRANSDUCTION	2 3
TABLE 3. THE CATEGORIZATION OF CHEMICAL BONDS.	3 3
TABLE 4. BENEFITS OF APTAMERS OVER ANTIBODIES.	3 8
TABLE 5. SIMULATION PARAMETER OF SQUARE SILICON NITRIDE MEMBRANE INDUCED BY ATTACHING THE RESIDUAL GOLD SURFACE REPRESENTING THE SURFACE STRESS OF MOLECULAR INTERACTION.	5 7
TABLE 6. 2 STEP SU-8 PROCESS FLOW FOR HIGH ASPECT RATIO.....	7 3
TABLE 7. MICROARRAY STANDARD RECIPE FOR WASHING.....	9 2
TABLE 8. MOLECULE INTERACTION EFFICIENCY WITH MEDIAN SIGNAL INTENSITY AFTER TARGET MOLECULE ARE INTERACTED WITH PROBE.....	9 5
TABLE 9. ASSAY PROTOCOL OF THROMBIN BINDING APTAMER.	1 3 3
TABLE 10. THE SENSITIVITY COMPENSATION FACTOR OF MEMBRANE TRANSDUCER	1 6 1
TABLE 11. THE CAPACITANCE OFFSET VALUE OF REFERENCE TRANSDUCER...	1 6 6
TABLE 12. THE THROMBIN DETECTION RESULT OF MEMBRANE-BASED CHEMOMECHANICAL TRANSDUCER SYSTEM.	1 7 2

List of Figures

FIGURE 1-1. COMPACT AND PORTABLE CHEMICAL AND BIOLOGICAL DETECTION SYSTEM NEED BROAD FIELD TECHNOLOGIES SUCH AS MEMS, CHEMISTRY, BIOLOGY, MECHANICS AND ELECTRONICS.	4
FIGURE 2-1. EQUILIBRIUM CURVATURES OF LIPID MONOLAYER WHICH IS DEPENDENT ON SURFACE FREE ENERGY IN A SPECIFIC ENVIRONMENT.	1 0
FIGURE 2-2. SURFACE STRESS: A TENSILE SURFACE STRESS (POSITIVE SURFACE STRESS) CONTRACTS THE TOP SURFACE OF A THIN PLATE INDUCING A CONCAVE CURVATURE; A COMPRESSIVE SURFACE STRESS (NEGATIVE SURFACE STRESS) EXPANDS THE TIP SURFACE OF A THIN PLATE INDUCING A CONVEX CURVATURE.	1 2
FIGURE 2-3. MEMBRANE DEFLECTIONS ARE CORRESPONDING TO THE APPLIED PRESSURES. FOR THE RADIUS OF AN ASSUMED CIRCULAR MEMBRANE IS EQUAL THE AREA OF SQUARE MEMBRANE WITH $\sqrt{((750)2/3.14)}$. ALSO THE SILICON NITRIDE IS 0.5 MM THICKNESS, 0.27 POISSON RATIOS, AND 310 GPa YOUNG'S MODULUS.	2 0
FIGURE 2-4. TRANSLATING BIOMOLECULAR RECOGNITION INTO NANOMECHANICS USING AN ARRAY OF MICRO-CANTILEVER[25].....	2 5
FIGURE 2-5. MAIN OPERATION MODES OF NANOMECHANICAL SENSORS: STATIC MODE. WHEN THE STATIC MODE IS USED, THE MEASUREMENT OF THE FULL CANTILEVER PROFILE, OR AT LEAST A REFERENCED Z POSITION, IS NEEDED FOR THE END-POINT ASSAY. THE DYNAMIC MODE CAN FOLLOW CHANGES IN THE ADDED MASS (I) AND ALSO CHANGES IN THE STIFFNESS (II). WHEN THE ADSORPTION IS RESTRICTED EITHER TO THE FREE-END OR TO THE CLAMPED END, BOTH CONTRIBUTIONS CAN BE DISENTANGLED[37]......	2 7
FIGURE 2-6. PARYLENE MICRO MEMBRANE-BASED CHEMOMECHANICAL TRANSDUCER: (A) LAYOUT OF A UNIT CELL ON THE SENSOR CHIP AND THE SENSOR CROSS-SECTION VIEW. (B) LAYOUT OF THE MICROFLUIDIC UNIT CELL. (C) THE MICRO FABRICATED SENSOR CHIP	

WITH A 3X3 ARRAY OF SENSOR UNIT CELLS. (D) CHIP WITH BONDED MICROFLUIDIC COVER. (E) UNIT CELL WITH LAYOUT FOR SINGLE ENDED CAPACITANCE MEASUREMENT. (F) UNIT CELL WITH LAYOUT FOR DIFFERENTIAL CAPACITANCE MEASUREMENT. (G) MAGNIFIED VIEW OF THE RELEASED MEMBRANE SENSOR.....	2 9
FIGURE 2-7. (100) SILICON PLATE DEVICE FOR CHEMOMECHANICAL TRANSDUCER SENSING MOLECULAR INTERACTION: (A) DEVICE CROSS SECTION USED FOR OPTICAL INTERFEROMETRY MEASUREMENTS, (B) PLATE DEFLECTION PROFILES FROM LINE A-B, AND (C) SCANNING ELECTRON MICROSCOPY OF EXPOSED SENSING SURFACE BEFORE Ti/AU SPUTTERING.	3 0
FIGURE 2-8. RESULTS OF DEFORMATION: (A) X-RAY DIFFRACTION SCAN 30 NM SPUTTERED AU LAYER (WITH 8 NM Ti LAYER), (B) MEASURED PLATE BENDING AT T=0, 200 AND 300 S (10S INTERVALS) PRIOR TO VAPOR EXPOSURE, (C) BENDING DURING 1-DODECANETHIOL VAPOR EXPOSURE AND (D) CALCULATED ΔW AS A FUNCTION OF $\Delta \Sigma S$ AND $W \Delta$	3 1
FIGURE 2-9. DETECTION IN WESTERN BLOTS. IN THE ORIGINAL BLOTTING TECHNIQUES, THE TARGET IS IMMOBILIZED ON THE SUPPORT WITH ADSORPTION.	3 5
FIGURE 2-10. THE SYSTEMATIC EVOLUTION OF LIGANDS BY EXPONENTIAL ENRICHMENT (SELEX).....	3 7
FIGURE 3-1. SCHEMATICS OF NORMAL STRESS AND SURFACE STRESS.....	4 8
FIGURE 3-2. MEMBRANE DEFORMATION DUE TO MOLECULAR REACTION.....	5 0
FIGURE 3-3. CONCEPT OF THE MICROMACHINED MEMBRANE CAPACITIVE SENSOR. ALL PART OF THE SENSOR IS INTEGRATED WITH MEMS FABRICATION TO MANUFACTURE UNIFORM PERFORMANCE.	5 2
FIGURE 3-4. THE CROSS-SECTIONAL VIEW OF MEMBRANE CAPACITIVE SENSOR WHICH UTILIZE A SILICON NITRIDE MEMBRANE FIXED ON ALL FOUR SIDES AND IS SUSPENDED WITH COMPOSITED METAL LAYERS.....	5 3

FIGURE 3-5. A CROSS-SECTIONAL VIEW OF MEMBRANE SENSOR (A) WITHOUT COMPENSATOR, THIS MEMBRANE CAN BE EASILY AFFECTED BY UNDESIRED NOISE SIGNAL, (B) WITH COMPENSATOR, COMMON NOISES SUCH AS TEMPERATURE AND ELECTRON CHARGE CAN BE REMOVED AT BOTH METAL LAYERS.....	5 5
FIGURE 3-6. ELECTRODE SHAPE AND SIZE SIMULATION ACCORDING TO SAME AREA ON THE SILICON NITRIDE MEMBRANE OF 400MM LENGTH SQUARE.....	5 7
FIGURE 3-7. BEAM MODEL AND MATERIAL PARAMETER FOR FEM SIMULATION. ALKANETHIOL PARAMETER [6].	5 8
FIGURE 3-8. INITIAL BUCKLING OF BEAM DUE TO RESIDUAL STRESS MISMATCH.....	5 9
FIGURE 3-9. SURFACE STRESS INDUCED MEMBRANE DEFLECTION. THE DEFLECTION DUE TO TENSILE STRESS IS SMALLER COMPARED TO CANTILEVER MODEL IS APPARENT IN THE SIMULATION RESULT.	6 0
FIGURE 3-10. SACRIFICIAL LAYER: (A) A PATTERNED SACRIFICIAL LAYER WITH DIMPLE STRUCTURES, (B) 3D PROFILE IMAGE OF SACRIFICIAL LAYER, (C) PLASMA DAMAGE OF SACRIFICIAL LAYER AND (D) CRACK PATTERN ON THE SACRIFICIAL LAYER DUE TO THERMAL DAMAGE.	6 1
FIGURE 3-11. FABRICATION PROCESS FLOW OF DOUBLE SACRIFICIAL LAYER.....	6 3
FIGURE 3-12. REDUCING VISCOUS DAMPING OF PERFORATED PLANAR MICROMECHANICAL STRUCTURES.	6 4
FIGURE 3-13. THE SCHEMATICS OF MEMBRANE TRANSDUCER: (A) CROSS-SECTIONAL VIEW, (B) CAPACITANCE ELECTRODE VIEW (C) LOWER ELECTRODE PAD CONNECTED WITH MEMBRANE ELECTRODE THROUGH ELECTRODE-BRIDGE AND (D) UPPER ELECTRODE WITH LOTS OF HOLES FOR PREVENTING AIR-FILM SQUEEZE DAMPING.....	6 5
FIGURE 3-14. OPTICAL IMAGE OF COMPLETELY FABRICATING MEMBRANE TRANSDUCERS	6 7
FIGURE 3-15. FLUOROCARBON FILM AND HYDROPHOBIC PROPERTY.	6 9
FIGURE 3-16. POLYMER THICKNESS AND HYDROPHOBICITY ACCORDING TO POLYMER DEPOSITION TIME.	7 0

FIGURE 3-17. SHADOW MASK HOLDER. THIS OXIDIZED METAL UTILIZES O-RINGS FOR SEIZING THE WAFER.	7 1
FIGURE 3-18. SCHEMATICS OF SHADOW MASK. A HIGH ACCURACY OF ALIGNMENT IN THE CLOSE PROXIMITY SHADOW MASK BETWEEN SENSOR AND SHADOW MASK IS ACHIEVED. THE SLOPE PILLAR FOR ALIGNMENT IS MADE OF POTASSIUM HYDROXIDE (KOH) ETCH.	7 2
FIGURE 3-19. FABRICATION PROCESS FLOW FOR THE SELF-ALIGNED SHADOW MASK USING SU-8.	7 5
FIGURE 3-20. OPTICAL IMAGE OF SELF-ALIGNED SHADOW MASK.	7 6
FIGURE 3-21. REACTION GOLD DEPOSITED WITH SELF-ALIGNED SHADOW MASK IS IN THE 500 MM DEPTH FROM THE WAFER SURFACE.	7 7
FIGURE 3-22. FIRST PROTOTYPE OF MEMBRANE TRANSDUCER SYSTEM: (A) MEMS SENSOR HOLDER WITH THE CIRCUITS OF MEASUREMENT, (B) THE GLASS HOLDER WITH TRANSDUCERS AND ELECTRODE LINES, (C) MEASUREMENT SET-UP AND (D) MICRO-FLUIDIC CHANNEL ON TOP OF THE PACKAGE.	7 9
FIGURE 3-23. (A) THE PCB CIRCUIT WITH STABLE DRIVING VOLTAGE LOGIC, (B) THE PCB MEMS SENSOR, (C) THE SECOND PCB NOISE PEAK TO PEAK 2 fF AND (D) 3 RD PCB PEAK TO PEAK NOISE 100 aF.	8 1
FIGURE 3-24. PHOTO IMAGE OF PACKAGED MEMBRANE-BASED CAPACITIVE TRANSDUCER SYSTEM.	8 1
FIGURE 3-25. CHANGE IN THE SURFACE STRESS BECAUSE EXPOSED GOLD SURFACE IS REACTED WITH IONS. (A) A SAM MODIFIED AU, (B) DEFECTIVE SAM LAYER, (C) BARE GOLD LAYER IN 100MM HClO ₄ AND (D) BARE GOLD LAYER IN 100 MM NaCl. THE CHANGE IN SURFACE STRESS VALUES ARE ARBITRARILY SET TO ZERO AT THE MOST NEGATIVE POTENTIAL.	8 4
FIGURE 3-26. FT-IR MEASURED SPECTRA OF AN 11-MUA SAM ON REACTION GOLD WITH THE POSITION OF THE CH ₂ STRETCH VIBRATIONS AT 2919 cm ⁻¹ AND 2850 cm ⁻¹ , RESPECTIVELY, INDICATE A WELL-DEFINED SAM. (A) ETHANOL WASHING (B) D.I	

WASHING AND (C) SPECTRAL MODE TABLE FOR ASSIGNMENTS OF 11-MUA SAMs ON Au (111)/MICA[17]. THE C=O STRETCH VIBRATION IS OBSERVED AT 1710 cm^{-1} . THE PEAK AT 1435 cm^{-1} IS DUE TO THE C-O-H DEFORMATION VIBRATION; THE FEATURE AT 1468 cm^{-1} IS ATTRIBUTED TO CH ₂ DEFORMATIONS.....	8 6
FIGURE 3-27. SEM IMAGE OF THE Au-COATED SiN _x CANTILEVER SHOWING THE SENSOR'S RECEPTOR SURFACE AND DEFLECTION DUE TO SURFACE STRESS INDUCED BY BINDING ALKANETHIOL MOLECULE ON THE GOLD SURFACE[19]	8 8
FIGURE 3-28. COMPARE THE STM IMAGES ($3\mu\text{M} \times 3\mu\text{M}$) OF (A) LARGE-GRAINED GOLD AND (B) SMALL-GRAINED GOLD, (C) REAL-TIME THICKNESS PROFILES OF THE DODECANETHIOL SAMs AND (D) THE SURFACE STRESS INDUCED DURING THE FORMATION OF DODECANETHIOL SAM ON GOLD-COATED CANTILEVERS[20].	8 9
FIGURE 3-29. DIFFERENT CONDITION OF EVAPORATING GOLD SOURCE DURING THE DEPOSITION OF GOLD LAYER AND THE AFM IMAGE OF GOLD SURFACE TO CHECK GRAIN SIZE.....	9 0
FIGURE 3-30. FLUORESCENCE RESULT AFTER MICROARRAY STANDARD WASHING.....	9 2
FIGURE 3-31. FLUORESCENCE RESULTS AFTER PBS AND DISTILLED WATER WASHING.....	9 3
FIGURE 3-32. FLUORESCENCE SCAN IMAGE AND SIGNAL INTENSITY AFTER (A) IMMOBILIZATION AND (B) PROTEIN INTERACTION.	9 4
FIGURE 3-33. SCHEMATICS OF MEMBRANE TRANSDUCER SYSTEM.[23].....	9 7
FIGURE 3-34. CDC SIMPLIFIED BLOCK DIAGRAM IN AD7746 CHIP.[24]	9 7
FIGURE 3-35. EQUIVALENT RESISTOR MODEL FOR SWITCHED CAPACITOR CIRCUIT.....	9 7
FIGURE 3-36. HIGH PASS FILTER (HPF) CIRCUIT.	9 9
FIGURE 3-37. P-SPICE SIMULATION OF MEASUREMENT CIRCUIT.....	9 9
FIGURE 3-38. SIMULATION RESULTS FOR STABLE CIRCUITS.	1 0 0
FIGURE 3-39. CURRENT VS. VOLTAGE CURVE BETWEEN GROUND AND LOWER ELECTRODES.	1 0 0
FIGURE 3-40. SCHEMATICS OF OVERALL MEASUREMENT SYSTEM INCLUDED WITH HARDWARE AND SOFTWARE.	1 0 2

FIGURE 3-41. CIRCUIT LAYOUT OF CAPACITIVE MEASUREMENT FOR THE THIN MEMBRANE TRANSDUCER SYSTEM.	1 0 3
FIGURE 3-42. DIFFERENTIAL CAPACITANCE MEASUREMENT SYSTEM.	1 0 4
FIGURE 3-43. WINDOW GRAPHICAL-USER-INTERFACE(GUI).	1 0 5
FIGURE 4-1. TEMPERATURE SIGNAL SINGLE SENSOR SIGNAL FROM 28 TO 38 DEGREE CELSIUS	1 1 1
FIGURE 4-2. PRESSURE SENSITIVITY OF MEMBRANE TRANSDUCER. THIS MEMBRANE TRANSDUCER USE 100NM THICKNESS SILICON NITRIDE FILM.	1 1 3
FIGURE 4-3. PRESSURE SIGNAL OF THIN MEMBRANE TRANSDUCER SINGLE SENSOR SIGNAL FROM 1 TO 23 PASCAL.	1 1 3
FIGURE 4-4. TEMPERATURE DIFFERENTIAL SIGNAL FROM 27 TO 34 DEGREE CELSIUS ...	1 1 5
FIGURE 4-5. PRESSURE SIGNAL OF THIN MEMBRANE TRANSDUCER. DIFFERENTIAL SIGNAL FROM 1 TO 23 PASCAL.	1 1 6
FIGURE 4-6. THE COMMON MODE REJECTION OF PRESSURE(A) AND TEMPERATURE(B)..	1 1 7
FIGURE 4-7. DETECTION OF DIVALENT CATIONS WITH CANTILEVER BIOSENSORS IS BASED ON THE AFFINITY OF THESE IONS TO A VARIETY OF BIO-MOLECULES. (A) THE MECHANISM OF CANTILEVER DEFLECTION IS ORIGINATED FROM ELECTROSTATIC REPULSION. (B) CANTILEVER ARRAYS ARE DEFLECTED IN CONSTANT BUFFER TE FLOW FOLLOWED BY INJECTING VARIOUS CONCENTRATION OF $CaCl_2$. [6].....	1 1 9
FIGURE 4-8. CHEMICAL COMMON MODE REJECTION WITH NON-SPECIFIC ADSORPTION.	1 2 0
FIGURE 4-9. THE ELECTRIC FIELD DISTRIBUTION OF TWO OPPOSITELY CHARGED METAL PLATES. [7].....	1 2 1
FIGURE 4-10. CHEMO-ELECTRICAL MEASUREMENT.	1 2 2
FIGURE 4-11. THE SIGNAL OF CHEMO-ELECTRICAL TRANSDUCER.....	1 2 3
FIGURE 4-12. SCHEMATICS OF ELECTRIC FIELD SHIELDING BY DEPOSITING METAL LAYER.	1 2 4
FIGURE 4-13. EXPERIMENTAL RESULT OF ELECTRIC FIELD SHIELDING WITH METAL LAYER.	1 2 5

FIGURE 4-14. NEGATIVE CHARGE MOLECULE IMMOBILIZATION AT THE DEPOSITED REACTION GOLD ON THE BACKSIDE OF MEMBRANE.	1 2 7
FIGURE 4-15. NEGATIVE ELECTROSTATIC FORCES ARE RELEASED BY ADDING CATION CHARGE ON THE BUFFER.	1 2 7
FIGURE 4-16. THROMBIN PROTEIN WHICH IS COAGULATION FACTOR II. THE STRUCTURE OF HUMAN THROMBIN IN COMPLEX WITH THE INHIBITOR HIRUDIN. [11].....	1 3 0
FIGURE 4- 17. G-TETRADE STRUCTURES IN THE PRESENCE OF K AND NA CATION, AND THROMBIN BINDING APTAMER (TBA)[16].....	1 3 0
FIGURE 4-18. CONFIRM THE MOLECULAR IMMOBILIZATION WITH LASER SCANNING FOR FLUORESCENCE DYE.....	1 3 4
FIGURE 4-19. HIGHLY STABLE THROMBIN PROTEIN PROBE STRUCTURE.....	1 3 5
FIGURE 4-20. EXPERIMENTAL SET UP FOR BIO MOLECULAR INTERACTION.	1 3 6
FIGURE 4-21. SPECIFIC MOLECULAR INTERACTION RESULT WITH ARRAY OF MEMBRANE TRANSDUCER TO REJECT COMMON NOISE.	1 3 7
FIGURE 4-22. THE CENTER DEFLECTION VERSE SURFACE STRESS. THE DIRECTION OF MEMBRANE DEFLECTION IS DECIDED WITH HYDRAULIC PRESSURES THAT CAUSE THE LARGE DEFORMATION.	1 3 8
FIGURE 4-23. QUALITATIVE, QUANTITATIVE MOLECULAR INFORMATION RESULT WITH MEMBRANE-BASED CHEMOMECHANICAL TRANSDUCER SYSTEM.	1 3 9
FIGURE 4-24. CAPACITANCE CALCULATION ACCORDING TO MEMBRANE DEFLECTION...	1 4 0
FIGURE 5-1. SIGNAL ENHANCEMENT APPROACH TO USE NANO STRUCTURES WHICH ARE MADE OF ANODIC ALUMINA OXIDE TEMPLATE.	1 4 8
FIGURE 5-2. FABRICATION PROCESS FLOW OF GNR ON SILICON NITRIDE MEMBRANE...	1 4 9
FIGURE 5-3. SEM IMAGES OF THE ANODIZED ALUMINUM OXIDE FOR NANO ROD TEMPLATE ON SUSPENDED MEMBRANE.....	1 5 0
FIGURE 5-4. SEM IMAGES OF THE GNRS ON 100 NM-THICKNESS SUSPENDED Si3N4 MEMBRANE.	1 5 1

FIGURE 5-5. HIGH ASPECT RATIO OF GNRs AFTER REMOVAL OF AN AAO TEMPLATE (LENGTH: ~ 500 NM, DIAMETER: ~70NM, ASPECT RATIO: 7.14).	1 5 2
FIGURE 5-6. A 15 WAFER AVERAGE THICKNESS OF SILICON NITRIDE DEPOSITED BY LPCVD AT INTER-UNIVERSITY SEMICONDUCTOR RESEARCH CENTER AT SEOUL NATIONAL UNIVERSITY.	1 5 4
FIGURE 5-7. THIN MEMBRANE TRANSDUCERS ARE FABRICATED WITH MEMS TECHNOLOGY	1 5 5
FIGURE 5-8. INITIAL CAPACITANCE VALUE OF MEMBRANE TRANSDUCER.....	1 5 6
FIGURE 5-9. THE INITIAL CAPACITIVE VALUE AND CAPACITIVE CHANGE OF TRANSDUCERS APPLIED WITH A 40 BIAS-VOLTAGE. ALSO, THIS FOUR INCH WAFER MAP SHOWS THE DIFFERENCE OF SENSOR SENSITIVITY.	1 5 7
FIGURE 5-10. THE INITIAL CAPACITIVE VALUES OF THE MEMBRANE TRANSDUCER AFTER THE PACKAGING WITH PCB.....	1 5 8
FIGURE 5-11. THE CHANGE OF CAPACITIVE VALUE APPLIED WITH THE BIAS VOLTAGE OF 40V.	1 5 9
FIGURE 5-12. THE NORMALIZED CAPACITIVE CHANGES ARE INDUCED DUE TO THE ELECTROSTATIC FORCE OF THE APPLIED VOLTAGES.....	1 6 0
FIGURE 5-13. THE COMPENSATION DATA OF CAPACITANCE CHANGE ACCORDING TO THE APPLIED VOLTAGE.	1 6 2
FIGURE 5- 14. THE SENSITIVITY OF MEMBRANE TRANSDUCER IS CONFIRMED BY CHANGING AC LEVEL VOLTAGE ON THE CAPACITIVE MEASUREMENT SYSTEM.....	1 6 3
APPENDIX 1. THE RAW DATA GRAPH IS ORIGINAL OF FIGURE 4-21	1 6 5
APPENDIX 2. SCHEMATICS OF CAPACITANCE CALCULATION	1 6 8
APPENDIX 3. THE INFINITESIMAL AREA OF CURVED MEMBRANE.....	1 6 9
APPENDIX 4. THE CURVE FITTING OF SQUARE ERROR VS. KD VALUE.....	1 7 3
APPENDIX 5. THE CURVE FITTING WITH EXPERIMENTAL RESULT AT THE DISSOCIATION CONSTANT OF 26 NM.....	1 7 3

APPENDIX 6. REPEAT EXPERIMENTAL RESULT AND LARGE DYNAMIC RANGE OF MEMBRANE

TRANSDUCER 1 7 4

Chapter 1

Introduction

1.1 Introductory Remark

Chemo-mechanical transduction for biological and chemical events open up a new horizon for the expanding applications of diagnostics, drug discovery, security and threat evaluation. Although DNA and protein analysis are mature technologies, they usually utilize extrinsic labels which require expensive detection equipment to decide if the label is present after DNA-DNA hybridization or antigen-antibody binding. These works can be carried out on a chip platform without the use of exogenous labels. Micro- and nanometer scale cantilevers have been mainly used for those purposes. The micro cantilever and polymer demonstrated surface stress change caused by a specific bio molecular interaction such as self-assembled monolayer formation[1], DNA hybridization[2], antigen-antibody binding[3] and cellular binding[4]. These approaches are, however, hardly realized into a compact device due to the bulky optical detection equipment and it has trouble with various selectivity performance and robustness[5]. Although micro cantilever provides a viable alternative to resonant mass sensing techniques, the surface stress sensing mechanism is fundamentally different with membrane technology, where the resonance frequency detection decides the change of adsorption mass on the

resonator[6]. For sensing surface stress, thin membrane transducer on the other hand has several advantageous characteristics. Firstly, shell structures are more robust and stable than cantilever beams, but it is very sensitive to surface reaction[7], therefore, can be easily functionalized and probed by using commercially available printing techniques[8]. Secondly, the detection surface is physically isolated from the electrical sensing surface, which can be easily used for low-noise precise capacitance measurement technology [9]. Also, the isolated surface is a diverse platform which is accessible by both liquid and gas samples. Finally, electric measurement of sensing structure can readily be scaled and multiplexed with each reaction chamber. [10, 11]

In the previous research [12-14], a polymer based thin membrane transducers is introduced to show the possibility of bio molecular detection. To improve the lower sensitivity of the membrane transducer compared to cantilever type transducer, polymer material which has lower rigidity stiffness is used. The advantage of low rigidity stiffness is offset by the decrease of reliability in wet environments and fabrication uniformity compared with micro machined materials; silicon oxide, poly silicon, and silicon nitride. In addition to difficulties in fabricating a completely integrated device with polymer membrane, polymer based transducer has issues in the packaging of fluidic channel and measurement circuits because of high flexibility and low melting point. The reliability of chemical and biological diagnosis is crucial for commercial products, as reliability often dominates the device designs. MEMS devices are core products in future integrated systems which miniaturization and advanced functionalities are inevitable described in figure 1-1.

Here we report a highly reliable chemo-mechanical transducer system consisting of a MEMS fabricated membrane transducer, autonomously designed receptor molecule and capacitive measurement system. A fully integrated thin membrane transducer is developed by using micro machined technology with silicon nitride membrane material that is inert to chemical interaction and commonly used in MEMS sensors. This integrated membrane transducer has a sensing surface, analyte reaction chamber, and read out structure which are composed of seven layers which are made of integration with surface and bulk micromachining. These layers of transducer are composed of silicon substrate, membrane, molecule reaction gold, lower electrode, spacer, upper electrode and electrode contact pad layers. Every component helps enhance the quality of sensor systems. In addition, the integration enables a breakthrough application in the areas of genetics, diagnostics, threat evaluation, and acoustic sensors. Using the thin membrane transducer, we develop a chemo-mechanical transducer system integrated with specially designed components such as receptor structure, reaction chamber and differential capacitive measurements. The thin membrane transducer system consists of an array of transducers that are working identically at common disturbances such as hydraulic pressure, heat fluctuation and chemical adsorptions. Common mode rejection is a handy tool used in differential measurement in order to distinguish the signals from the specific molecular recognition and increase the sensitivity of detection.

Using the sensor system, we also report the chemo mechanical detection to identify bio-molecular interactions, which induce surface stress change that ultimately leads to membrane deflection. The ultra-sensitive detection of thrombin protein is

achievable with differential capacitive sensing which the limit of detection is 10pM with the use of a DNA aptamer. Importantly, this aptamer based probe assay platform offers valuable attributes short detection time (a few hundred seconds), optimal immobilization density, and dry condition durability[15, 16]. In order to enhance the surface sensitization, firstly, the immobilization of the probe molecule is optimized by controlling the grafting density of DNA aptamer probe in the mixture of 6-mercapto hexanol. Secondly, the contamination of functional layer is prevented via the immobilization of alkanethiol monolayer on gold surface. Lastly, the control of linker length and blocking of the extra functional groups on molecules are essential to achieve high selectivity. Moreover, the membrane sensor is reusable after 1 N NaOH is added to denature the protein on the membrane.

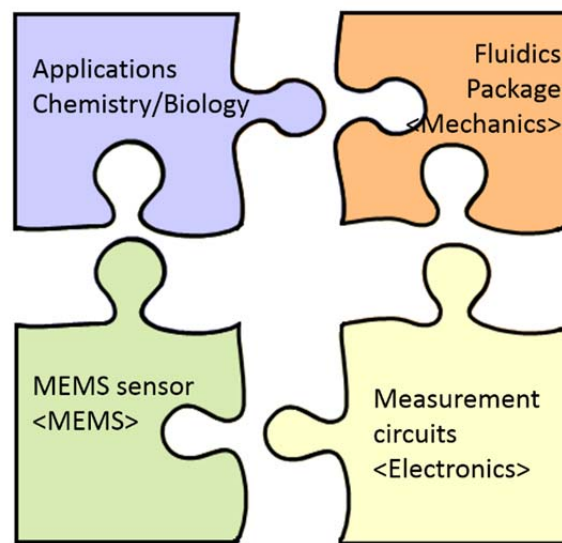


Figure 1-1. Compact and portable chemical and biological detection system need broad field technologies such as MEMS, chemistry, biology, mechanics and electronics.

The contents of this dissertation are organized in the following manner. Chapter 2 covers the summary of theoretical background knowledge for understanding surface stress sensor system, including prior work on surface stress sensors. The design, analysis and fabrication of thin membrane transducer as well as another electrochemical sensor are described in Chapter 3. The explanations on the receptor molecular structure and capacitive sensor system are also included in Chapter 3. In Chapter 4, a validation of sensor system is represented through the common mode rejection of temperature, pressure and non-specific chemical adsorption. Also the sensor system demonstrates the feasibility of molecular detections such as cation and protein recognition with the developed receptor structure. A summary of the important results of this work as well as future outlook are presented in Chapter 5.

1.2 References

1. Rüdiger Berger, E.D., Hans Peter Lang, Christoph Gerber, James K. Gimzewski, Ernst Meyer, Hans-Joachim Güntherodt, *Surface Stress in the Self-Assembly of Alkanethiols on Gold*. Science, 1997. **276**(27): p. 2021-2024.
2. J. Fritz, M.K.B., H. P. Lang, H. Rothuizen, P. Vettiger, E. Meyer, H.-J. Güntherodt, Ch. Gerber, J. K. Gimzewski, *Translating Biomolecular Recognition into Nanomechanics*. Science, 2000. **288**: p. 316-318.
3. Min Yue, J.C.S., Henry Lin, Ram Datar, Richard Cote, and Arun Majumdar, *Label-Free Protein Recognition Two-Dimensional Array Using Nanomechanical Sensors*. Nano Letters, 2008. **8**(2): p. 520-524.
4. Sang, S. and H. Witte, *A novel PDMS micro membrane biosensor based on the analysis of surface stress*. Biosens Bioelectron, 2010. **25**(11): p. 2420-4.
5. Ram Datar, S.K., Sangmin Jeon, Peter Hesketh, Scott Manalis, Anja Boisen, and Thomas Thundat, *Cantilever Sensors: Nanomechanical Tools for Diagnostics*, in *MRS BULLETIN*. 2009. p. 449-454.
6. Gil-Santos, E., et al., *Mass sensing based on deterministic and stochastic responses of elastically coupled nanocantilevers*. Nano Lett, 2009. **9**(12): p. 4122-7.
7. Carlen, E.T., et al., *Micromachined silicon plates for sensing molecular interactions*. Applied Physics Letters, 2006. **89**(17): p. 173123.
8. Wu, Z.C., K. Griffiths, H. R. Xu, J. Ma, X., *A novel silicon membrane-based biosensing platform using distributive sensing strategy and artificial neural networks for feature analysis*. Biomed Microdevices, 2012. **14**(1): p. 83-93.
9. A.M. Zapata , E.T.C., E. S. Kim¹, J. Hsiao¹, D. Traviglia¹, M.S. Weinberg, *BIOMOLECULAR SENSING USING SURFACE MICROMACHINED SILICON PLATES*, in *The 14th International Conference on Solid-State Sensors, Actuators and Microsystems, Lyon, France*. 2007. p. 831-834.

10. Lim, S.-H.S., et al., *Nano-chemo-mechanical sensor array platform for high-throughput chemical analysis*. Sensors and Actuators B: Chemical, 2006. **119**(2): p. 466-474.
11. Xu, T., et al., *Micro-machined piezoelectric membrane-based immunosensor array*. Biosens Bioelectron, 2008. **24**(4): p. 638-43.
12. Satyanarayana, S., D.T. McCormick, and A. Majumdar, *Parylene micro membrane capacitive sensor array for chemical and biological sensing*. Sensors and Actuators B: Chemical, 2006. **115**(1): p. 494-502.
13. Cha, M., et al., *Biomolecular detection with a thin membrane transducer*. Lab Chip, 2008. **8**(6): p. 932-7.
14. Tae June Kang, D.-K.L., Jwa-Min Nam, Yong Hyup Kim, *Multifunctional nanocomposite membrane for chemomechanical transducer*. Sensors and Actuators B: Chemical, 2010. **147**: p. 691-696.
15. Jayasena, S.D., *Aptamers: an emerging class of molecules that rival antibodies in diagnostics*. Clin Chem, 1999. **45**(9): p. 1628-50.
16. Schlecht, U., et al., *Comparison of antibody and aptamer receptors for the specific detection of thrombin with a nanometer gap-sized impedance biosensor*. Anal Chim Acta, 2006. **573-574**: p. 65-8.

Chapter 2. Theoretical Background

2.1 Principle of Chemo-Mechanical Transduction

2.1.1 Surface Stress

2.1.2 Thin Plate Theory

2.1.2.1 Small Deflection Theory

2.1.2.2 Large Deflection Theory

2.2 Chemo Mechanical Transducer

2.2.1 Cantilever Transducer

2.2.2 Membrane Transducer

2.3 Surface Sensitization Technique

2.3.1 Surface Sensitization

2.3.2 Molecular Immobilization on Solid Surface

2.3.3 Aptamer

2.3.4 Dissociation Constant

2.4 Reference

Chapter 2

Theoretical Background

Charles *et al*[1] demonstrated mechano-chemical transduction by using a long polymer strands, the trans and cis isomers of a 1,2-disubstituted benzocyclobutene. The polymer is subject to an ultrasound mechanical force caused by electrocyclic ring opening in a formally conrotatory and disrotatory process. During the chemical reactions, reactant molecules require certain amount of energy to overcome the energy barrier to allow their transformation. Usually, the energy is provided by in the form of heat, light, pressure or electrical potential, however mechanical force moving the reactants from ground state to excited state potential energy are facilitated to surmount the energy barrier. An opposite case is a chemomechanical transduction. Chemical reactions induce the mechanical deformation which is inspired of nature nanotechnology. For example, ion channels in cell membrane are transmembrane proteins that regulate ionic permeability on lipid bilayer membrane. The operation of this transmembrane protein is controlled by mechanical feedback induced surface stress due to chemical reaction[2]. In figure 2-1, a calcium ion channel can pump the ions out of the cell membrane when two gramicidin monomer molecules are attached. This process involves mechanical stress since the length of this dimer molecule is smaller than the membrane thickness. When the calcium level build an addition in cell membrane, the surface

stress of the curved lipid bilayer is decreased, and then the dimer will be separated into two monomers and stops functioning.

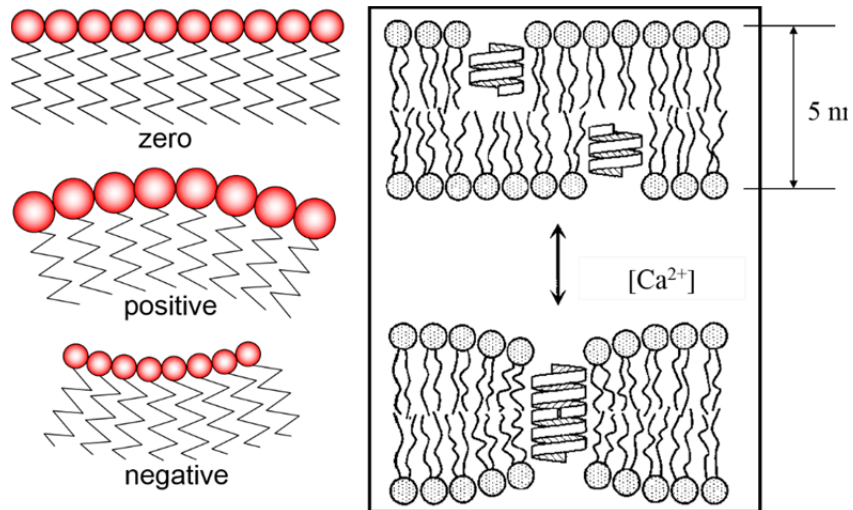


Figure 2-1. Equilibrium curvatures of lipid monolayer which is dependent on surface free energy in a specific environment.

2.1 Principle of Chemo Mechanical Transduction

AFM micro cantilevers are commonly used in various microscopy applications detecting electrostatic, spatial and electronic forces on the surfaces. Some researchers utilize the entire cantilever beam instead of the cantilever's tip as a probe for large range of detection [3]. The molecular interactions cause the cantilever to bend upon adsorption on the cantilever surface. Using the mechanism, physical, chemical and biochemical processes can be directly transduced into nano-mechanical responses due to the surface stresses from the energy of molecular interactions. The surface energies are first defined by Josiah Willard Gibbs as the amount of reversible work per unit needed to elastically stretch a pre-existing surface. Surface stress occurs when surface atoms or thin films undergo some dynamic molecular interaction processes resulting in a change in density. If the bond strength between surface atoms are stronger than that of substrate atoms, a tensile surface stress will be generated by the attractive forces that result in a concave surface curvature.

2.1.1 Surface Stress

A nano- and microscopic processes induces the surface stress of a macroscopic quantity. Recent mechanochemical interactions have been investigated with molecular reconstruction, interfacial mixing, and self-organization at solid surfaces have renewed the interest in the study of surface stress[4] [5]. In fact, surface stress arises when surface atoms go through some dynamic micro-structural processes

such as thermal reflow, high temperature deposition, and deposition of different stress materials. For example, surface atoms that tend to repel each other will collectively induce a compressive surface stress, resulting in a convex surface curvature. In contrast, when surface atoms are attracted to each other, a tensile surface stress will be resulted to form a concave surface curvature. Figure 2-2 illustrates the mechanism of compressive and tensile surface stress showing the surface curvature.

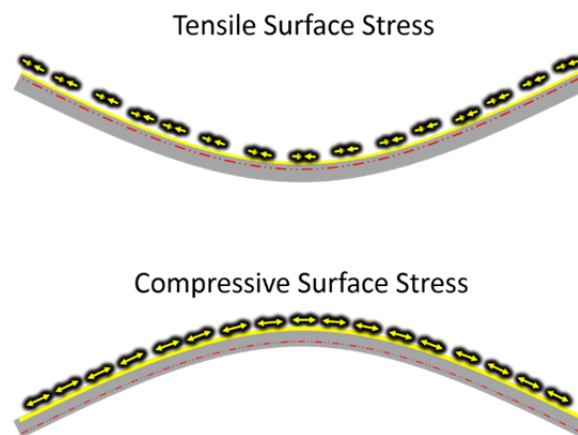


Figure 2-2. Surface stress: A tensile surface stress (positive surface stress) contracts the top surface of a thin plate inducing a concave curvature; a compressive surface stress (negative surface stress) expands the top surface of a thin plate inducing a convex curvature.

When a clean metal surface is deposited, the electrons of a metal replace themselves in response to the absence of atoms on the surface; the distribution of metal atoms near the surface is distinguished with what it is in the bulk of the material. If the charge density of metal molecules would be the same at the surface with the bulk state of the material, no surface stress would be generated. Gold

surface has inherent tensile surface stress because of the competition between the repulsive interactions between the filled d shells and an electron gas attraction from the mobile sp electrons[6]. Therefore, the increases of charge density result in an increase in tensile surface stress, which can be large enough to initiate surface reconstruction. In the case of Au (111), surface atoms are reconstructed to compensate for this increase in surface charge density so as to reduce the surface free energy. As a result, the surface accommodates an additional Au atom in a $(2\sqrt{3}\times\sqrt{3})$ reconstructed unit cell, which relieve the native tensile surface stress. The adsorption on a metal surface causes the change of electronic charge density which induce a compressive surface stress on the substrate resulted in deformation.[5]. In an opposite case, the tensile surface is similar interpretation occurring at Si(100) surface[7]. Shuttleworth has defined the surface stress equation in terms of the surface stress tensor σ_{ij} and surface energy, γ ; which named as the Shuttleworth equation[8].

$$\sigma_{ij} = \gamma\delta_{ij} + \frac{\partial\gamma}{\partial\varepsilon_{ij}} \quad \text{Equation 2.1.1-1}$$

In the equation, δ_{ij} is the Kronecker delta and ε_{ij} is the elastic strain tensor. On the liquid surface, surface stress is equal to surface energy, γ , in which the second term vanishes as there is no resistance acting the plastic deformation on the liquid surface. However, the surface energy is changed according to the change of energy during elastic stretching of a pre-existing surface at solid interfaces that make the change of the second term of equation 2.1.1-1.

2.1.2 Thin Plate Theory

Plate theory is suitable for the analysis of micromachined thin film diaphragms. In the plate theory, both small and large deflection has different characteristics, which conditions can be classified as shown in Table 1. Normally, membrane deflection belongs to the small deflection range due to a uniform axial surface stress. However, large initial deflection must be considered in order to obtain the change in differential surface stress due to a variety of reasons including imperfections of the membrane layer, a thin stressed film or adsorbed species on the surface, or deflections due to hydraulic gravity.

Table 1 Conditions of plate theory for small and large deflection

Theory	Conditions
Small deflection	Plate deflection ≤ 0.2 x plate thickness and/or Plate deflection ≤ 0.04 x plate diameter [9]
Large deflection	Plate deflection > 0.3 x plate thickness [10]

A classical plate theory of Timoshenko[11] explains that the mechanical behavior of a plate is dominated by the resistance of the deflection, by measuring the flexural rigidity, D:

$$D = \frac{Et^3}{12(1-\nu^2)} \quad \text{Equation 2.1.2-1}$$

, where E, t, and ν are young's modulus, plate thickness, and Poisson's ratio, respectively. For a circular plate with clamped edges, the initial deflection[11] is

$$w_i(r) = w_\delta \left[1 - \left(\frac{r}{a} \right)^2 \right]^2 \quad \text{Equation 2.1.2-2}$$

, where a is the plate radius and w_δ is the maximum initial deflection (at $r=0$).

The total deflection of both initial bending and a surface stress is[12, 13]

$$w(r) = \left[\frac{32w_\delta}{(\beta a)^2} \right] \left[\frac{J_0(\beta r) - J_0(\beta a)}{(\beta a)J_1(\beta a)} - \left(\frac{1}{2} \right) \left(1 - \left(\frac{r}{a} \right)^2 \right) \right] \quad \text{Equation 2.1.2-3}$$

, where J_0 and J_1 are Bessel functions of the first kind, $\beta^2 = \frac{\sigma_s}{D}$.

The change in differential surface stress is then

$$\Delta\sigma_s \approx \left(\frac{80}{11} \right) \gamma \left(1 + \frac{\sqrt{w_\delta(w_\delta + 4\Delta w)}}{w_\delta} \right) \quad \text{Equation 2.1.2-4}$$

, where $w_\delta < 0$, $\gamma = \frac{D}{a^2}$, and $\Delta\sigma_s = (\sigma_s)_{t=t_f} - (\sigma_s)_{t=0}$.

For applications such as label-free bio sensing, the precise calculation of the binding induced surface stress change may not be necessary; however, choosing a receptor layer with the appropriate functional group that generates a large change in surface stress upon binding is crucial to optimize the signal-to-noise ratio.

2.1.2.1 Small Deflection Theory

Kirchhoff used several assumptions to develop linear plate theory, which is known as Kirchhoff's Hypothesis. Small deflection theory is based on the Kirchhoff-Love Hypotheses[9]:

1. The plate material is elastic, homogenous, continuous, and isotropic
2. The bending deflections are small compared to the thickness of the plate. The slope of the deflected plate is also small; hence the square of the deflection is small.
3. Plane sections originally normal to the surface are presumed to be normal after bending. Hence shearing strain γ_{rz} and $\gamma_{\theta z}$ are negligible. The stresses σ_z are small and can be neglected.
4. The deflections of the plate are due to the displacements of points in the middle surface of the plate in a direction normal to the non-deflected middle surface.

The differential equation of a standard plate theory for the displacement $w(x,y)$ with an orthographic plate (here $E_x=E_y=E$) including residual stress[12]

$$D \frac{\partial^4 w}{\partial x^4} + 2H \frac{\partial^4 w}{\partial x^2 \partial y^2} + D_1 \frac{\partial^4 w}{\partial y^4} + Th \left(\frac{\partial^2 w}{\partial x^2} + \frac{\partial^2 w}{\partial y^2} \right) = P \quad \text{Equation 2.1.2.1-1}$$

With D (flexural rigidity), $D_1=D\nu$, $D_{xy}=Gh^3/12$ and $H=D_1+2D_{xy}$, the thickness h , Poisson's ratio ν and the homogeneous in-plane stress T . For a square membrane of area a^2 , this equation can only be solved numerically by satisfying the following conditions for a rigidly clamped plate. In the boundary condition, deflection and slope of plate edges are zero.

$$w(x = 0, a, y) = 0, w(x, y = 0, a) = 0,$$

$$\left. \frac{\partial w}{\partial x} \right|_{x=0, a, y} = 0, \left. \frac{\partial w}{\partial y} \right|_{x, y=0, a} = 0 \quad \text{Equation 2.1.2.1-2}$$

For closed form solution, the deflection of a square diaphragm of area A can be approximated by using a circular model with the same area[14]. This approximation offers a simpler calculation that comes with sufficient accuracy. For an isotropic circular, clamped diaphragm with existing plate deflection and subject to additional residual stress, the static deflection amplitude of pure plates (low tension) and pure membrane (high tension) can be expressed by

For Pure plate deflection,

$$w_{plate}(r) = \frac{pa^4}{64D} \left[1 - \left(\frac{r}{a} \right)^2 \right]^2 \quad \text{Equation 2.1.2.1-3}$$

For Pure membrane deflection,

$$w_{membrane}(r) = \frac{p}{\sigma t} \left[\frac{a^2 - r^2}{4} \right] \quad \text{Equation 2.1.2.1-4}$$

According to membrane theory, the residual stresses (σ) on the diaphragm are said to dominate the mechanical response. The total membrane deflection can be calculated with superposition solution that incorporates both plate and membrane theory

$$\frac{1}{w_{total}} = \frac{1}{w_{plate}} + \frac{1}{w_{membrane}} \quad \text{Equation 2.1.2.1-5}$$

So that the total deflection becomes

$$w_{total} = \frac{Pa^4}{64D} \cdot \frac{1}{1 + \frac{Th}{16D}(a^2 - r^2)} \left[1 - \left(\frac{r}{a} \right)^2 \right]^2 \quad \text{Equation 2.1.2.1-6}$$

In this equation, we can define corner stress, σ_c , which is a critical point for plate behavior.

$$\sigma_c = \frac{16D}{a^2t} \quad \text{Equation 2.1.2.1-7}$$

In my membrane, the value of corner stress is 0.4 MPa. When the stress on the plate is smaller than corner stress, the plate deflection is dominant with flexural rigidity, but when the stress of membrane is larger than corner stress, the membrane deflection is dominant with residual stress.

2.1.2.2 Large Deflection Theory

When the out-of-plane deflection of the plate is comparable to the thickness, the strain and the curvature throughout the plate are no longer uniform. The deformation including the coupling between axial and transverse motion is geometrically nonlinear. Timoshenko[11] explained the deflection of thin film with an approximate solution, based on the energy method, which is also suitable for small deflection range.

$$w = w_0(1 - r^2/a^2)^2 \quad \text{Equation 2.1.2.2-1}$$

Charles Bert et al[15], solve the constant (w_0) of equation into variable factor form including stretching body of membrane from its original erroneous form.

$$\frac{Pa^4}{Et^4} = 4.20 \frac{1}{(1-\nu^2)} \frac{w}{t} + 1.58 \frac{1}{(1-\nu^2)} \left(\frac{w^3}{t^3} \right) \quad \text{Equation 2.1.2.2-2}$$

Even though the above formulations for large deflections are quite useful, they do not take into account the built-in stress, which is commonly present in thin films. To explain the effects of built-in stress, we consider this equation;

$$\frac{Pa^4}{Et^4} = \frac{4\sigma a^2}{Et^2} \left(\frac{w}{t} \right) \quad \text{Equation 2.1.2.2-3}$$

Rearranging the above equation with equation 2.1.2.2-3, one can obtain

$$\frac{Pa^4}{Et^4} = \left[4.20 \frac{1}{(1-\nu^2)} + \frac{4\sigma a^2}{Et^2} \right] \frac{w}{t} + 1.58 \frac{1}{(1-\nu^2)} \left(\frac{w^3}{t^3} \right) \quad \text{Equation 2.1.2.2-4}$$

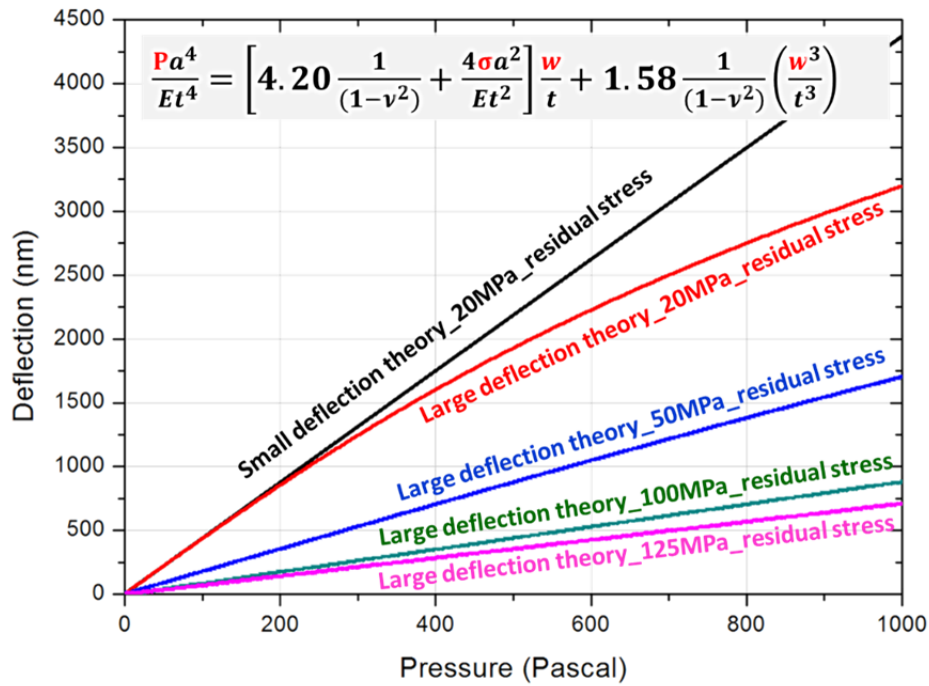


Figure 2-3. Membrane deflections are corresponding to the applied pressures. For the radius of an assumed circular membrane is equal the area of square membrane with $\sqrt{((750)2/3.14)}$. Also the silicon nitride is 0.5 μm thickness, 0.27 Poisson ratios, and 310 GPa young's modulus.

Figure 2-3 demonstrates the difference of membrane deflection between small and large deflection region due to applied pressure. Also, the built-in stress in other words residual stress highly affects the membrane deflection. These differences generally cooperate with lower the overall sensitivity of a membrane sensor. From graph, the sensitivity of a diaphragm to mechanical response rapidly decreases depending on the residual stress. Therefore, it is of paramount importance to minimize if not eliminate the thin film stress to have a sensitive sensor.

2.2 Chemo Mechanical Transducer

Chemical sensors could be classified into several main fundamental transduction modes: (a) thermal, (b) mass, (c) electrochemical, and (d) optical. Each of these detection modes is related with features that are complementary rather than competitive with each other, and the search of an “ideal transducer” has continued [16]. In a biology, mechanical interactions play a crucial role for determining motility and adhesion on the cellular scale, and governing transportation and affinity on the molecular scale[17]. During the last two decades, advances in microelectromechanical systems (MEMS) have facilitated development of sensors that involve transduction of mechanical energy and rely heavily on mechanical phenomena.

Most MEMS sensors detect the mechanical movements and deformations of their micro machined components such as single clamped suspended beams like as cantilevers, double clamped suspended beams like as bridges, and suspended diaphragms. Due to atomic force microscopy, a single clamped suspended beam, which name it as nano or micro cantilever is the first device for chemo-mechanical transducer[18]. A small cantilever is the central element in many mechanical biosensors that offers several advantages such as label-free detection, high sensitivity, and real-time monitoring for detecting bio-molecule interaction.

The biomechanical signal transduction has been observed in a variety of binding assay, as summarized in table 2. The sensor response to binding events can be

attributed to a variety of mechanisms. In case of DNA hybridization, one of the mechanisms causing stress on sensor surface is electrostatic force due to the highly negative charge of the molecule. When short length ssDNA chains are involved, under 15-mer, the negative charge on the oligonucleotide backbone produce electrostatic force, and this is the dominant factor. By the action of hybridization, formation of double-stranded structure, this force becomes even greater. [12] When examining this situation from a thermodynamic point of view, long chain ssDNA behave as a worm-like chain (WLC), effectively and double-stranded DNA are more like a rod. The conformational change produced by hybridization lead to reduced steric effect and induces tensile surface stress.[19] When we consider binding phenomena involved in antigen-antibody [19, 20] or aptamer-protein [21, 22] reactions, in most of these cases, there is a net charge effect which could lead to electrostatic force, however the steric effect involved is more dominant. These molecules are much bigger and have stretched conformations; also the net charge further enhances the steric effect after binding occurs, leading to a compressive surface stress.

Table 2. A variety of binding assay using chemo-mechanical transduction

Type	material	Dimension (um)	Molecule (concentration)	deflection (nm)	stress	Reason	Paper reference
Membrane	silicon	thickness=2 Circle R=400	dodecanethiol (98%, 400 μl)	33	compressive	surface free energy has been reduced	APL, 89, 173123, 2006
Membrane	Parylene	0.5 x 300 x 300	10 mJ/m ²	65	compressive	compressive stress	sensors and actuators B, 115, 2006, 494-502
Membrane	PDMS	2 x 500 x 500	16mer DNA (1μM)	20(6fF)	compressive	compressive stress	Lab chip, 2008, 8, 932-937
Membrane	PDMS	2 x 500 x 500	thrombin (500nM)	18fF	compressive		Lab chip, 2008, 8, 932-937
Cantilever	silicon	1 x 350 x 35	glucose oxidase-glucose (25mg/ml)	155	tensile		Anal. Chem. 2004, 76, 292-297
Cantilever	silicon	1 x 500 x 100	12mer DNA (2μM, 400nM, 80nM)	22,15,3	compressive	charge density from sugar-phosphate backbone	Science, 2000, 288, 316-318
Cantilever	silicon	1 x 500 x 100	12 mer DNA (1μM)	8			PNAS, 2002, vol.99. No.15, 9783-9788
Cantilever	silicon	1 x 350 x 30	MDTP (1mM)	250	tensile	π-π interaction of aromatic rings of pyridine in MDTP	Mendelev Comm., 2010, 20, 329-331
Cantilever	silicon	2 x 350 x 30	CuCl ₂ ·2H ₂ O (1mM)	600 @80min.	compressive	copper chelation	Mendelev Comm., 2010, 20, 329-332
Cantilever	silicon	3 x 350 x 30	histidine (1mM)	250 @70min.	compressive	repulsions of electronegative chloride atoms	Mendelev Comm., 2010, 20, 329-333
Cantilever		0.65 x 600 x 20	free prostate specific antigen(fPSA)	40@ 0.5 ng/ml, 70@ 1 ng/ml, 110@ 10 ng/ml			MRS Bulletin, vol34, june 2009

2.2.1 Cantilever Transducer

Atomic force microscopy was developed in 1986 from Gerd Binnig. It is able to detect atomic resolution surface with non-contact method by using van der Waals force between stylus and surface atom. Commercialization of AFM has initiated the development of micro-cantilevers for the surface stress sensors. In 1994, instead of the tip J. R. Barnes et al [18] utilize the whole body of cantilever beam as a probe to detect photo-thermal energy in the order of Pico joules (10^{-12} J). The cantilever-based sensors comprehend the transduction of chemical and physical interaction occurring on the surface into a mechanical deflection or resonant frequency shift of the cantilever depending on the respective working principle. The micro-cantilever generate a great deal of interest after it shows promising potential in the area of applications such as chemical/physical analysis and the detection of the freshness of food, charge, surface stress, IR radiation and heat flux. Therefore, some companies such as Concentris [23] and Veeco [24]. Especially, Fritz demonstrate biomolecular recognition can be translated into nanomechanical response [25] as described in figure 2-4. In this paper, the specific DNA hybridization is shown to take place on the surface of cantilever beam, surface stress that resulted in the deflection of cantilever inducing for differential sensing they used an array of sensors which are differently functionalized, which implicate a real molecular recognition signal rejecting common nonspecific adsorption of an array of cantilevers. Also, single mismatch oligonucleotides with hybridization of 12-mer complementary oligonucleotides are clearly detected implying that this chemo-mechanical transduction has improved the selectivity of molecular binding. The

specificity of this sensing layers determines the application with the difference of the chemical end-group present at the mono layer/gas/liquid interface.

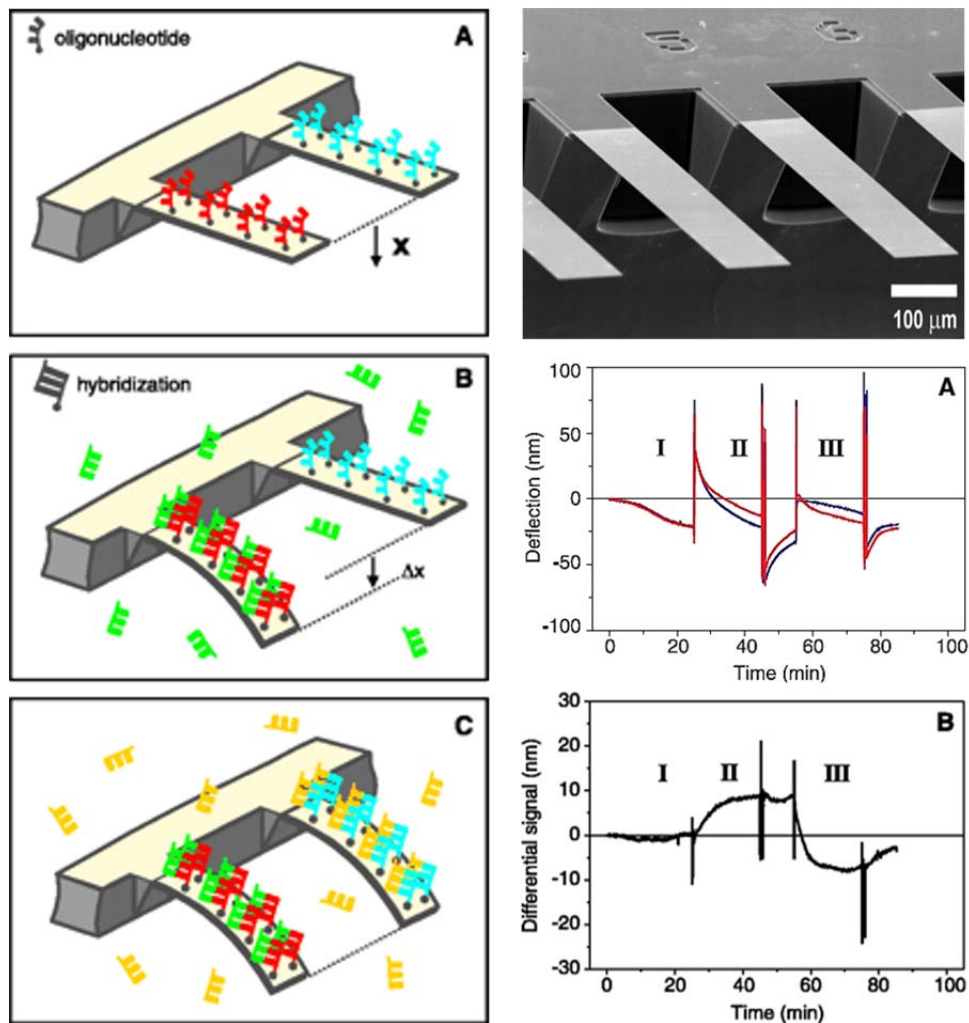


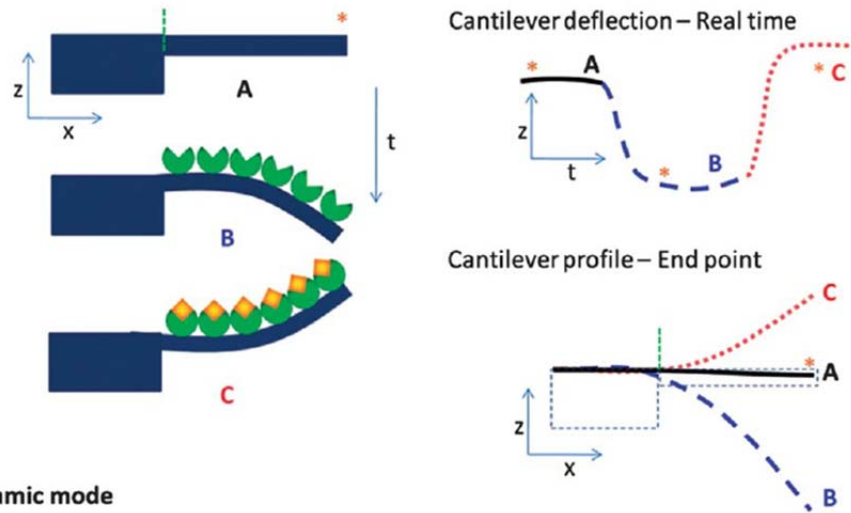
Figure 2-4. Translating biomolecular recognition into nanomechanics using an array of micro-cantilever[25].

The sensing layers of the functionalized SAM are both receptive sensitized to react with target molecules and responsive by allowing the transduction of the surface stress to the cantilever beam [26-28]. The micro-cantilever has been observed in a

variety of molecule binding applications such as detection of mercury gas[29], humidity sensing[30], explosive gas[31, 32], volatile organic compound(VOC) sensing[3, 33, 34], cell[35], and cocaine[36]. The nematic-states of molecule crystal induce the stress on the surface of cantilever beam. This surface stress owing to electrostatic repulsion or attraction, steric interactions, hydration and entropic effects make the deflection. Each parameter of these applications becomes more relevant according to the functionality of the particular device.

However, the micro-cantilevers are extreme flexible in a liquid that cause the undesirable deflection and deformation. Also, most cantilevers utilize the bulky optical measurement system that has the detecting limits of non-opaque analyte, and the back-side of cantilevers is vulnerable to nonspecific adsorption. T. Thundat *et al* [29] suggest oscillating mode for alternative measurement system depict in figure 2-5. The mechanism has potential of system miniaturization, but this technology has also limitations such as analyte viscosity, thermal noise and low sensitivity.

A) Static mode



B) Dynamic mode

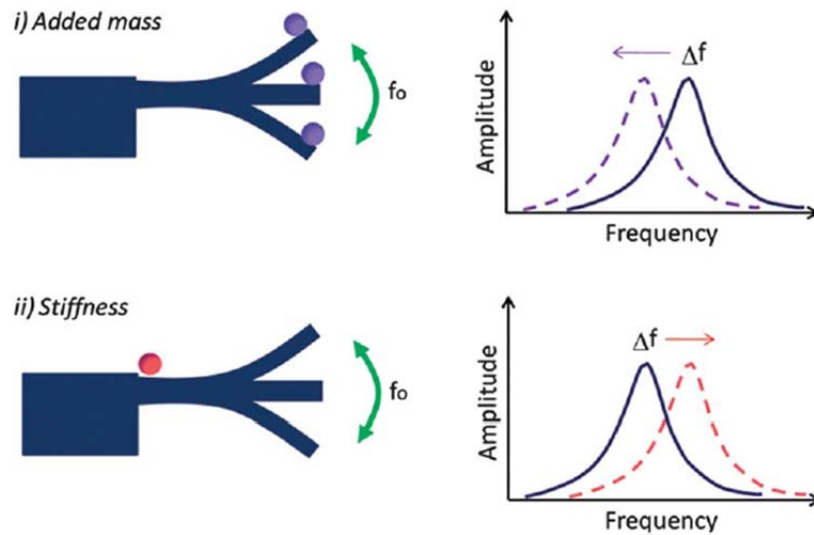


Figure 2-5. Main operation modes of nanomechanical sensors: static mode. When the static mode is used, the measurement of the full cantilever profile, or at least a referenced z position, is needed for the end-point assay. The dynamic mode can follow changes in the added mass (i) and also changes in the stiffness (ii). When the adsorption is restricted either to the free-end or to the clamped end, both contributions can be disentangled[37].

2.2.2 Membrane Transducer

Membrane base chemo-mechanical transducers overcome the challenge of cantilever as well as enhance the reliability. Membrane is the another configuration of structure member for detecting surface stress changes using silicon polymer bimorph to sensing VOC and humidity[38]. Membranes offer many advantages, some of which include easy electronic readout and sample isolation from detection systems.

Srinath Satyanarayana et al[39] publish the parylene micro membrane capacitive sensor for chemical and biological detection. This paper reports the design parameter with FE analysis simulation which demonstrates sensor response highly affected by gold coverage ratio comparing membrane area. The salient advantages of the membrane-based chemomechanical transducer: (i) is label-free; (ii) is a universal platform suitable for both chemical and biological sensing; (iii) uses electronic readout; (iv) has integrated microfluidics for addressing individual sensors on the chip; (v) is capable of handling both liquid and gas sample; (vi) is made using standard low temperature micro-fabrication processes; (vii) can readily be scaled and multiplexed. The sensor response to organic vapors like isopropyl alcohol and toluene are measured. They fabricate an array of sensor to spontaneously detect various gas molecules in figure 2-6 of optical images of the parylene membrane sensor. Although a novel membrane-based nanomechanical sensor for chemo-mechanical transduction uses the parylene material which has a low mechanical stiffness of polymers to increase the sensitivity, the parylene is

very susceptible of environmental noises such as fluidic pressure and high temperature.

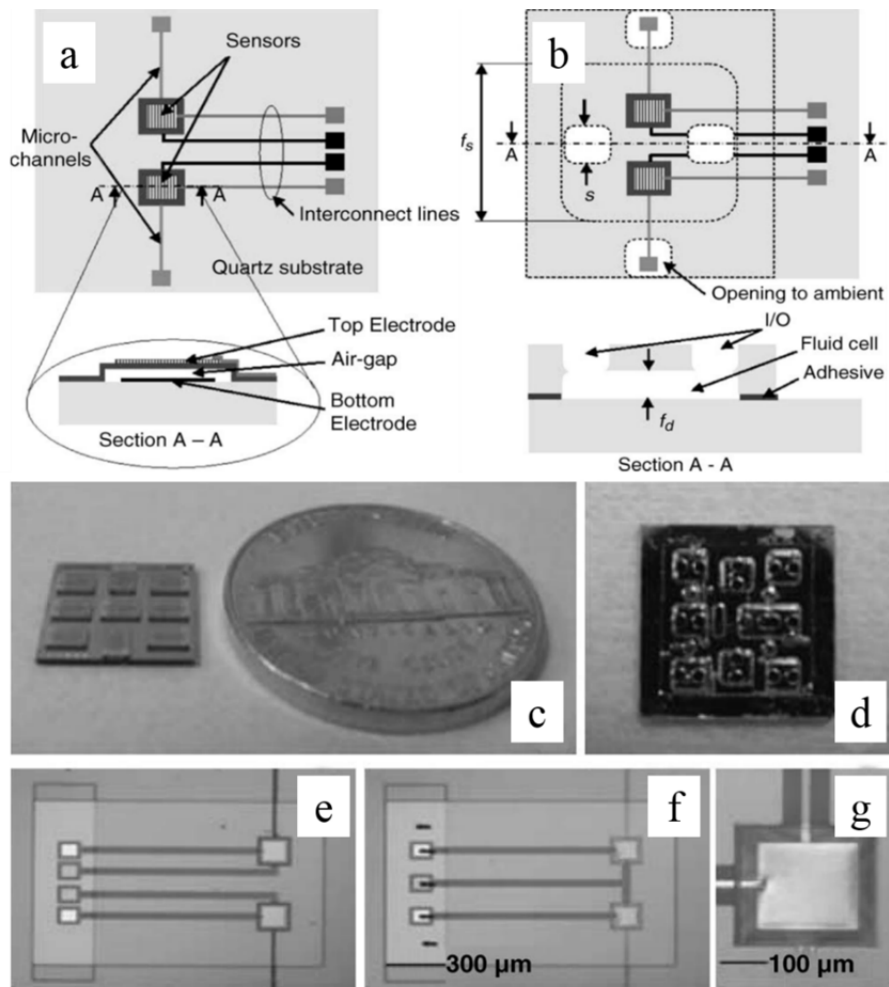


Figure 2-6. Parylene micro membrane-based chemomechanical transducer: (a) Layout of a unit cell on the sensor chip and the sensor cross-section view. (b) Layout of the microfluidic unit cell. (c) The micro fabricated sensor chip with a 3x3 array of sensor unit cells. (d) Chip with bonded microfluidic cover. (e) Unit cell with layout for single ended capacitance measurement. (f) Unit cell with layout for differential capacitance measurement. (g) Magnified view of the released membrane sensor.

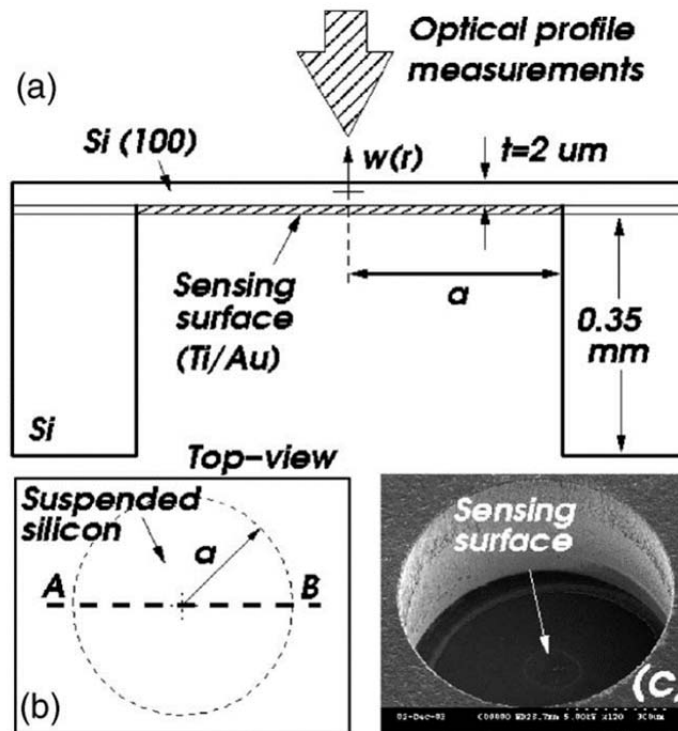


Figure 2-7. (100) silicon plate device for chemomechanical transducer sensing molecular interaction: (a) Device cross section used for optical interferometry measurements, (b) plate deflection profiles form line A-B, and (c) Scanning electron microscopy of exposed sensing surface before Ti/Au sputtering.

The Charles Stark Draper Laboratory group shows the micromachined silicon plate membrane sensor for sensing molecular interactions shown in figure 2-7. They mention that the ratio of deflection to a certain surface stress for membrane structures is smaller than cantilever structures by a factor of about 10 to 100 times[40-42], but the electronic displacement detection resolution exceeds 100 times over that of reported optical detection techniques[43, 44]. A thin suspended crystalline silicon circular plate is fabricated for surface stress sensor and the

surface stress changes associated with vapor phase chemisorption of a self-assembled monolayer with 1-dodecanethiol vapor shown in figure 2-8. The isolated face of the suspended silicon plate serves as the sensing surface treated with a receptor layer sensitive to a target molecule such as gold, antibody and aptamer. The chemisorption of an Alkanethiol on the gold surface make 361nm deformation after 300 second of the chemical evaporation which indicate compressive $0.72 \pm 0.02 \text{ Nm}^{-1}$ surface stress change. However, the silicon material is vulnerable to crack the surface of thin film.

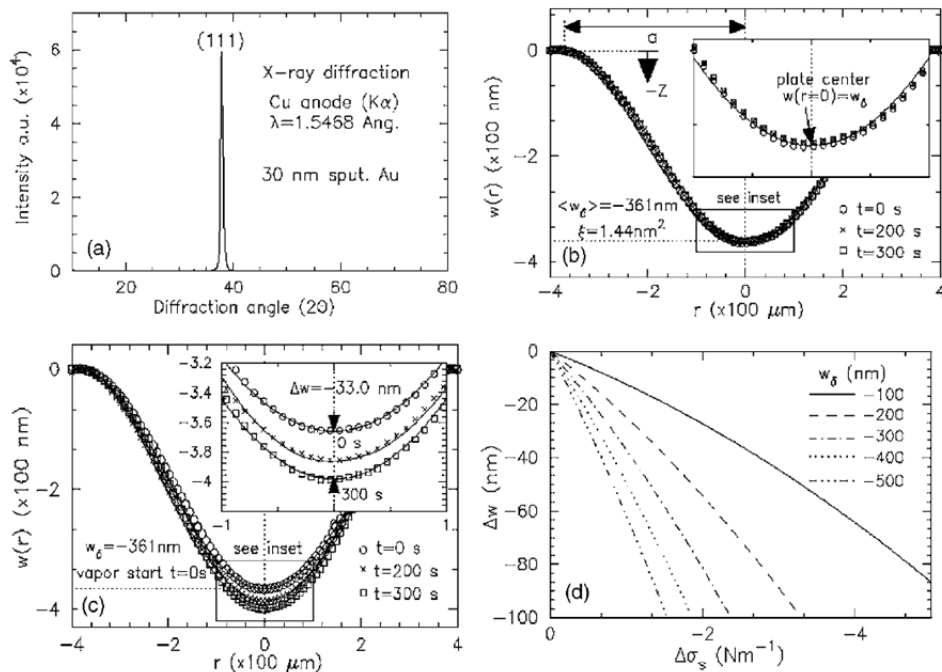


Figure 2-8. Results of deformation: (a) X-ray diffraction scan 30 nm sputtered Au layer (with 8 nm Ti layer), (b) measured plate bending At t=0, 200 and 300 s (10s intervals) prior to vapor exposure, (c) bending during 1-dodecanethiol vapor exposure and (d) calculated Δw as a function of $\Delta\sigma_s$ and w_δ .

2.3 Surface Sensitization Technique

Chemical and biological sensors require specific molecule for capturing target molecule which is called as receptor. The receptor layer on a biosensor provides specific binding sites for the target analytes such as molecules, proteins and cells. The receptor layers determine the sensor's characteristics such as selectivity, sensitivity and repeatability. The selective layer can be designed utilizing principles of molecular interaction; recognition, for example, DNA hybridization, antigen-antibody binding and aptamer epitope binding. Also, the sensing layers on the solid surface of biosensor can be achieved using molecular self-assembly monolayers for specific surface selectivity. Since the technology of surface functionalization, specificity and selectivity of biological receptors are too complex, sensor researchers have to understand molecule interaction of interesting target molecule and optimize the molecule structure of receptor.

2.3.1 Surface Sensitization

The specificity and sensitivity of biosensor systems are highly relative with the interfacial properties where bioactive species are immobilized. The design of molecular structures includes both the immobilization of the bio-receptor itself and the overall chemical preparation of the transducer surface. Also, the inertness of the surface limits the nonspecific adsorptions which induce the background noise of the sensor. Lastly, a robust interface improves the stability and the reliability of biosensor system. The optimum elaboration and the use of biosensor require the

background knowledge of the surface preparation and immobilization process of bio-species which is a detailed overview of the individual steps of surface modification; functionalization and immobilization of bio-receptors onto solid supports. Furthermore, the strength of intermolecular bonds is main factor for surface stress resulted in membrane deflection. The strength of bonds varies with different chemical bonds. Table 3 lists the categorization of chemical bond based on their strength.

Table 3. The categorization of chemical bonds. [45]

Strong	Covalent bonds & Antibonding	Sigma bonds: 3c-2e · bent bond · 3c-4e(Hydrogen bond, Dihydrogen bond, Agostic interaction) · 4c-2e Pi bonds: π backbonding · Conjugation · Hyperconjugation · Aromaticity · Metal aromaticity Delta bond: <u>Quadruple bond</u> · Quintuple bond · Sextuple bond Dipolar bond · Facticity
	Ionic bonds	Cation-pi interaction · Salt bridge
	Metallic bonds	Metal aromaticity
Weak	Hydrogen bond	Dihydrogen bond · Dihydrogen complex · Low-barrier hydrogen bond · Symmetric hydrogenbond · Hydrophilic
	Other noncovalent	Van der Waals force · Mechanical bond · Halogen bond · Auophilicity · Intercalation · Stacking · Entropic force · Chemical polarity
Other	Disulfide bond · Peptide bond · Phosphodiester bond	

2.3.2 Molecular Immobilization on Solid Surface

In the 1970's, biological analysis techniques such as ELISA [46], Southern blot [47] and western blot [48] based on the detection of solid supported biomolecular interactions are developed and still remain widely used. The principle is the specific recognition between a molecule in solution and a receptor molecule immobilized onto a solid support. This immobilization is concentrated on the specific area of surface which increases the receptor molecular density. According to the Langmuir isotherm model, the incensement of the density makes the detection easier and more sensitive on the surface and the recognition events to be detected are precisely localized. In conventional blotting techniques in figure 2-9, target molecule is immobilized on a solid to find a group of probe molecules in solution. This process is conducted in parallel tests. The number of individual experiments corresponds to the number of available probe molecules. By developing of detection technology, known probes attach a multiple surface to contact target solution as a single test, which is called as arrays. There are a few materials to directly immobilize biological molecules onto native solid surface. For satisfying specificities of biosensor application, particular surface chemistries are required to control the immobilization in order to maintain biological activity and minimize nonspecific adsorption. Thin organic films on mineral surface are widely used to foment the immobilization of biomolecules to solid surface [49]. For appropriate immobilization, the organic films have some characteristics such as reproducibility, homogeneity, thermal and chemical stability and chemical reaction performed during the immobilization or functionalization process. Various organic

molecules and chemical reactions are included depending on the characteristics of the solid surfaces such as hydroxyl-terminated surfaces by silane coupling agents and gold surfaces are modified by adsorption of alkanethiolate reagents.

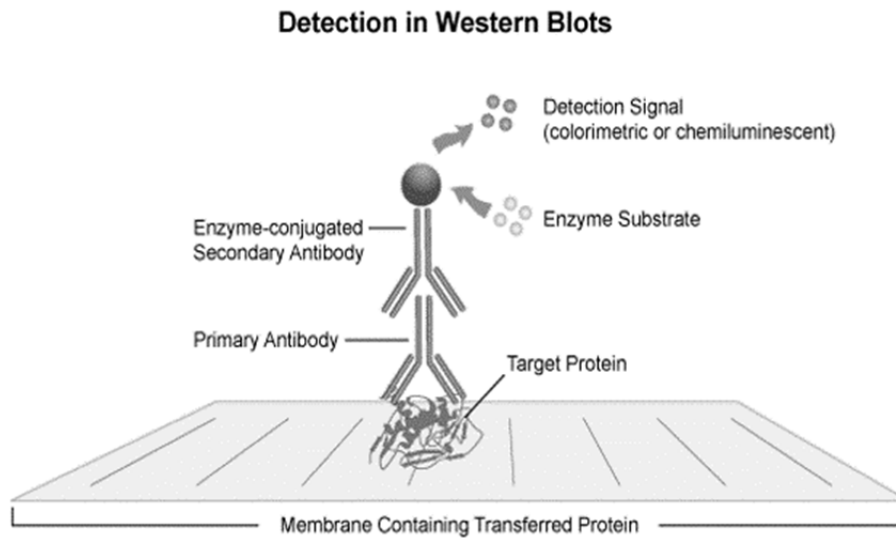


Figure 2-9. Detection in Western Blots. In the original blotting techniques, the target is immobilized on the support with adsorption.

2.3.3 Aptamer

Antibodies is the most popular receptor for molecule recognition of a wide range of applications, so antibodies are routinely used for clinics and also contribute the advancement of most diagnostic test. The development of the systematic evolution of ligands by exponential enrichment (SELEX) process, however, made possible an Aptamer for next generation of receptor with high affinity, low cost, and specificity. Although aptamers are mimic properties of antibodies in a variety of diagnostic formats, aptamer can detect small molecule such as ions, gases, and small particle like as cocaine which cannot detect with antibody receptor. Aptamers (synthetic antibodies) are (stable) single-stranded DNA, RNA, or peptide molecules capable of binding to its target antigen with high affinity and specificity. Aptamer have been discovered against a wide variety of target molecules from small organics to large proteins[50]. Compared with the bellwether antibody technology, aptamer research is still in its infancy, but it is progressing at a fast pace[51].

Aptamer that come out of a SELEX process are certain sequences containing the fixed sequences that were included to aid the amplification process. The SELEX process begins with a random sequence library obtained from combinatorial chemical synthesis of DNA as depicted in figure 2-10 [52]. The diversity of a library is related with the number of randomized nucleotide positions, which normally contain a 40-nucleotide random region represented by 1.2×10^{24} individual sequences ($4^{20} = 1.2 \times 10^{24}$). The success of finding unique and rare aptamer that interact with a target parallels the diversity of the libraries used. These

include peptide libraries used for phage display as well as the libraries made up of small organic molecules.

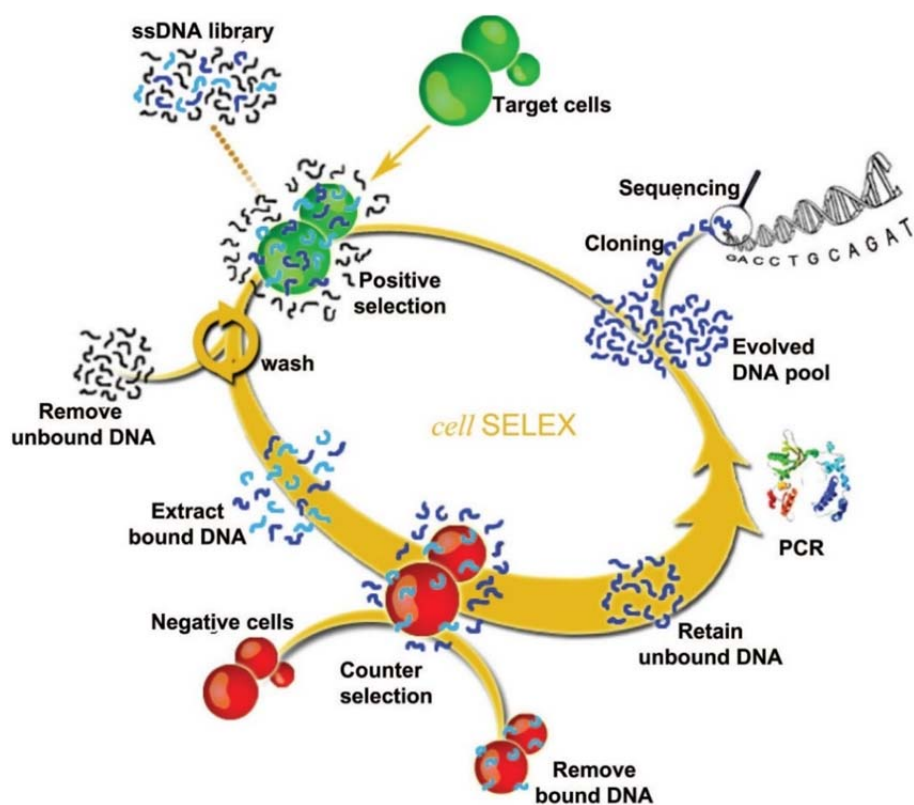


Figure 2-10. The systematic evolution of ligands by exponential enrichment (SELEX).

The binding analysis of enriching populations of the target molecules is carried to determine the progress of the enrichment of high-affinity binders. Once affinity saturation is achieved after several rounds of selection/amplification, the enriched library is cloned and sequenced to obtain the sequence information of each member. Usually, the majority of individual sequences, over 90%, in an enriched library are “winners”, aptamers that bind to the target used for selection. Once the sequence information has been obtained through the SELEX process, the desired aptamer

can be readily produced by chemical synthesis with low cost. For a given target molecule, these are two kinds aptamer, DNA and RNA. Since DNA lacks the 2' hydroxyl group of the RNA, they are quite difference in three-dimensional structure. In Table 4, I summarize the benefits of aptamers compared with antibodies and the yellow-colored rows detail special advantages of aptamers to recognize target molecule for transducer [53].

Table 4. Benefits of aptamers over antibodies.

	Aptamer	Antibody
Affinity	Low nM-pM	Low nM-pM
Specificity	High	High
Manufacturing	In vitro chemical process	In vivo biological system
Cost	Low	High
Target molecule	Wide: ions, small organic molecules, proteins, whole cells, toxic molecules, etc.	Narrow: only immunogenic compounds
Batch to batch variation	No	Big problem; Significant
Chemical modification	Easy	Limited
Thermal rigidity	Small and reversible	irreversible
Life time	Very long	Limited, storage on refrigerator

Therefore, aptamers have numerous advantages over antibodies to be useful tools in analytical, diagnostics and therapeutic applications. The most important characteristic of aptamers is its ability to bind their target molecules with high specificity[54].

2.3.4 Dissociation Constant

The binding process is initiated with long-range electrostatic interactions, leading to the approach and combining of the ligand to appropriate intermolecular interactions of the complementary binding surfaces. During the molecular interaction, reversible and non-covalent binding are indispensable steps in the most chemical and biological processes. Since binding interactions are so crucial a factor for understanding of molecular interaction, binding processes can be studied at the structural, equilibrium-thermodynamic, and kinetic levels. Normally, characterizing the strength of the dynamic binding equilibrium determines dissociation constants, K_D , which are experimentally determined quantities with units of molarity. For example, in two state reversible interactions, dissociation constants equal between ligand and receptor concentration that gives half-maximal binding.

In a simple two state model, binding equilibrium model can be used to approximate most simple, reversible and non-covalent binding interactions[55].



in which a complex $A_x B_y$ breaks down into x A subunits and y B subunits. The dissociation constant K_D , with units of molarity, is defined as

$$K_d = \frac{[A]^x [B]^y}{[A_x B_y]} \quad \text{Equation 2.3.4-1}$$

where $[A]$, $[B]$, and $[A_x B_y]$ are the concentrations of A, B, and the complex $A_x B_y$, respectively.

2.4 Reference

1. Hickenboth, C.R., et al., *Biasing reaction pathways with mechanical force*. Nature, 2007. **446**(7134): p. 423-427.
2. Lundbaek, J.A., A.M. Maer, and O.S. Andersen, *Lipid bilayer electrostatic energy, curvature stress, and assembly of gramicidin channels*. Biochemistry, 1997. **36**(19): p. 5695-701.
3. Lang, H.P., et al., *Nanomechanics from atomic resolution to molecular recognition based on atomic force microscopy technology*. Nanotechnology, 2002. **13**(5): p. R29-R36.
4. Ramirez, A.L.B., et al., *Mechanochemical strengthening of a synthetic polymer in response to typically destructive shear forces*. Nat Chem, 2013. **5**(9): p. 757-761.
5. Godin, M., *Surface Stress, Kinetics, and Structure of Alkanethiol Self-Assembled Monolayers*, in *Physics*. 2004, McGill University: Montreal Quebec.
6. Marks, V.H.a.L.D., *Competition between Pair-wise and Volume Forces at Noble Metal Surfaces* SURFACE SCIENCE, 1986. **165**(65).
7. Ibach, H., *The role of surface stress in reconstruction, epitaxial growth and stabilization of mesoscopic structures*. Surface Science Reports, 1997. **29**(5–6): p. 195-263.
8. SHUTTLEWORTH, R. *The Surface Tension of Solids*. in *Proceedings of the Physical Society. Section A*. 1950.
9. Finot, M. and S. Suresh, *Small and large deformation of thick and thin-film multi-layers: Effects of layer geometry, plasticity and compositional gradients*. Journal of the Mechanics and Physics of Solids, 1996. **44**(5): p. 683-721.
10. Ko, W.H. and W. Qiang. *Touch mode capacitive pressure sensors for industrial applications*. in *Micro Electro Mechanical Systems, 1997. MEMS '97, Proceedings, IEEE., Tenth Annual International Workshop on*. 1997.
11. Timoshenko, S., *Theory of plates and shells*. 1959, McGRAW-HILL classic textbook peissue.

12. Szilard, R., *Theory and Analysis of PLATES: Classical and Numerical Methods*. 1974, Engelwood Cliffs, NJ: Prentice-Hall.
13. Carlen, E.T., et al., *Micromachined silicon plates for sensing molecular interactions*. Applied Physics Letters, 2006. **89**(17): p. 173123.
14. Maisano, J., *More Advanced Models for Silicon Condenser Microphones*, in *92nd Convention of the Audio Engineering Society*. 1992: Vienna, Austria.
15. Martindale, C.W.B.a.J.L., *An Accurate, Simplified Method for Analyzing Thin Plates Undergoing Large Deflections*. American Institute of Aeronautics and Astronautics(AIAA) Journal, 1988. **26**(2): p. 235-241.
16. Nickolay V. Lavrik, M.J.S., and Panos G. Datskos, *Cantilever transducers as a platform for chemical and biological sensors*. Review Science Instruments, 2004. **75**: p. 2229.
17. J.L. Arlett, E.B.M.a.M.L.R., *Comparative advantages of mechanical biosensors*. nature nanotechnology, 2011. **6**(APRIL): p. 203-215.
18. J.R. Barnes, R.J.S., M.E. Welland, Ch. Gerber & J.K. Gimzewski, *Photothermal spectroscopy with femtojoule sensitivity using a micromechanical device*. Nature, 1994. **372**(3): p. 79-81.
19. Wu, G., et al., *Origin of nanomechanical cantilever motion generated from biomolecular interactions*. Proceedings of the National Academy of Sciences, 2001. **98**(4): p. 1560-1564.
20. Moy, V.T., E.L. Florin, and H.E. Gaub, *Intermolecular forces and energies between ligands and receptors*. Science, 1994. **266**(5183): p. 257-9.
21. Lee, J.H., et al., *Immunoassay of prostate-specific antigen (PSA) using resonant frequency shift of piezoelectric nanomechanical microcantilever*. Biosensors and Bioelectronics, 2005. **20**(10): p. 2157-2162.
22. Cha, M., et al., *Biomolecular detection with a thin membrane transducer*. Lab Chip, 2008. **8**(6): p. 932-7.
23. Concentris. *Concentris - Cantilever Sensor Products*. [cited 2013.10.30].
24. Veeco. *Veeco Develops First Commercial Cantilever Sensor System*. 2002 [cited 2013

31 Oct.].

25. J. Fritz, M.K.B., H. P. Lang, H. Rothuizen, P. Vettiger, E. Meyer, H.-J. Güntherodt, Ch. Gerber, J. K. Gimzewski, *Translating Biomolecular Recognition into Nanomechanics*. Science, 2000. **288**: p. 316-318.
26. J. Fritz, M.K.B., H. P. Lang, T. Strunz, E. Meyer, H.-J. Güntherodt, E. Delamarche, Ch. Gerber, and J. K. Gimzewski, *Stress at the Solid-Liquid Interface of Self-Assembled Monolayers on Gold Investigated with a Nanomechanical Sensor*. Langmuir, 2000. **16**: p. 9694-9696.
27. F. Frederix, K.B., W. Laureyn, G. Reekmans, A. Campitelli, W. Dehaen, and G. Maes, *Enhanced Performance of an Affinity Biosensor Interface Based on Mixed Self-Assembled Monolayers of Thiols on Gold*. Langmuir, 2003. **19**: p. 4351-4357.
28. Alvarez, M., et al., *Development of nanomechanical biosensors for detection of the pesticide DDT*. Biosens Bioelectron, 2003. **18**(5-6): p. 649-53.
29. Thundat, T., et al., *Detection of mercury vapor using resonating microcantilevers*. Applied Physics Letters, 1995. **66**(13): p. 1695-1697.
30. Ferrari, V., et al., *Development and application of mass sensors based on flexural resonances in alumina beams*. Ultrasonics, Ferroelectrics and Frequency Control, IEEE Transactions on, 1996. **43**(4): p. 601-608.
31. Pinnaduwaige, L.A., et al., *A sensitive, handheld vapor sensor based on microcantilevers*. Review of Scientific Instruments, 2004. **75**(11): p. 4554-4557.
32. Pinnaduwaige, L.A., et al., *Detection of 2,4-dinitrotoluene using microcantilever sensors*. Sensors and Actuators B: Chemical, 2004. **99**(2-3): p. 223-229.
33. Lang, H.P., et al., *An artificial nose based on a micromechanical cantilever array*. Analytica Chimica Acta, 1999. **393**(1-3): p. 59-65.
34. Battiston, F.M., et al., *A chemical sensor based on a microfabricated cantilever array with simultaneous resonance-frequency and bending readout*. Sensors and Actuators B: Chemical, 2001. **77**(1): p. 122-131.
35. Karin Y. Gfeller, N.N., Martin Hegner, *Micromechanical oscillators as rapid biosensor*

- for the detection of active growth of *Escherichia coli*. *Biosensors and Bioelectronics*, 2005. **21**: p. 528–533.
36. Kyungho Kang, A.S., Marit Nilsen-Hamilton, and Pranav Shrotriya, *Aptamer Functionalized Microcantilever Sensors for Cocaine Detection*. *Langmuir*, 2011. **27**: p. 14696–14702.
37. Calleja, M., et al., *Challenges for nanomechanical sensors in biological detection*. *Nanoscale*, 2012. **4**(16): p. 4925-38.
38. Chatzandroulis, S., et al., *Capacitive-type chemical sensors using thin silicon/polymer bimorph membranes*. *Sensors and Actuators B: Chemical*, 2004. **103**(1–2): p. 392-396.
39. Satyanarayana, S., D.T. McCormick, and A. Majumdar, *Parylene micro membrane capacitive sensor array for chemical and biological sensing*. *Sensors and Actuators B: Chemical*, 2006. **115**(1): p. 494-502.
40. Rüdiger Berger, E.D., Hans Peter Lang, Christoph Gerber, James K. Gimzewski, Ernst Meyer, Hans-Joachim Güntherodt, *Surface Stress in the Self-Assembly of Alkanethiols on Gold*. *Science*, 1997. **276**(27): p. 2021-2024.
41. Wu, G., et al., *Bioassay of prostate-specific antigen (PSA) using microcantilevers*. *Nat Biotechnol*, 2001. **19**(9): p. 856-60.
42. Pei, J., F. Tian, and T. Thundat, *Glucose biosensor based on the microcantilever*. *Anal Chem*, 2004. **76**(2): p. 292-7.
43. Rugar, D., H.J. Mamin, and P. Guethner, *Improved fiber-optic interferometer for atomic force microscopy*. *Applied Physics Letters*, 1989. **55**(25): p. 2588-2590.
44. Yaralioglu, G.G., et al., *Analysis and design of an interdigital cantilever as a displacement sensor*. *Journal of Applied Physics*, 1998. **83**(12): p. 7405-7415.
45. Sang, S., *An approach to the design of surface stress-based PDMS micro-membrane biosensors-Concept, Numerical simulations and Prototypes*, in *University of Bibliothek*. 2010, University of Bibliothek: Ilmenau.
46. Engvall, E. and P. Perlmann, *Enzyme-linked immunosorbent assay (ELISA). Quantitative assay of immunoglobulin G*. *Immunochemistry*, 1971. **8**(9): p. 871-4.

47. Southern, E.M., *Detection of specific sequences among DNA fragments separated by gel electrophoresis*. Journal of Molecular Biology, 1975. **98**(3): p. 503-517.
48. Burnette, W.N., "Western blotting": *electrophoretic transfer of proteins from sodium dodecyl sulfate--polyacrylamide gels to unmodified nitrocellulose and radiographic detection with antibody and radioiodinated protein A*. Anal Biochem, 1981. **112**(2): p. 195-203.
49. Dugas, V., A. Elaissari, and Y. Chevalier, *Surface Sensitization Techniques and Recognition Receptors Immobilization on Biosensors and Microarrays*, in *Recognition Receptors in Biosensors*, M. Zourob, Editor. 2010, Springer New York. p. 47-134.
50. www.aptagen.com/home.aspx. *Aptamer*. 2013 [cited 2013 19th Oct.].
51. Jayasena, S.D., *Aptamers: An Emerging Class of Molecules That Rival Antibodies in Diagnostics*. Clinical Chemistry, 1999. **45**(9): p. 1628-1650.
52. www.chem.ufl.edu. *cell SELEX*. [cited 2013 20th Oct.].
53. Nimjee, S.M., C.P. Rusconi, and B.A. Sullenger, *Aptamers: an emerging class of therapeutics*. Annual Review Of Medicine, 2005. **56**: p. 555-583.
54. Kang, K., *MicroCantilever (MC) based nanomechanical sensor for detection of molecular interactions*, in *Mechanical Engineering*. 2011, Iowa State University.
55. WIKIPEDIA. *Dissociation constant*.

Chapter 3. System Design and Manufacturing

3.1 Thin Membrane Transducer

3.1.1 MEMS Fabrication

3.1.1.1 Sensor Design and Simulation

3.1.1.2 Double Layer of Photoresist

3.1.2 Sensitivity Enhancement

3.1.2.1 Fluorocarbon SAM Coating

3.1.2.2 Self-aligned Proximate Shadow Mask

3.1.3 MEMS Sensor Packaging

3.2 Receptor Molecular Structure

3.2.1 Self-Assembly Monolayer

3.2.2 Effect of Gold Surface

3.2.3 Molecular Immobilization

3.3 Capacitive Measurement System

3.3.1 Analogue to Digital Convertor

3.3.2 Capacitive Measurement Circuit

3.4 Reference

Chapter 3

System Design and Manufacturing

In the recent years, chemomechanical transducer has been investigated for label free, highly sensitive and selective detection. The chemomechanical transducers utilize a balance between chemical free energy and mechanical strain to induce a surface stress on the transducer. On one surface of the sensor, specific reactions with grafted receptor molecule change the surface stress caused by changes in intermolecular forces. These include complex forces such hydration, electrostatic, osmotic, entropic, van der Waals and steric effects. Therefore, the interplay of chemistry and mechanics controls the mechanical deformation.

In the nanometer scale, mechanical deflection are dominated with surface stress rather than normal stress[1]. The magnitude of strain (ϵ) of normal stress (σ) is constant, but the strain (ϵ_s) of surface stress (σ_s) is approximated shown in figure 3-1:

$$F = \sigma \cdot A + \sigma_s \cdot 2(t + w) \quad \text{Equation 3-1}$$

$$\epsilon_s = \frac{\sigma_s \cdot 2(t+w)}{EA} \sim \frac{2(t+w)}{wt} \sim \frac{1}{t} \quad \text{Equation 3-2}$$

Also, this equation assume the deflection under the thickness of plate; small deflection range. The thickness of the plate is inverse proportional to the surface strain which implies that even if the thickness of the film decrease, the proportion of surface strain in total strain increases.

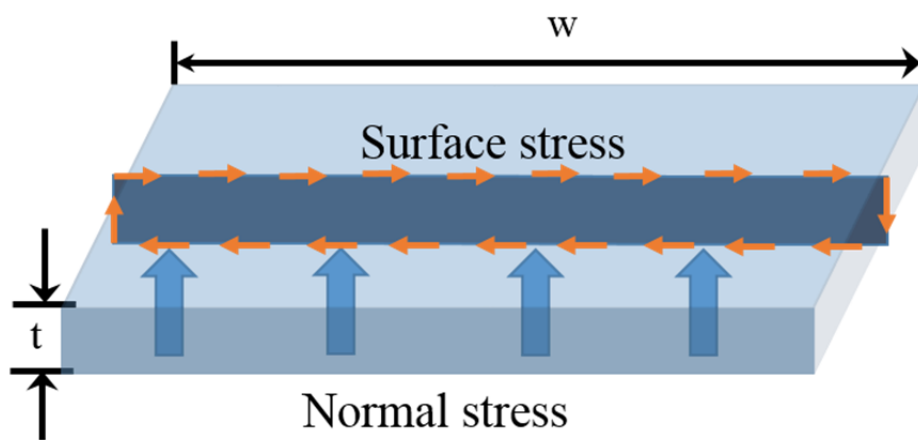


Figure 3-1. Schematics of normal stress and surface stress.

3.1 Thin Membrane Transducer

As I described at chapter 2.2.2 Membrane transducer, membrane transducer has a lot of benefits such as label, electronic readout, real-time monitoring and suitable platform for both liquid and gas. In the previous research, most of membrane-based chemomechanical transducer use a polymer material to increase the sensitivity of the membrane transducer. Although the polymer membrane transducer has low elastic modulus, it has some problems such as reliability associated with the use of polymer in wet environments and uniformity compared with micromachined materials. Also, polymer membrane is difficult to fabricate integrated device and package with reaction chamber or fluidic channel due to extremely flexible and low melting temperature. Therefore, I develop fully integrated thin membrane transducer using micromachined technology with silicon nitride membrane material.

The following equation by Stoney dictates that the amount of deflection of the membrane is proportional to σ surface stress and inversely proportional to Young's modulus and the second power of the thickness

$$\frac{1}{R} = 6 \left(\frac{1-\nu}{Et^2} \right) \sigma \quad \text{Equation 3.1-1}$$

where R is the radius of curvature and ν Poisson ratio. Also, the effect of molecular reaction occurs surface stress that move the neutral axis of a rigid body described in figure 3-2. The movement of neutral axis induces the deformation of

membrane to release the surface stress with balancing between molecular free energy and mechanical restoring force.

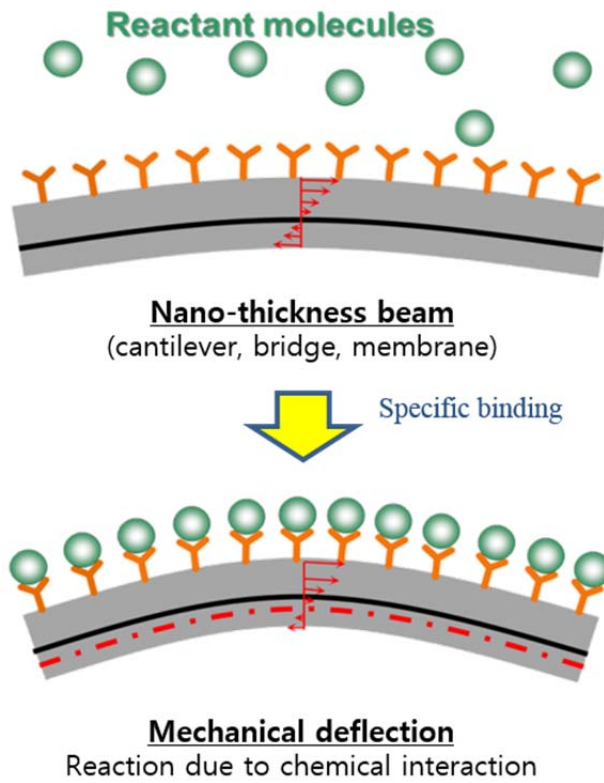


Figure 3-2. Membrane deformation due to molecular reaction

3.1.1 MEMS Fabrication

Thin membrane transducer can be realized with MEMS technology to integrated micro scale components such as membrane, spacer, parallel electrode and reaction layers into a complete platform. KOH wet silicon etch, electroplating, dimple process, electrode bridge process and sacrificial layer and release process are the keys for compact design, low cost and low temperature fabrication process which is compatible with CMOS integration.

3.1.1.1 Sensor Design and Simulation

Thin membrane transducer is depicted in figure 3-3. The membrane transducers are composed of seven layers, which involve surface and bulk micromachining. The core components of transducer consist of membrane, reaction gold, lower electrode, spacer, upper electrode and pad layer. The reaction gold layer is deposited by using self-aligned shadow mask to produce a particular geometry, where molecules are immobilized on the specific region. Silicon substrate is etched to make a reaction chamber and float membrane, while silicon nitride is deposited with low-pressure chemical vapour deposition (LPCVD), which is a batch process effectively reduces wafer to wafer variation. Those processes significantly improve thin membrane transducer due to high chip to chip uniformity and conformal deposition, as well as low residual stress. Metallization of the membrane, lower electrode, is fabricated with metal deposition and photolithography. Also, dielectric double layers are conformed to deposit on silicon oxide layer to reduce parasitic capacitance.

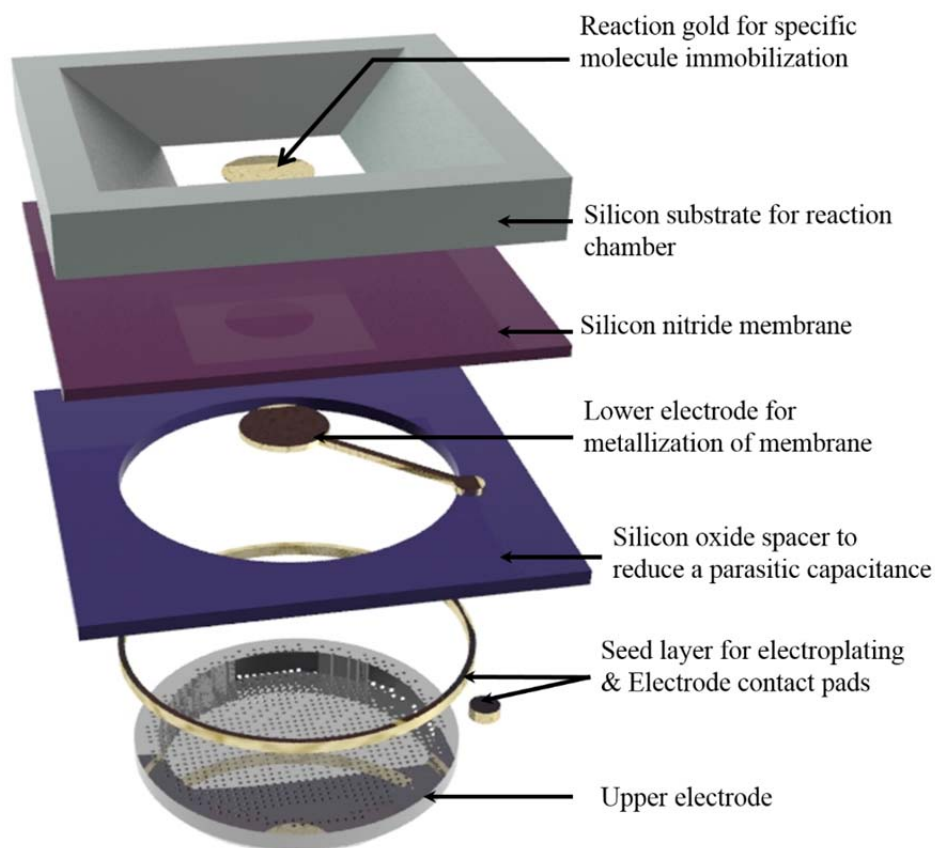


Figure 3-3. Concept of the micromachined membrane capacitive sensor. All part of the sensor is integrated with MEMS fabrication to manufacture uniform performance.

Then, sacrificial layer construct constant gap between lower electrode and upper rigid electrode and the dimple patterns are patterned on the sacrificial layer. The dimple structures increase the stability on the wet environment during the fabrication as well as working situation. Next, rigid upper nickel electrode structure is constructed with electroplating by controlling stress in which stress is carefully controlled the electrode to reduce the deformation of itself. Finally, electrode

contact pads use the seed layer of upper electrode electroplating to reduce the cost of fabrication. For the high quality and reliability of the sensor, those of processes must be developed with exquisite recipes for fabrication flow.

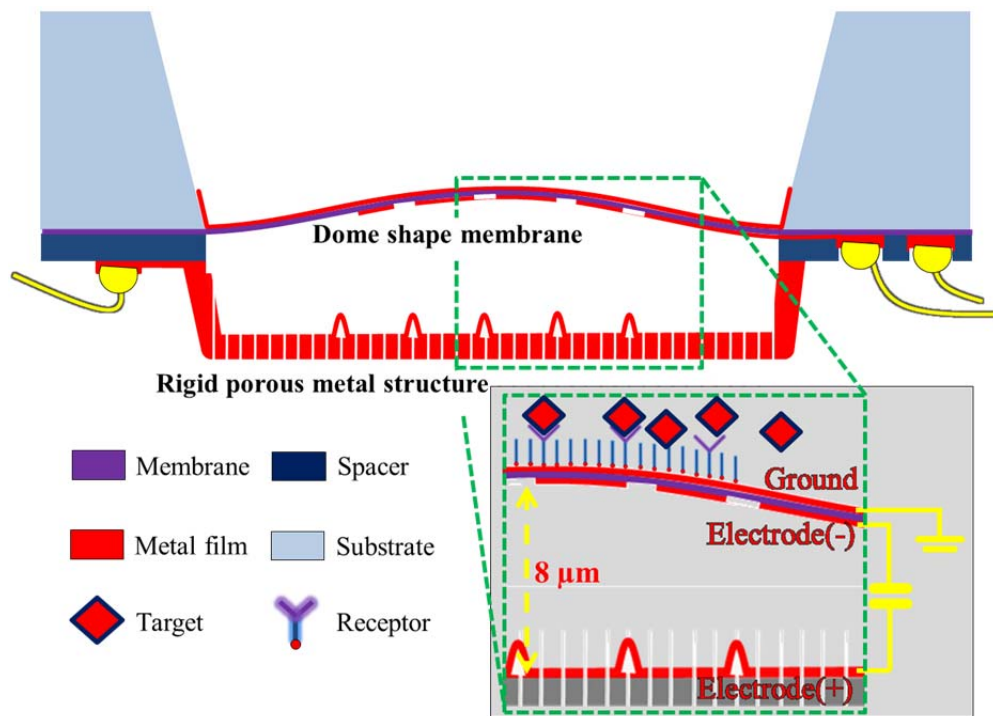


Figure 3-4. The cross-sectional view of membrane capacitive sensor which utilize a silicon nitride membrane fixed on all four sides and is suspended with composited metal layers.

Figure 3-4 show the working principle of membrane transducer and a capacitance measurement. Binding of analyte molecules to the probes immobilized on top of the membrane surface changes the surface stress. The compressive surface stress causes the mechanical deflection of membrane that increases the air-gap and reduces the capacitance value. The silicon substrate, which is bulk micromachined with potassium hydroxide etch of silicon nitride mask, can be used for individual

reaction chamber for array sensors. Also, the electroplated nickel electrode structure has 40% ratio of ventilation holes for the purpose of releasing the sacrificial layer and prohibiting squeeze-film air damping[2]. The damping effect of air flow in holes is considered as a vertical flow by conventional Reynolds' equation for infinite thick hole-plate. Therefore, the thin membrane transducer use the confined membrane structure that is readily multiplexed with different spotting functionalization[3].

The design, geometry and performance of these capacitive membrane sensors, however, can be limited by the high stiffness of the silicon-based materials. Accordingly, it is desirable in a sensor design to increase the sensitive surface stress and minimize undesired thermal and chemical noises. Arun majumdar suggested that the same metal material and same dimension with reaction metal is coated at the bottom of membrane to compensate for those undesired sensor responses in a membrane capacitive sensor[4]. Figure 3-5 depict the cross-sectional view of metal compensation membrane structure. A material has particular thermal expansion coefficient can induce noise on the composite membrane. The thermal noise will be canceled if the same material and dimension metal is coated on the counter side of membrane. However when the membrane is immersed in liquid, fluidic and hydraulic pressure exert load onto it which causes the membrane to deflect with ambiguous curvature. After the deflection due to perpendicular pressure, the both metal layers composited on curving membrane suffer with opposite stresses such as compressive and tensile stresses that produce severe noise. Therefore, it is important to analyze the sensitively proportional area of reaction

gold to react surface stress and the optimizing area of lower electrode to measure the capacitance.

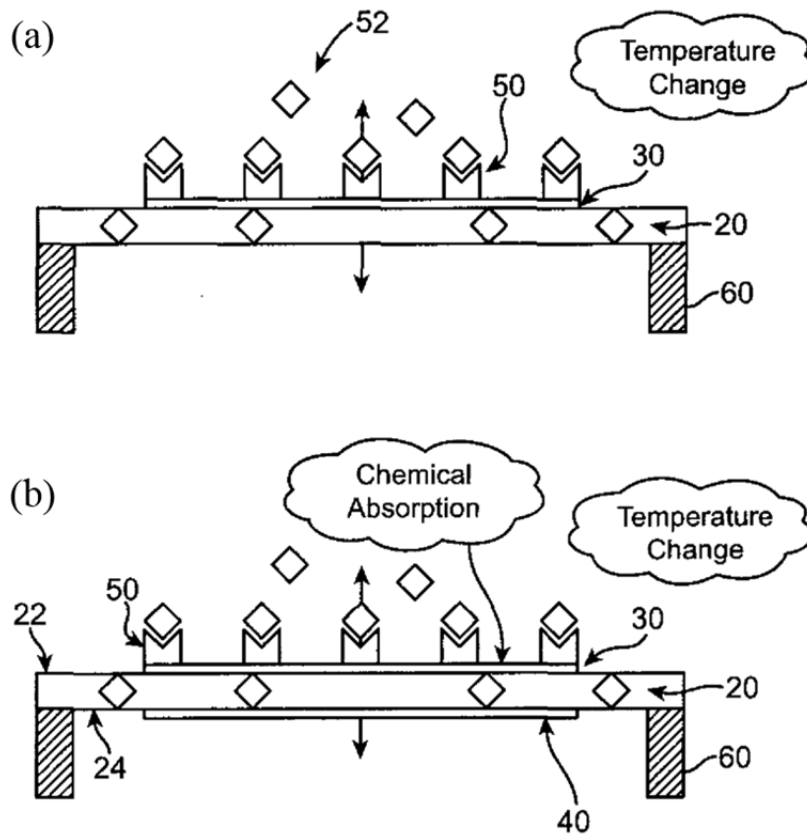


Figure 3-5. A cross-sectional view of membrane sensor (a) without compensator, this membrane can be easily affected by undesired noise signal, (b) with compensator, common noises such as temperature and electron charge can be removed at both metal layers.

The design variables that are available for optimization are the reaction gold size on the silicon nitride membrane. When the gold covers the whole area of membrane, it was expected that the membrane deflection would be zero since the

membrane configuration is similar to the double-clamped beam configuration. Unlike the case of the double-clamped configuration, analytical solutions for membrane deflection arising from surface stress changes for partially covered membranes do not exist. Consequently, finite element (FE) analysis is used to determine the optimal gold coverage ratio for the membrane sensor. The details of the FE model are listed in Table 5. The FE analysis software is no direct method to apply a surface stress load. Hence, a method for applying surface stress load via a bulk stress on the gold is used. The assumption is valid owing to the sufficiently large flexible rigidity of the silicon nitride which Young's modulus and thickness are four and ten times larger than gold's, respectively. Different geometries of reaction gold like circular, rhombic and square shapes are modelled on the membrane, to investigate the effect of the radius from the center point on the membrane deflection. Flat plate is considered as the initial condition which has its four surfaces being clamped. The residual stress on the reaction gold is expressed with a 5 N/m compressive surface stress, which is equivalent to 100 MPa. Such residual stress will be transferred to the silicon nitride membrane that gives rise to deflection on the membrane where the reaction gold is deposited onto, as depicted in figure 3-6. From graph, it is clear that the increasing size of reaction gold induces larger residual stress that brings more membrane deflection.

Table 5. Simulation parameter of square silicon nitride membrane induced by attaching the residual gold surface representing the surface stress of molecular interaction.

	Silicon nitride	Gold
Elasticity Modulus(Gpa)	310	80
Poisson ratio	0.27	0.4
Element type (mechanical)	Solid 186	Shell93
Element size (mesh size)	1.5 μm	1.5 μm
Size	400 μm	r = 10~200 μm
Thickness	100 nm	50 nm
Boundary condition	4-faced fixed	Attached with silicon nitride
Initial condition	$\sigma_{xx} = \sigma_{yy} = \sigma_{zz} = 0$	$\sigma_{xx} = \sigma_{yy} = 100\text{MPa}, \sigma_{zz} = 0$

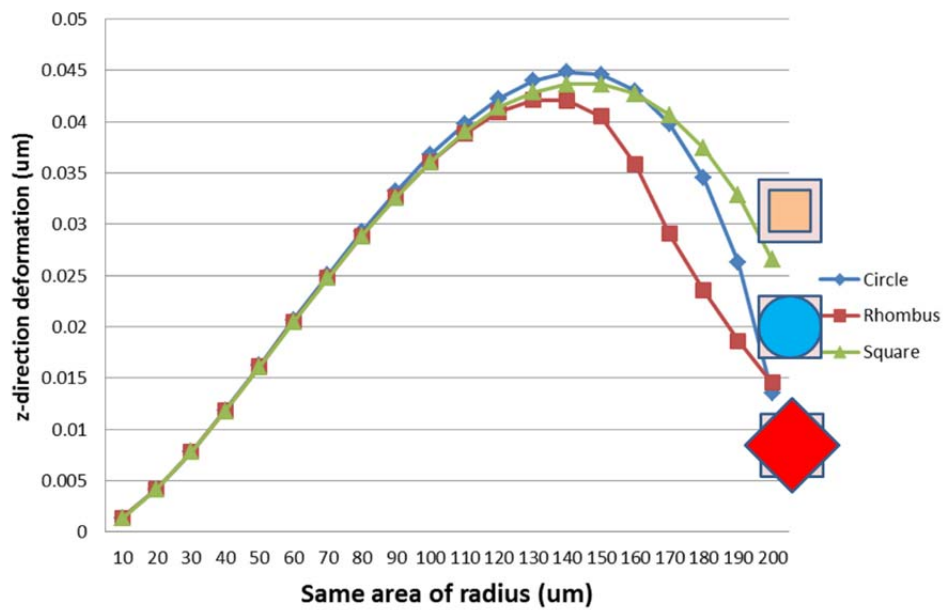
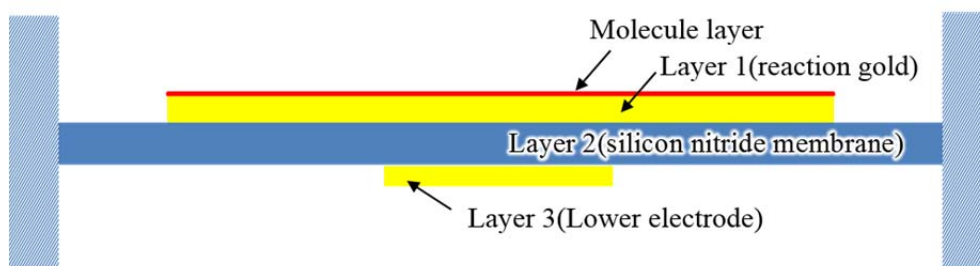


Figure 3-6. Electrode shape and size simulation according to same area on the silicon nitride membrane of 400 μm length square

Additionally, most surface stress is concentrated in the edge of reaction gold layer. When the edge of reaction gold is closed in the rigid substrate, the deflection of membrane is decreased. Therefore, approximately 70% length of reaction gold is chosen as the optimal size to be deposited on the whole silicon nitride membrane. Furthermore in the FE analysis, a complex structure is simplified to a two dimensional beam model which surface stress induced deflection can be determined easily. A simulation showing the deflection of the cantilever is possible by using Stoney's equation.[5]



	Material	Young's modulus [Gpa]	Density [kg/m ³]	Possion	Thickness (μm)	Length (μm)	Stress
Molecule layer	Alkanethiol	0.5	13.8	0.27	0.025	750	-100mN/m
layer 1	Gold	80	3100	0.4	0.05	750	-100MPa
layer 2	SiN	310	19,300	0.27	0.5	750	20
layer 3	Gold	80	3100	0.4	0.05	750	-100MPa

Figure 3-7. Beam model and material parameter for FEM simulation. Alkanethiol parameter [6].

In addition, the simulation results is confirmed with several models such as attaching no residual stress beam and rejecting the surface stress when the same reaction gold is added on the opposite side of membrane. The simulation result is

included in the appendix section. The schematic model and material parameters used in the simulation as depicted in the figure 3-7. The dimensional discrepancy of the lower electrode and the reaction gold creates a residual stress mismatch that leads to a buckling phenomenon in the initial state shown in figure 3-8. In such condition, the behavior of the deflection can be observed with respect to the design parameters when 100 mN/m surface stress is applied. Membrane structure has smaller deflection magnitude compared to cantilever, but the linearity of its deflection is suitable for electrical measurement that eventually gives birth to a sufficiently sensitive sensor described in figure 3-9.

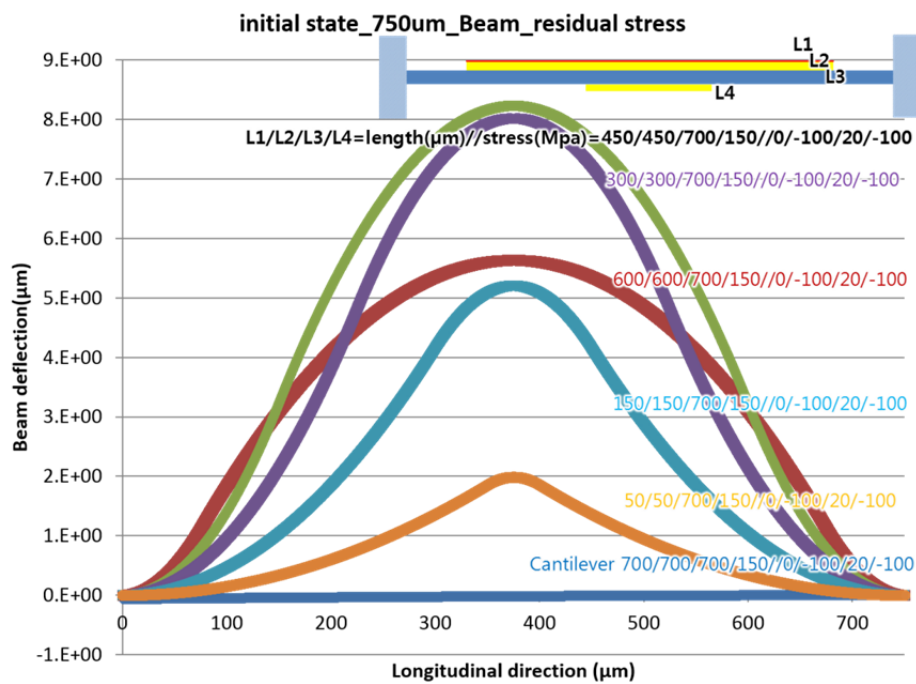


Figure 3-8. Initial buckling of beam due to residual stress mismatch.

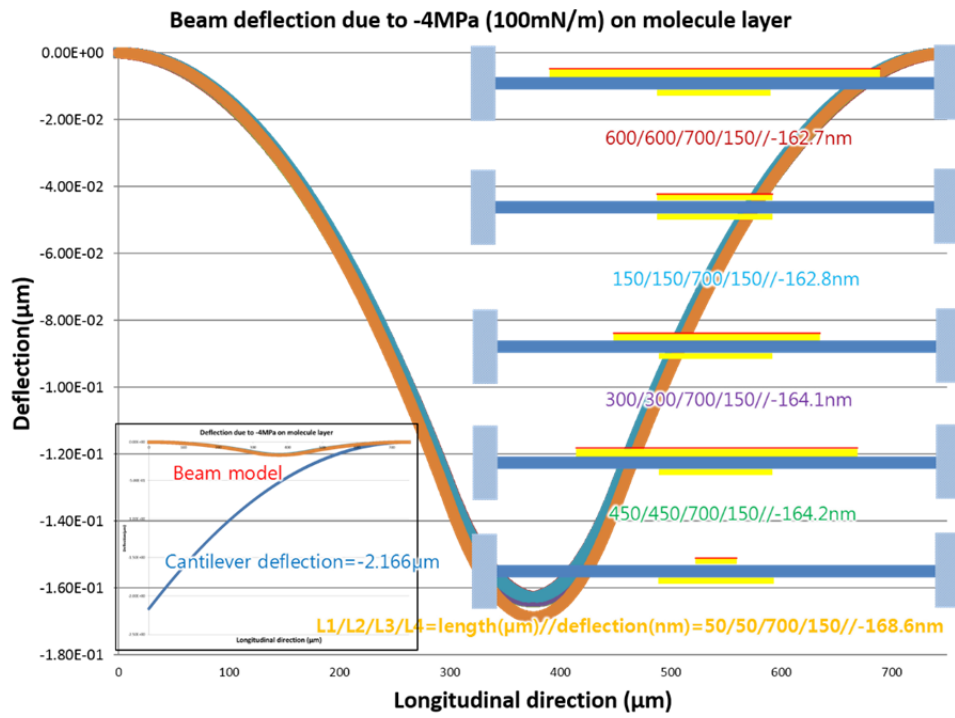


Figure 3-9. Surface stress induced membrane deflection. The deflection due to tensile stress is smaller compared to cantilever model is apparent in the simulation result.

3.1.1.2 Double Layer of Photoresist

This membrane transducer is compatible with CMOS circuit because all micromachining procedures involved are low temperature processes. It can be fabricated on a wafer containing CMOS analog-digital converter chip, to form a one-chip configuration. Despite stiction problem between layers during releasing process [7], photoresistes are often used for open structure of research products such as cantilever[8], scratch drive[9] and MEMS swtiches[10] owing to high uniformity with spin coating, easy thickness control and cost-effectiveness. Nevertheless, the deposition of a thick metal layer with low stress on the photoresist-double layer, without any compromises of mentioned advantages is a very demanding process.

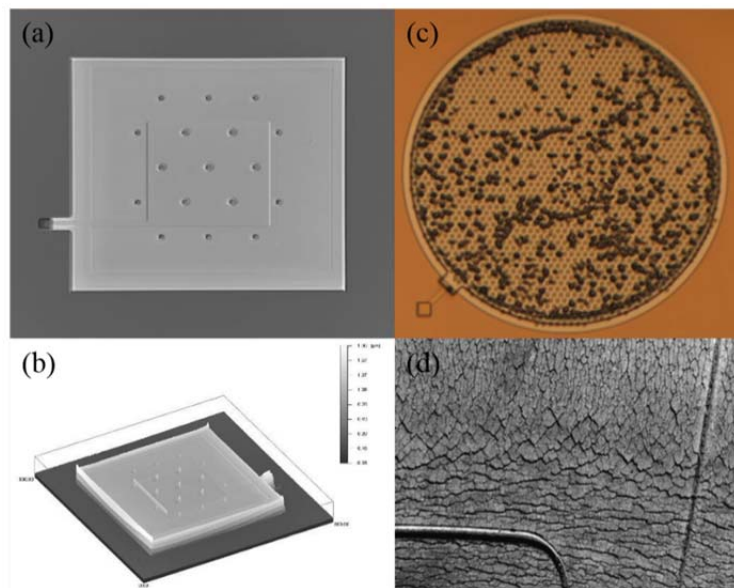


Figure 3-10. Sacrificial layer: (a) a patterned sacrificial layer with dimple structures, (b) 3D profile image of sacrificial layer, (c) plasma damage of sacrificial layer and (d) crack pattern on the sacrificial layer due to thermal damage.

Firstly, one should use negative photoresist, AZ5214-E because it is more resistive to the effects brought by heat and plasma treatments. A 2 μm thick photoresist layer is spin coated at 2500 rpm and undergoes a soft baking process prior to UV exposure with 70 mJ to create a sacrificial pattern. Then, the sacrificial layer is given a secondary UV exposure beneath a dimple mask in order to create dimple structures on the surface, as shown in figure 3-10(a) and 10(b). The UV exposure duration is controlled for one step lithography so that no post-exposure-bake (PEB) is needed. The dimple structure aims to prevent stiction problem after removing the sacrificial layer. Next, it is followed by photoresist development process and hard bake process at 120°C for 30 minutes to remove the residue of polymer solvent. During the hard bake process, the reflow of polymer layer that leads to a highly uniform layer occurs. After that, seed layers comprised of 300Å Cr and 1500Å Au are deposited on the sacrificial layer by using a gold sputter at 400W DC power, 2mTorr pressure for 90 seconds before the electroplating process in order to obtain a low stress metal layer. Figure 10(c) shows the undesirable condition of the polymer if the solvent is not completely removed. In case of other type of photoresist is used, thermal damage such as cracks would form on the the surface of sacrificial layer, as shown in figure 10(d). The crack defect is highly undesirable because it causes trouble to the formation of upper electrode and creates short circuit with the lower electrode.

is calculated to reduce the air damping effect of squeeze-film for thick hole-plate which is refer to the literature [11] shown as figure 3-12, the perforated planar structure for thick metal layer is similar with a nickel electroplating structure 3-12(a). The hole of hexagonal lattice increase the rigidity of a perforated planar structure 3-12(b) and the density of holes in the plate is optimized to the ratio of lateral and vertical air viscous damping 3-12(c).

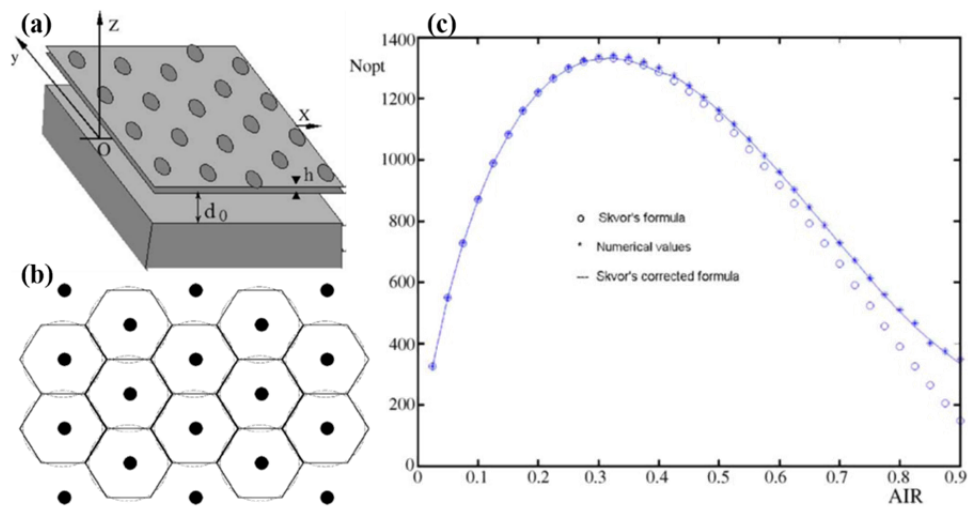


Figure 3-12. Reducing viscous damping of perforated planar micromechanical structures.

Next, the nickel metal is electroplated on the patterned structure at $55^{\circ}C$ 100mA for 2300 seconds 3-11(d). Subsequently, the electroplating mold layer is removed through development process after the exposure of 105 mJ UV light. This is preferable than ethanol and dry ashing method because they cause damage to the sacrificial layer underneath the metal layer, which UV light cannot penetrate through 3-11(e). Also, before the wet etching of metal layer to release the sacrificial layer, the thick AZ4330 photoresist layer is patterned with $6 \mu m$

thickness to prevent the detachment of nickel electrode due to the undercut of wet etching and creat electrode contact pads 3-11(f). Then, the seed layers comprising of gold and chromium metal are wet etched with the echants of AU-5 and Cr-7, resepectively 3-11(g). Lastly, the sonication in ethanol is conducted to remove the seed layer photoresist and the hard-baked sacrificial photoresist is eliminated with dry ashing. Dry ashing through the air holes prevents the deflection of nickel structure and the stiction between membrane and nickel structure 3-11(h). This process produces capacitive electrode with uniform gap and thick metal layer with low stress.

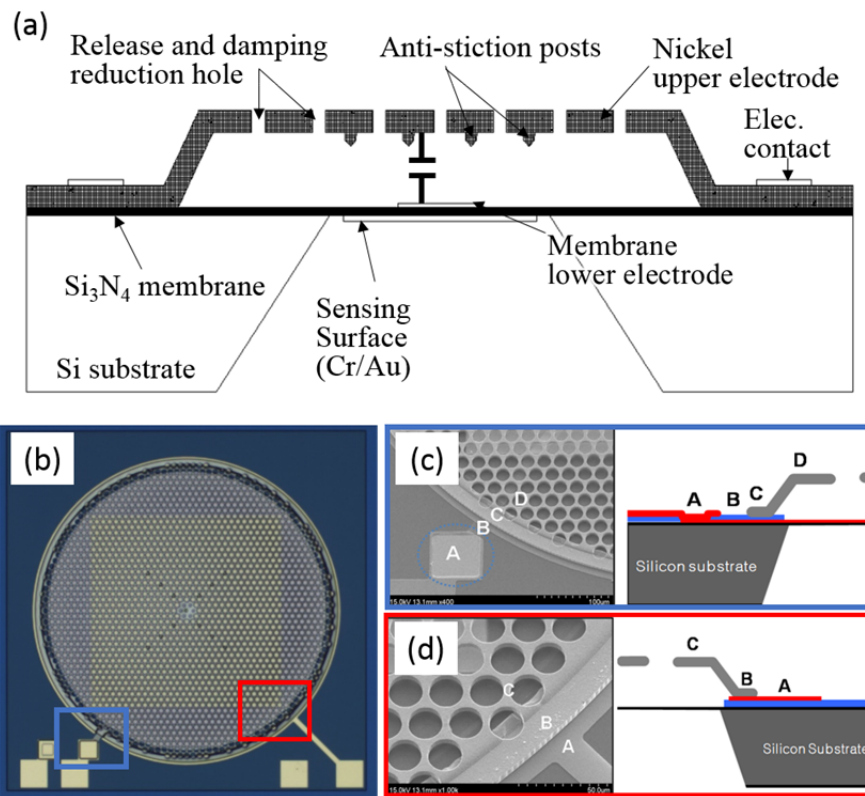


Figure 3-13. The schematics of membrane transducer: (a) cross-sectional view, (b) capacitance electrode view (c) lower electrode pad connected with membrane

electrode through electrode-bridge and (d) upper electrode with lots of holes for preventing air-film squeeze damping

Figure 3-13(a) shows the cross-sectional view of fabricated membrane transducer. The nickel upper electrode of low stress electroplating has anti-stiction posts and lots of air hole for removing sacrificial layer and reducing air film damping effects. The top view of membrane transducer in figure 3-13(b) has simple shape of electrodes with the techniques of double sacrificial layer and electrode bridge. The lower electrode is connected with electrode contact pad through the electrode bridge 3-13(c) and the upper electrode is connected with electrode contact pad through seed metal layer 3-13(d).

The special process of double photoresist sacrificial layer form the uniform feature of massive array membrane transducers and these has identical characteristics shown as figure 3-14.

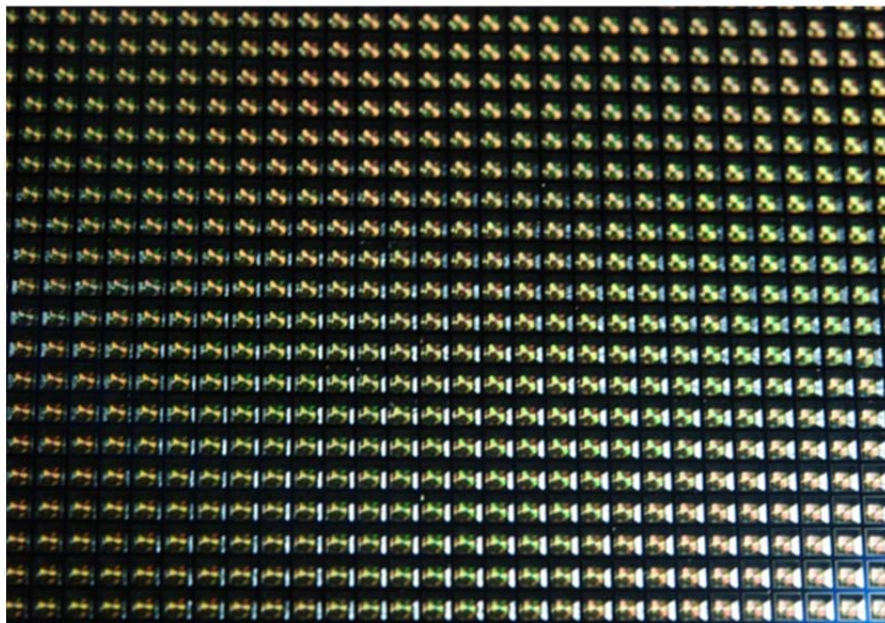
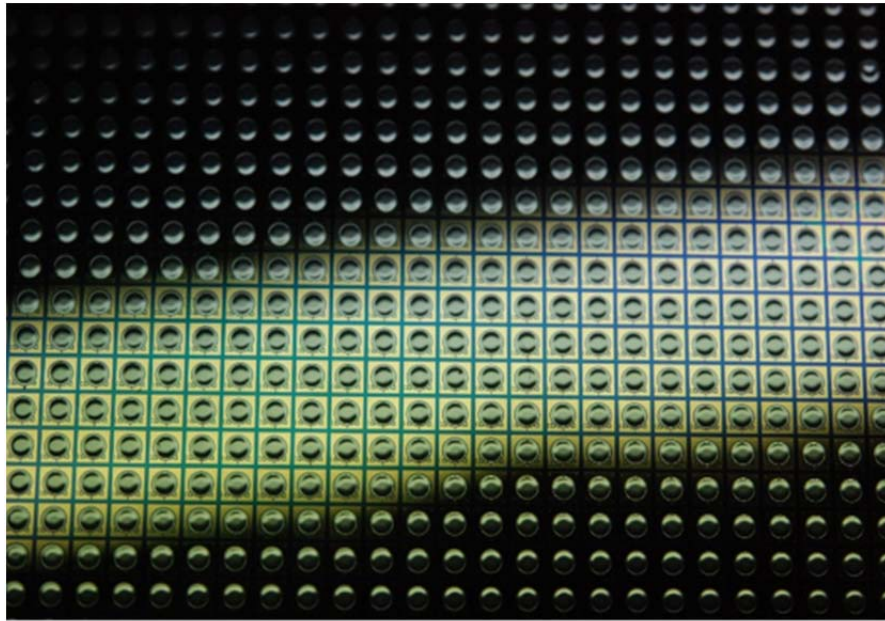


Figure 3-14. Optical image of completely fabricating membrane transducers

3.1.2 Sensitivity Enhancement

3.1.2.1 Fluorocarbon SAM Coating

One cannot overlook the reliability of the sensor in different conditions and environments. In order to enhance the stability of the sensor, the coating of hydrophobic fluorocarbon monolayer on the capacitance measurement part via vapor deposition is necessary[12]. The vapor deposition uses the plasma of C_4F_8 at 100 sccm, leaving a thin film on the silicon oxide layer, shown in figure 3-15(a). Despite extreme thickness, the coated layer shows excellent hydrophobic property, which is apparent in figure 3-15(b). This fluorocarbon material on the electrode pad does not pose any problems in the wire bonding packaging, is another advantage of the material. Moreover, the fluorocarbon film prevents stiction between floating silicon nitride membrane and rigid structure of upper electrode after silicon wet etch. Furthermore, the refrigeration of the sensor is required in the immobilization process of probe molecules, which is made possible by the fluorocarbon film. The fluorocarbon film is the main reason for the sensor to work properly even in high humidity environment. Moreover, the noise problem of the electrode metal caused by non-specific adsorption in gas detection can be tackled with the fluorocarbon coating.

The thickness and hydrophobic property relation of the polymer with deposition time is expressed in figure 3-16. The Deep RIE (PLASMA-THERM) equipment is operated at such conditions: 825 W, 30 sccm Argon and 100 sccm C_4F_8 .

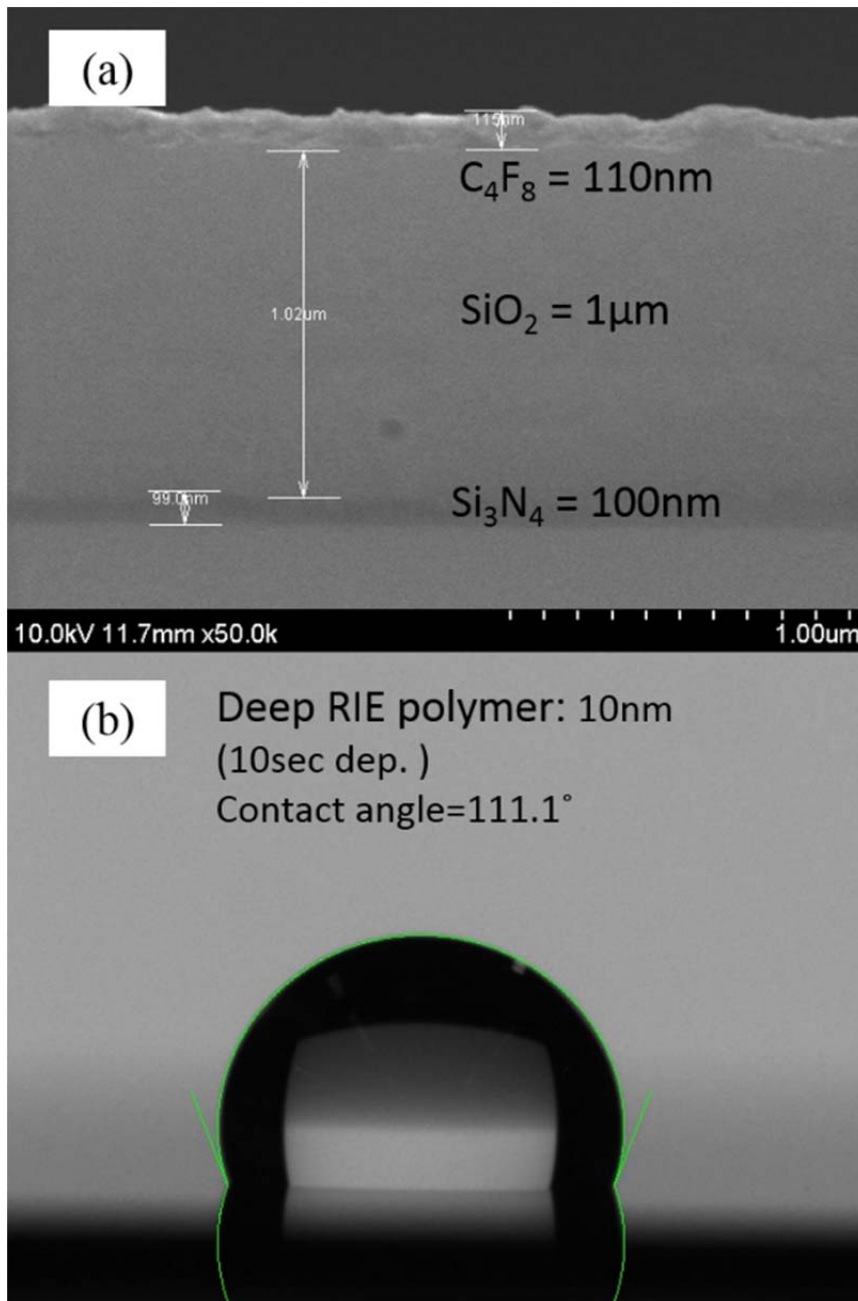


Figure 3-15. Fluorocarbon film and hydrophobic property.

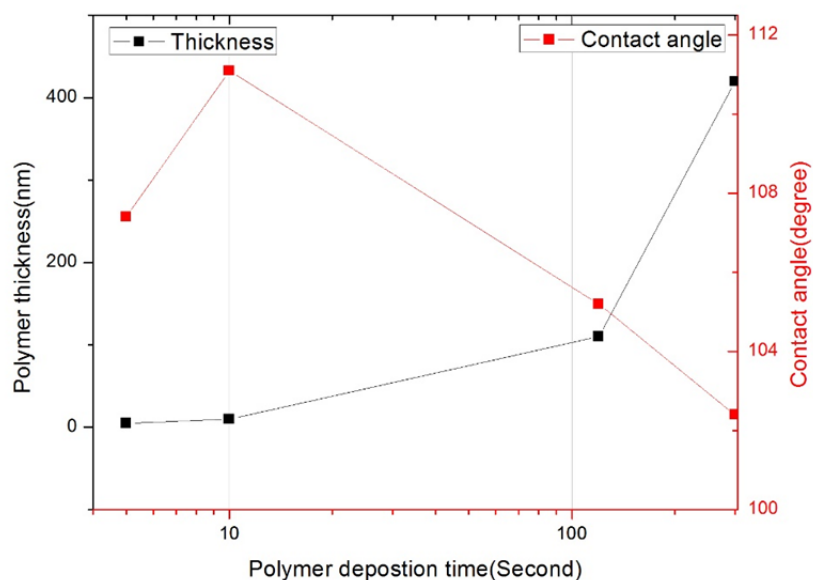


Figure 3-16. Polymer thickness and hydrophobicity according to polymer deposition time.

3.1.2.2 Self-aligned Proximate Shadow Mask

The membrane deflection will reduce significantly if the whole membrane is covered by the reaction gold because of the surface stress transfer to the rigid bulk silicon structure. The influence of gold coverage ratio upon sensing response associated with membrane deflection is simulated. It is discovered that not only the coverage ratio matters, but the geometry of the reaction gold immensely affects the sensing performance. In order to deposit the reaction gold at a desirable position, a holder is used to place a shadow mask on the membrane transducer wafer. Figure 3-17 shows the picture of the holder with an O-ring which is used to prevent the wafer from sliding. Since the membrane is located 500 μm deep from the wafer

surface, it is inevitable that air being trapped between the membrane transducer wafer and shadow mask wafer in ambient environment. However those gas will escape from the wafer interface in vacuum condition, leaving a narrow gap. The gap is responsible for the misalignment problem due to the sliding of the wafers in vacuum pressure during the metal deposition process. Therefore, instead, a close proximity self-aligned shadow mask is used to deposit gold layer. Ravi Kummamuru et al[13] reported the use of a similar close proximity self-aligned shadow mask in sputter deposition onto a membrane under a cavity.

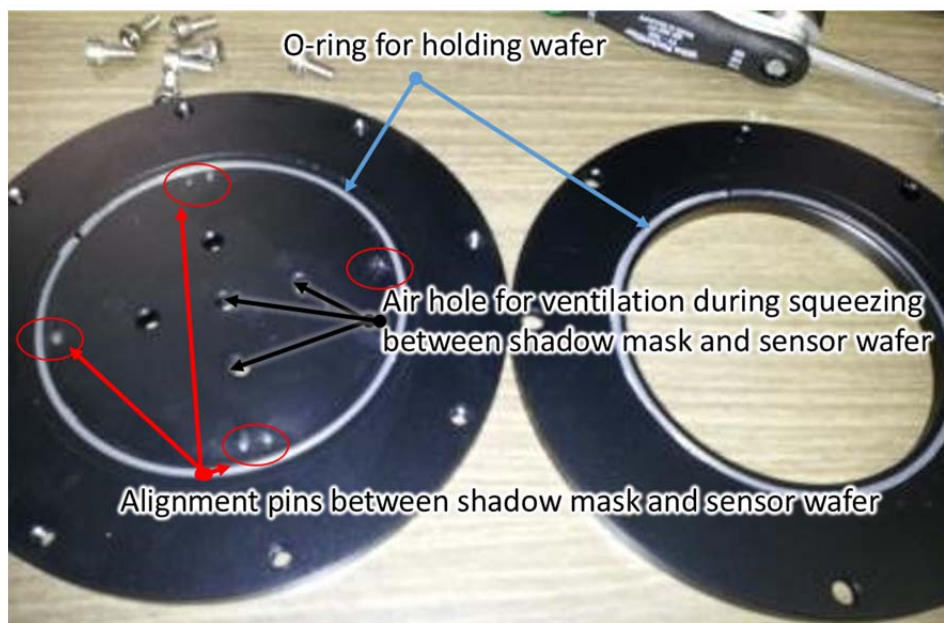


Figure 3-17. Shadow mask holder. This oxidized metal utilizes O-rings for seizing the wafer.

Figure 3-18 presents the structure of a shadow mask that possesses pillars that facilitate well alignment onto the cavity of reaction chamber existing between sensor and shadow mask. To fabricate a close proximity self-aligned shadow mask, silicon oxide and silicon nitride are deposited on a bare silicon wafer orderly. Then,

the silicon oxide and silicon nitrides at the backside are etched away through backside patterning, followed by wafer through etching with TMAH 30% solution. An inclined plane is made at $\langle 111 \rangle$ direction on the front side of the wafer. After that, a desirable pattern is made on the floating membrane of the shadow mask. Conveniently, one can use such close proximity self-aligned shadow mask to transfer reaction gold with desirable pattern onto the reaction surface of the thin membrane transducer.

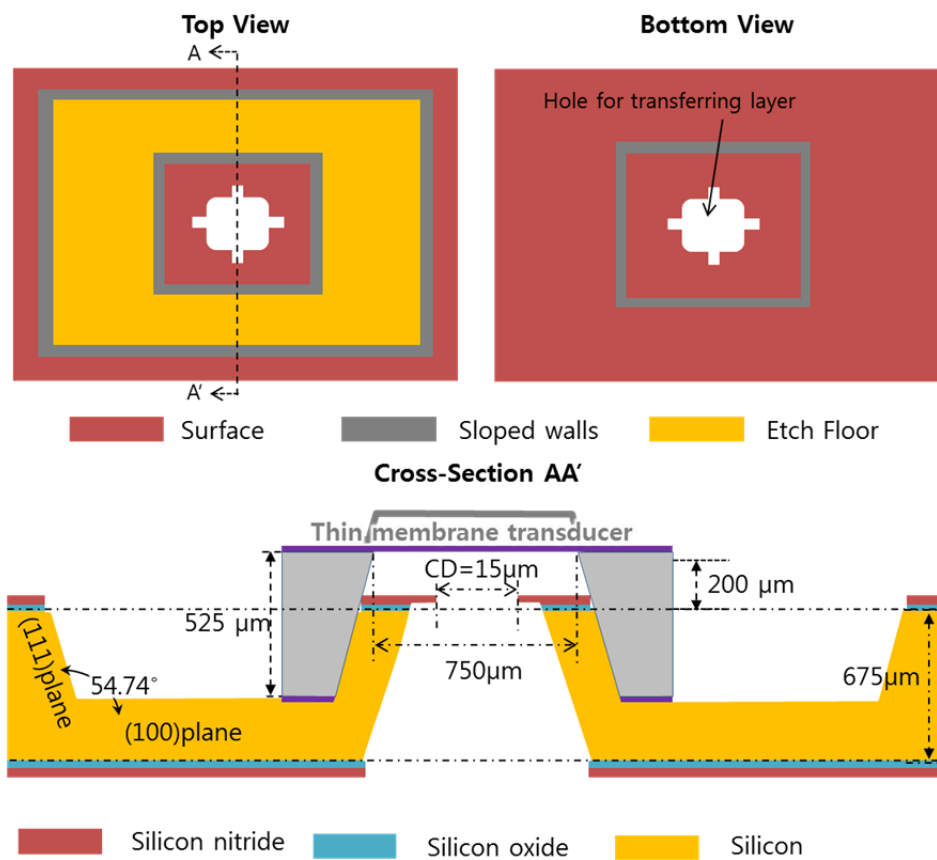


Figure 3-18. Schematics of shadow mask. A high accuracy of alignment in the close proximity shadow mask between sensor and shadow mask is achieved. The slope pillar for alignment is made of potassium hydroxide (KOH) etch.

Despite difficult fabrication process, however, the shadow mask fabricated in this manner is structurally weak. Thus, a modified self-aligned shadow mask with SU-8 pillar is developed to reduce bulk micro machining in the fabrication process. The fabrication process is relatively easy and the shadow mask handling is more convenient. In fact, the fabrication of high aspect ratio SU-8 pillar, of 160 μm thickness and 10 μm critical width, is the essential technology of the modified shadow mask. After several trials, it is found that SU-8 3050, usually used for thin film application, coated twice with 80 μm thickness has better result than one-time thick film coating with SU-8. Furthermore, SU-8 pattern ought to be added onto the shadow mask after the membrane is constructed. Otherwise, SU-8 film will be torn off by the residue stress introduced in the silicon wet etching process. Also, SU-8 is likely to peel off from the surface when the stress of the film is reasonably large. Therefore, one should ensure the wafer surface is clean and hydrophilic prior to coating to prevent such problem. O₂ plasma treatment for 20 seconds is another must-do procedure. The details of the fabrication procedures are summarized in the following table 6.

Table 6. 2 step SU-8 process flow for high aspect ratio

	Process	Condition
1	Surface cleaning	O ₂ plasma treatment (Tepla 300, Ar/O ₂ =700 ml/min, 700 watts, 20 sec.)
2	SU-8 coating	Spin coating (500 rpm 5sec. → 1700 rpm 30 sec.)
3	Soft bake	Hot plate 95 °C, 20 min.
4	Cooling	Room temperature 5 min.
5	SU-8 coating	Spin coating (500 rpm 5sec. → 1700 rpm 30 sec.)

6	Soft bake	Hot plate 95 °C, 60 min.
7	Cooling	Room temperature 5 min.
8	Exposure	Vacuum contact, align gap 50 μm, 17 sec. intensity:20mJ, Power 1080 watt, 20 mW, 365(i-line)
9	Post-exposure bake	Hot plate 65 °C, 1 min. → 95 °C, 6 min.
10	Cooling	Room temperature 5 min.
11	Development	AZ MIF 300, 15 min.
12	Inspection	Isopropyl alcohol 3 min.
11- 1	Final development	Dependent on the result of inspection AZ MIF 300, 1 min.
13	QDR, rinse & dry	D.I water rinse and dry
14	Microscope inspection	Inspection

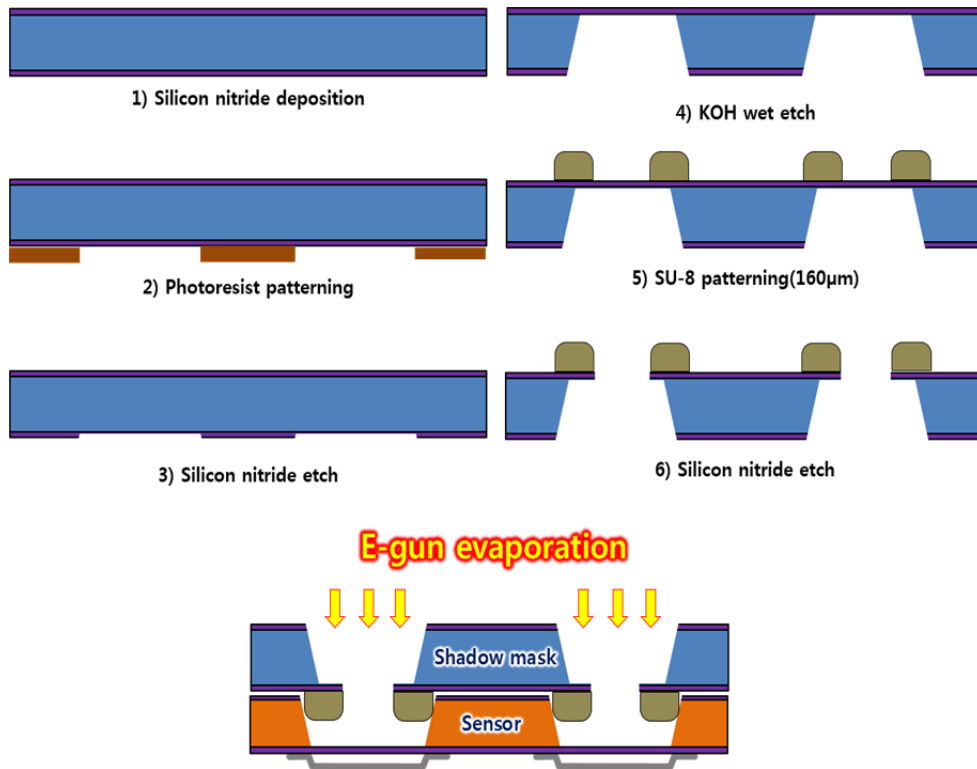


Figure 3-19. Fabrication process flow for the self-aligned shadow mask using SU-8.

The schematic description of this modified fabrication process is provided in Figure 3-19. A thick silicon nitride film is used for shadow membrane deposited LPCVD and then a membrane pattern is calculated and fabricated with photolithography. Consequently, the silicon nitride membrane is floated with silicon nitride dry etch and potassium hydroxide silicon wet etch. The 160 µm thick SU-8 pillars developed with the recipe of high aspect ratio are patterned on top of the floating membrane. Lastly, the geometry of shadow mask pattern is etched to silicon nitride membrane by using the mask of SU-8 pattern.

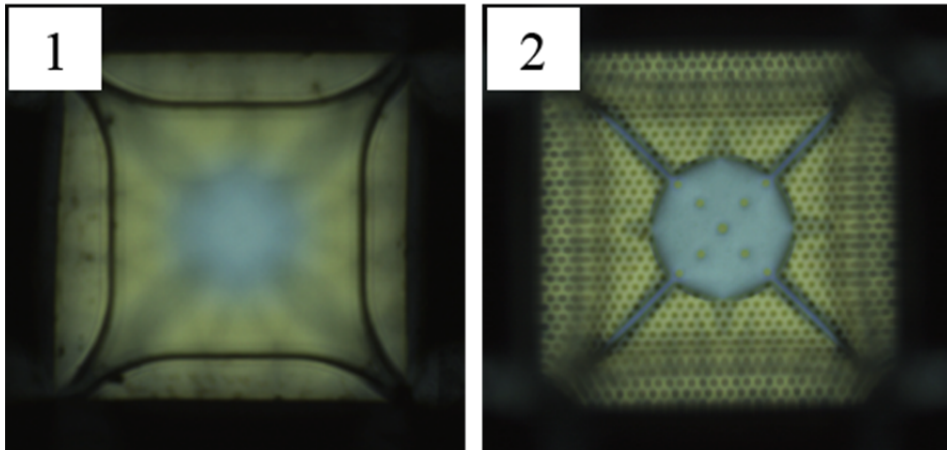


Figure 3-20. Optical image of self-aligned shadow mask.

The pillars facilitate the alignment of the shadow mask on the lower electrode of membrane transducer described in figure 3-20, More importantly, the pillar prevents the sliding event of the wafer even in vacuum condition during metal deposition process. In addition, the pillar structure enables a well-defined metal deposition that produces metal layer with distinct edges as shown in figure 3-21.

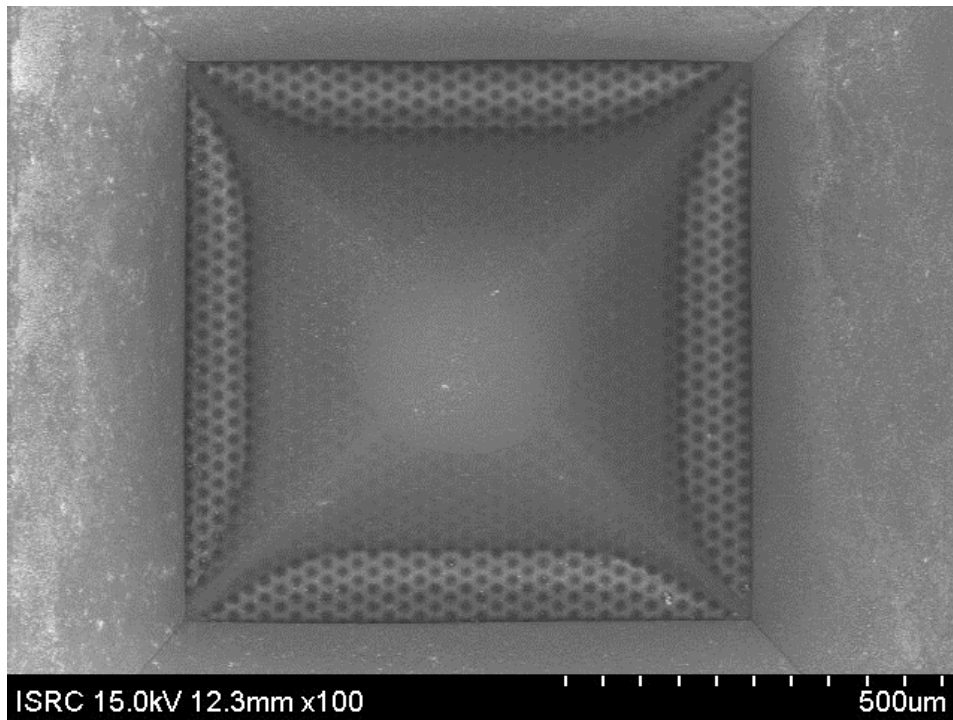


Figure 3-21. Reaction gold deposited with self-aligned shadow mask is in the 500 μm depth from the wafer surface.

3.1.3 MEMS Sensor Packaging

Since MEMS often includes moving structures, the packaging requirements of such components must take this into account. Some functions also include interaction with the surrounding environment through pressure sensors, for example[14]. In normal microelectronics, these carry out new requirements on packaging, because the chip must be shielded completely from any damage from the environment. Packaging also supports floated mechanical elements of the sensitive chip in order

to facilitate handling and simplify assembly. The most distinctive difference between packaging MEMS devices and other microelectronics is that MEMS are more often required to be in contact with the functional environments such as volatile organic compound (VOC) gas and bio-medium liquid. Most integrated sensors and circuits require capsulation to gain mechanical support, protect themselves against the environment, as well as facilitate mounting on circuit boards and easy handling of the individual chip. In the case of MEMS devices, they have to be protected at the wafer level in order to protect the structure from water and particle impingement during the dicing process. A higher level of integration will be required in future sensor systems because different sensor elements, electronics and measurement circuits or optical filters for optical sensors as well as fluidic elements for biological and chemical sensors will be combined together.

In the early stage of the sensor fabrication, the low throughput of the sensor allows only single sensor produced on every chip. The dimension of the sensor is 1 mm x 1 mm. A rigid substrate is needed to support the brittle sensing membrane and the wire bonding pad. In almost every kind of biomolecule detections, leakage must be avoided in the liquid chamber or channel. Figure 3-22(a) is the schematic drawing of a glass substrate on which the electrode pads and the sensor are mounted.

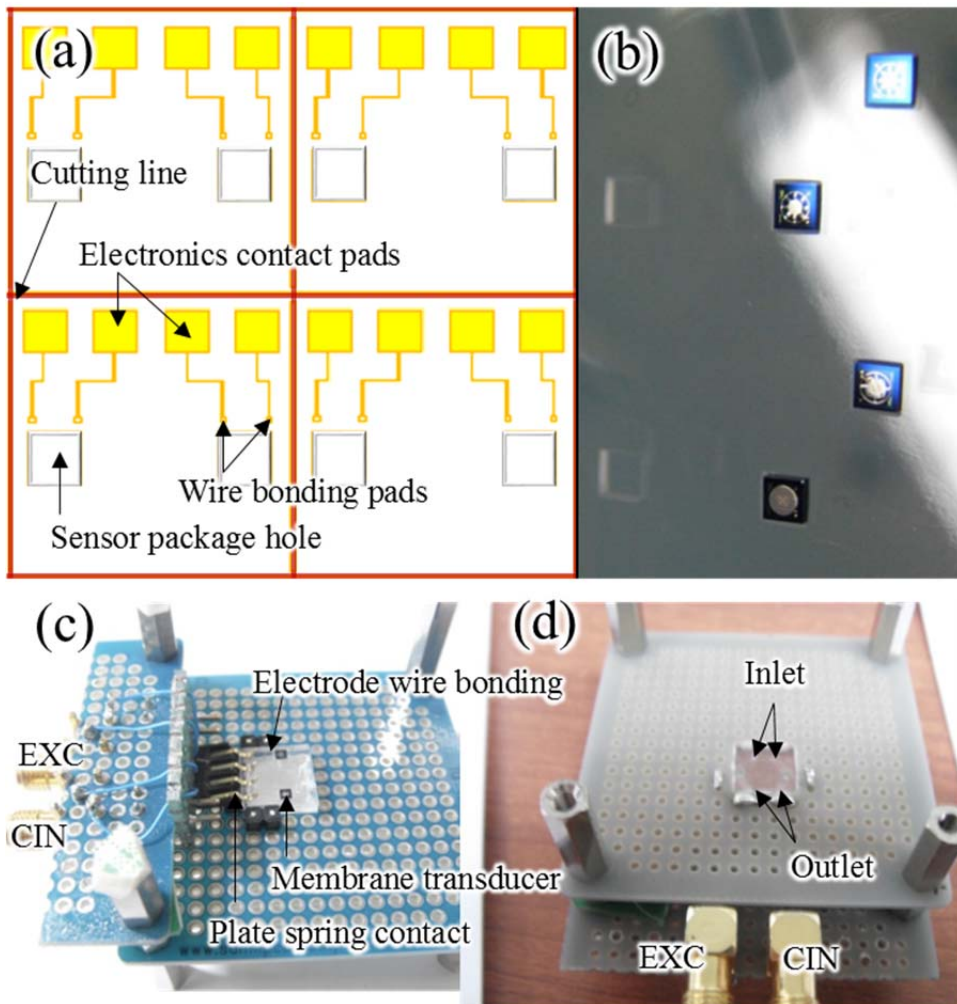


Figure 3-22. First prototype of membrane transducer system: (a) MEMS sensor holder with the circuits of measurement, (b) the glass holder with transducers and electrode lines, (c) measurement set-up and (d) micro-fluidic channel on top of the package.

Sand blasting technique is employed to make holes to accommodate the sensor chip on the glass substrate, as shown in figure 3-22(b) and the complete packaging is shown by figure 3-22(c). The measurement package utilizes plate spring to fix

the sensor and make contact with the electrode pads. Micro fluidic channel is integrated with the sensor system, shown in figure 3-22(d).

Mass production of membrane transducer is possible when the yield of the fabrication process increases. Figure 3-23 reveals the printed circuit board used to house AD 7746, a capacitance to digital converter which is being connected with sensor to prevent the distortion of the analogue signal. Moreover, there is a stabilizing circuit that controls the driving voltage in the measurement chip so as to reduce the system noise. A 3 cm x 2 cm integrated system, consisting of micro fluidic channel, capacitance measurement circuit and membrane transducer array is shown in Figure 3-24. In addition to good portability, the system is highly sensitive in the detection of specific molecular interaction.

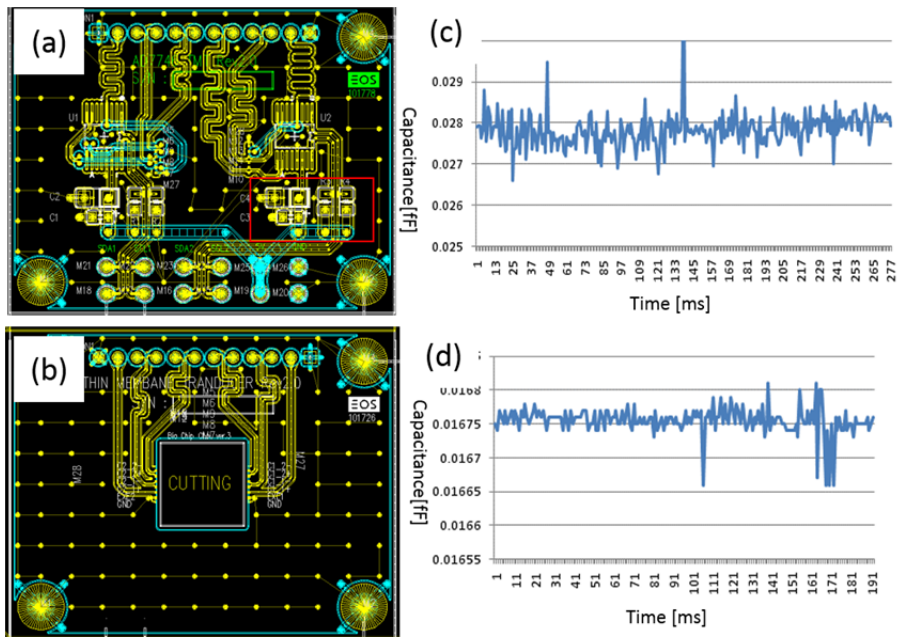


Figure 3-23. (a) The PCB circuit with stable driving voltage logic, (b) The PCB MEMS sensor, (c) The second PCB noise peak to peak 2 fF and (d) 3rd PCB peak to peak noise 100 aF.

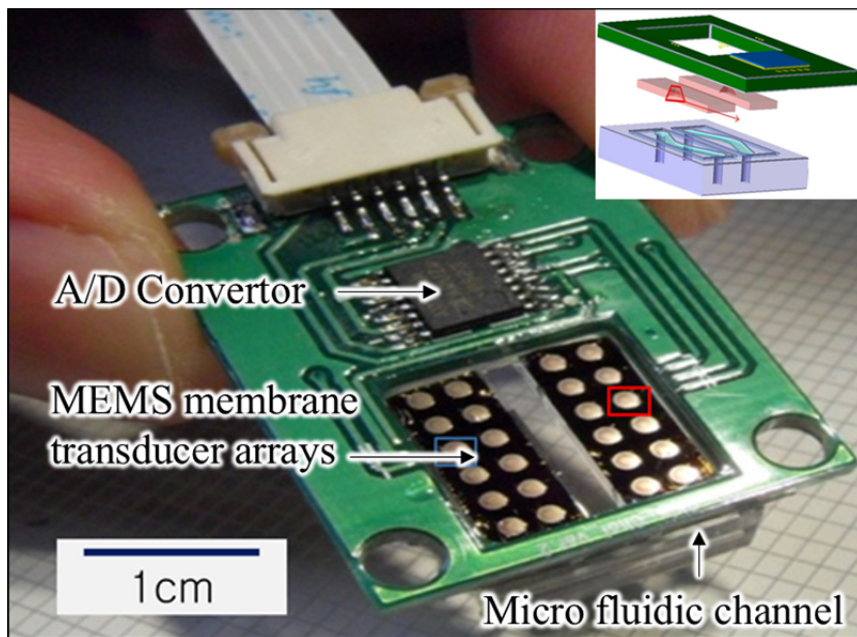


Figure 3-24. Photo image of packaged membrane-based capacitive transducer system

3.2 Receptor Molecular Structure

Chemical self-assembly indicate the spontaneous organization of substance at the molecular scale. In the nature of biological system, various self-organized system establish quite complex in their environmental conditions. Scientists make useful structures for a variety of applications to harness the advantages of chemical self-assembly. The surface functionalization of thiolated SAMs is widely being used to increase the specificity of chemical and biological sensing application.

Normally, a receptor molecule immobilize the whole area of cantilevers to increase the surface stress, but the membrane of whole surface covered with a receptor is not deflected due to the lateral force of molecular interactions described in chapter 3.1.1.1. Molecular immobilization on a specific region is researched for the membrane transducer utilizing partially covered gold layer. Especially, our membrane transducer of integrated with both surface and bulk micromachining cannot use the harsh cleaning processes such as piranha, peroxide and oxygen plasma before the molecular immobilization. Therefore, we have to develop the special molecular structure to protect contamination and enhance the surface stress of molecular interaction.

3.2.1 Self-Assembly Monolayer

Gold is easily contaminated under ambient laboratory air due to micro oil bubble from vacuum pump. The contamination of surface for molecular interaction indeed has an effect on reliability of sensor performance. Also, irregular exposed gold surface can affect surface stress. In figure 3-25, the surface stresses are affected by a function of potential for a dodecanethiol self-assembly monolayer (SAM) modified gold layer 3-25(a), a defective SAM (less than 100% coverage; sub-monolayer) 3-25(b) and a clean bare Au surface 3-25(c) and (d). The highly organized SAM modified gold surface does not adsorb ions which take place to compensate the adsorption of anions for the positive charging of the gold surface that cause a compressive change. The relatively high affinity of alkanethiols for gold is enough to displace weakly bound contaminants from the gold surface as forming the SAM. [15] Alkanethiol $[\text{HS}(\text{CH}_2)_n\text{CH}_3]$ self-assembly monolayers (SAM) are one of the most widely studied self-assembled systems for their versatility and stability.

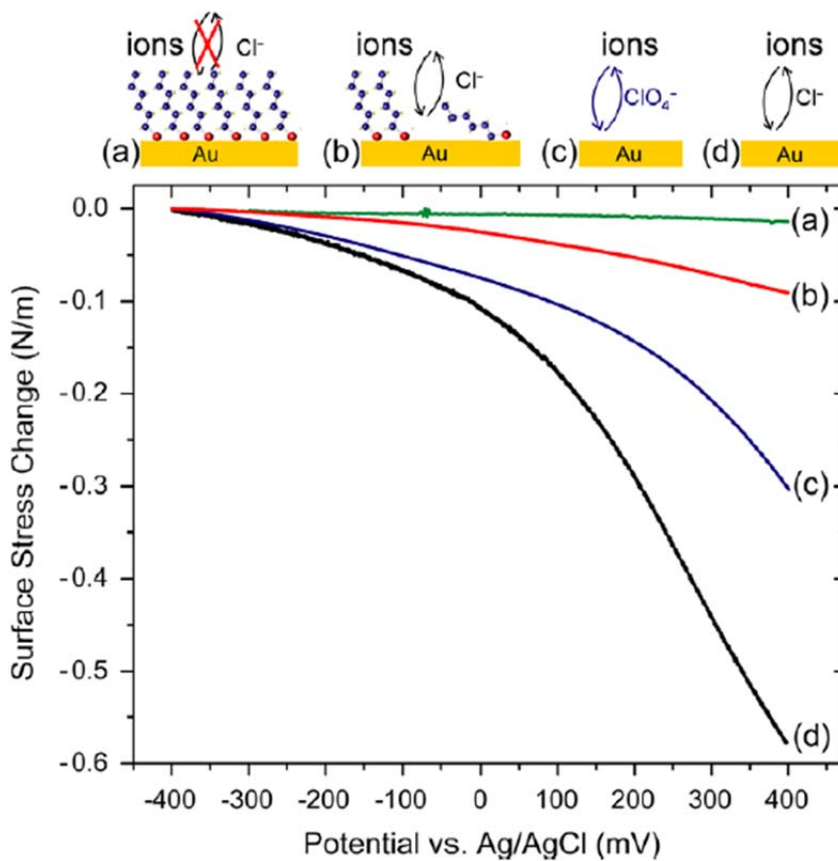
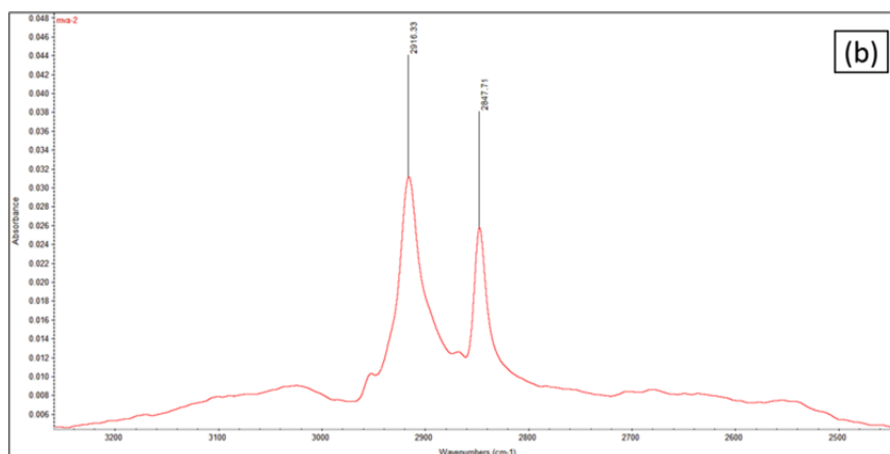
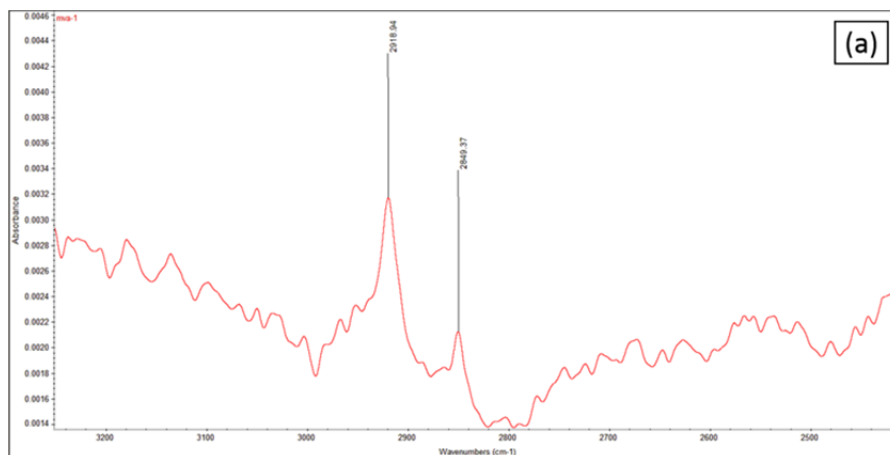


Figure 3-25. Change in the surface stress because exposed gold surface is reacted with ions. (a) a SAM modified Au, (b) defective SAM layer, (c) bare gold layer in 100mM HClO₄ and (d) bare gold layer in 100 mM NaCl. The change in surface stress values are arbitrarily set to zero at the most negative potential.

It is well known that 11-mercaptoundecanoic acid (MUA) has high binding affinity on the gold surface and it can withstand high temperature around 300°C during the transducer system packaging process. Besides, 11-MUA has carboxylic acid end terminal which binds with amine group through peptide bonding. After micromachining process, ethanol based-4mM 11-mercaptoundecanoic acid, 95% (Aldrich 450561) is coated onto the gold surface of the membrane transducer at 4°C for 12 hours, to prevent contamination on the surface. It is a crucial step to

remove non-specific binding of molecule on the gold surface through stringent washing with 100% ethanol before the development of 11-MUA monolayer.

The binding of 11-MUA on the gold surface can be verified with Fourier Transform Infrared Spectroscopy (FTIR). FTIR is a technique used to obtain an infrared spectrum of absorption, emission, photoconductivity or Raman scattering of a solid, liquid or gas[16]. Figure 3-26 contains the FTIR data of the 11-MUA molecules bound on the reaction gold surface. From the graph in figure 3-26(a), small signal implies that 11-MUA forms a monolayer on the surface after ethanol stringent washing. While bundle type 11-MUA produces larger signal, as shown by the graph in figure 3-26(b), both measuring result show two peaks at 2850 and 2919 wavelength which is an indication of the binding of 11-MUA on the gold surface 3-26(c).



(c) Spectral Mode Assignments for 11-MUA SAMs on Au(111)/Mica

freq, cm^{-1}	mode assignment
2919	CH_2 stretch, asymm.
2850	CH_2 stretch, symm.
1710	$\text{C}=\text{O}$ stretch
1468	CH_2 deformation
1435	$\text{C}-\text{O}-\text{H}$ deformation

Figure 3-26. FT-IR measured spectra of an 11-MUA SAM on reaction gold with the position of the CH_2 stretch vibrations at 2919 cm^{-1} and 2850 cm^{-1} , respectively, indicate a well-defined SAM. (a) ethanol washing (b) D.I washing and (c) spectral mode table for assignments of 11-MUA SAMs on Au (111)/mica[17]. The $\text{C}=\text{O}$ stretch vibration is observed at 1710 cm^{-1} . The peak at 1435 cm^{-1} is due to the $\text{C}-\text{O}-\text{H}$ deformation vibration; the feature at 1468 cm^{-1} is attributed to CH_2 deformations

3.2.2 Effect of Gold Surface

Thiol adsorption extracts the extra gold atom at the surface that cause a reconstructed Au (111) surface. Gold surface highly affect arrangement of self-assembly layer as well as surface stress. M. Godin et al[18] refute an argument that the surface stress at monolayer coverage increased linearly with the length of the alkyl chain of the molecule shown as figure 3-27[19]. The mean steady-state surface stress resulting from different length of alkanethiol chain do not play a significant role in generating the observed large surface stress, but the grain size on gold surface determines the amount of surface stress. This is because uniform adsorption of molecules takes place on gold surfaces with large and flat grains, results in a high-quality self-assembled monolayer. Scanning tunnelling microscope is used to investigate the effect of the alkanethiol monolayer area on the surface stress. It is showed that alkanethiol Sam has large area lattice if the grain size increases. From the experimental data, an equation relating surface stress with the grain size on the gold surface is obtained.

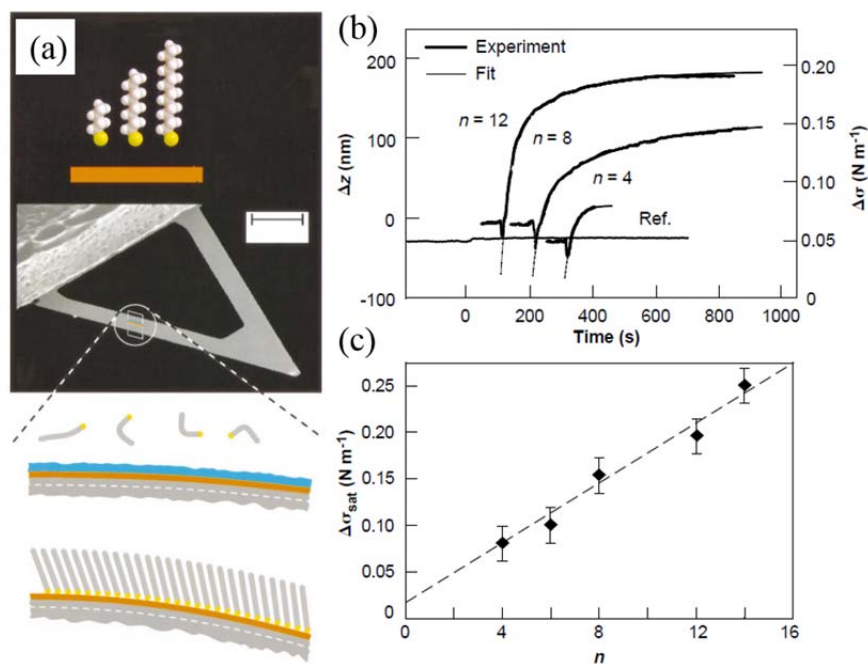


Figure 3-27. SEM image of the Au-coated SiN_x cantilever showing the sensor's receptor surface and deflection due to surface stress induced by binding alkanethiol molecule on the gold surface[19]

The surface stress is measured using a micro-cantilever sensor, and simultaneously in situ thickness measurements are carried out using ellipsometry. Two main types of gold surfaces are prepared: surfaces with a relatively small average grain size and surfaces with a large average grain size. Small-grained gold surfaces are prepared by thermally evaporating 100 nm of gold at a rate of 0.14 nm/sec. Although the substrates are not pre-heated before the start of the evaporating gold surface, the radiative heating energy of the evaporation increased the wafer substrate temperature to $130 \pm 20^\circ\text{C}$. When the substrates are heated to $260 \pm 10^\circ\text{C}$, the gold surfaces show a larger grain size by the end of the evaporate ion. All evaporations are conducted with a base pressure better than 1.0×10^{-5} Torr. Figure 3-28 shows the STM images of (a) gold with large grains (600 ± 400 nm) and (b)

gold with small grains (90 ± 50 nm). The real-time thickness profiles of the dodecanethiol SAMs are similar with both case described in figure 3-28(c), but simultaneous surface stress reveal that the SAMs formed on these two gold surfaces has distinctive difference plotted in figure 3-28(d), which reveals that the surface stress of the small grain size surface is ignorable. The surface stress on the large-grained gold continues to increase for about 10 hours into a final value of 16 N/m, while the small-grained gold express a slight increase in surface stress into a final value of 0.5 N/m in minutes.

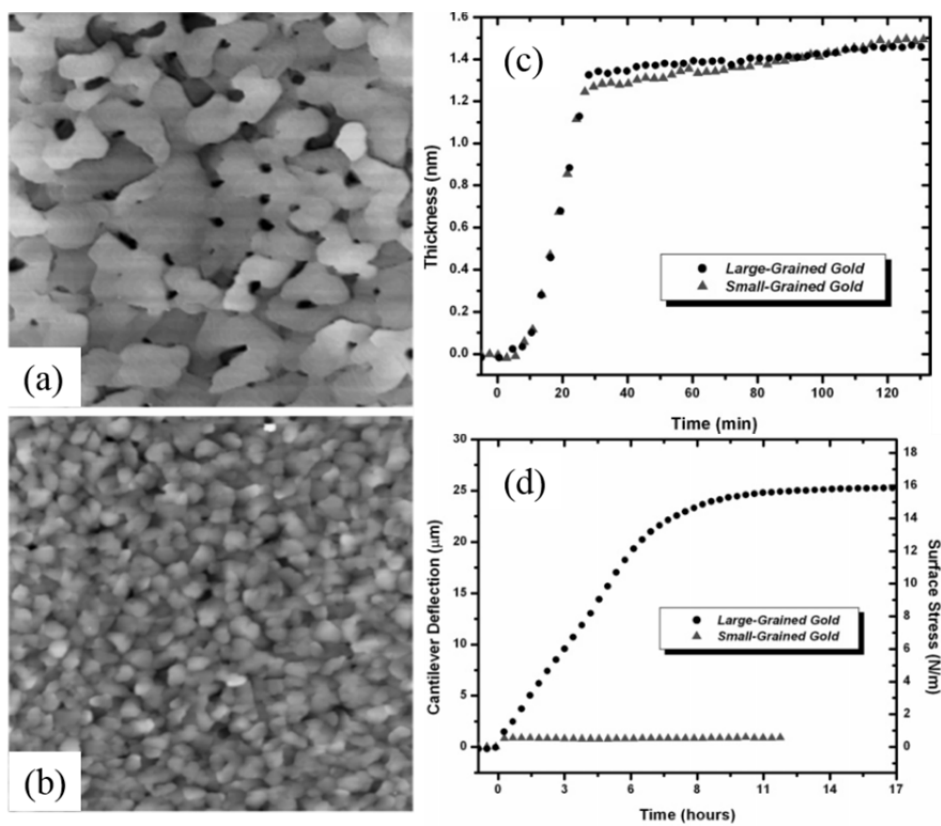


Figure 3-28. Compare the STM images ($3\mu\text{m} \times 3\mu\text{m}$) of (a) large-grained gold and (b) small-grained gold, (c) real-time thickness profiles of the dodecanethiol SAMs and (d) the surface stress induced during the formation of dodecanethiol SAM on gold-coated cantilevers[20].

Therefore, it becomes important to obtain large grain gold surface, which is achievable by manipulating the vacuum pressure and the temperature in the chamber. The grain size can be effectively enlarged by lowering the vacuum pressure, but this will lead to low uniformity problem. Due to the limitation of the equipment, the grain size enlargement is not observable at low chamber temperature. Atomic force microscope is used to identify the grain size of the gold layer. The 3-dimensional graphic is shown in figure 3-29.

Condition	Pressure (Torr)	Dep. Rate ($\text{\AA}/\text{sec}$)	Temp. ($^{\circ}\text{C}$)	Grain size (nm)
1	5×10^{-6}	20	RT	10 ± 20
2	2×10^{-5}	20	RT	50 ± 30
3	2×10^{-5}	20	120	50 ± 30
4	2×10^{-6}	20	120	30 ± 20

Grain size ($1\mu\text{m} \times 1\mu\text{m}$)

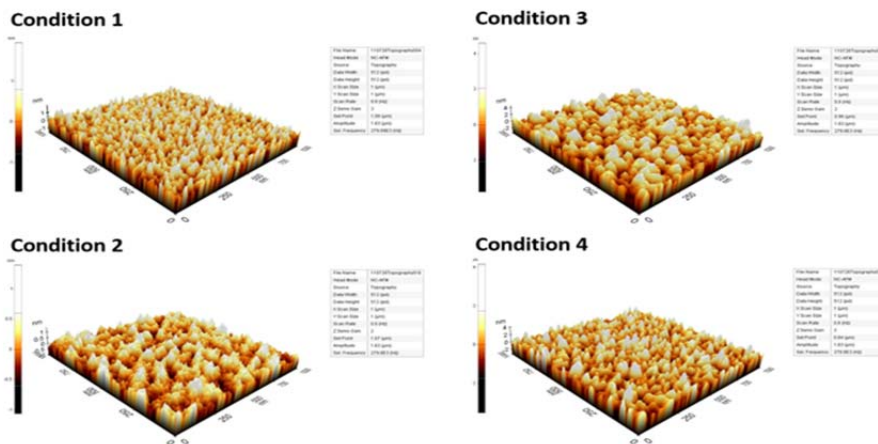


Figure 3-29. Different condition of evaporating gold source during the deposition of gold layer and the AFM image of gold surface to check grain size.

3.2.3 Molecular Immobilization

Biomolecule immobilization on gold surface is not common in biology and chemistry fields. In the 70's, it has been accepted that molecular immobilization on solid surface has several advantages. It makes the detection more sensitive and selective because the receptor molecules are concentrated on the specific area that increases the efficiency of molecular interaction through Langmuir isotherm model. Also, the recognition events can be generated at the precisely localized area in order to satisfy the specificity of a biosensor application. Particular surface chemistries are required to control the immobilization so as to maintain biological activity and minimize nonspecific adsorption.

Molecular immobilization experiment is performed on a 100 nm gold layer coated on glass slide, where thiol-modified single strand DNA is spotted with conventional micro array technology. Figure 3-30 shows the fluorescence signals after stringent washing, of which non-thiolated ssDNA is hardly visible; while thiol-modified ssDNA covalently bound with gold, shows fluorescence signal. Using the microarray standard protocol for washing shown as table 7, unlike on commercial microarray chip, the binding detachment of thiolated ssDNA from the gold is observed. Figure 3-31 presents the dependence of the fluorescence signal intensity on the length of the probe, after washing with 1x PBS and deionized water. From these experiments, it is clear that thiolated ssDNA has low binding efficiency on gold substrate, which justifies the use of 11-MUA.

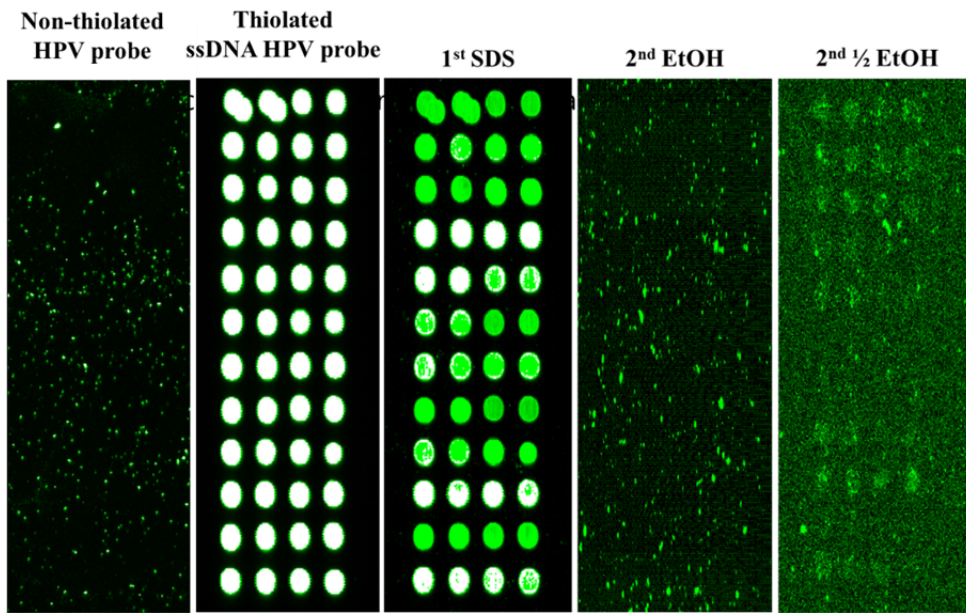


Figure 3-30. Fluorescence result after microarray standard washing.

Table 7. Microarray standard recipe for washing

Process	Solution	Volume /Conc.	Time (min.)
1	0.1% SDS	250 ml/ 0.1%	5
2	Deionized water	250 ml	5
3	Deionized water	250 ml	5
4	NaBH ₄ (0.625g) + 1x PBS 187.5ml + EtOH 62.5 ml (10 x PBS 18.75ml + Deionized water 168.75ml)	250 ml	5
5	Deionized water	250 ml	5
6	Deionized water	250 ml	5
7	Centrifuge – 800 RPM	-	5

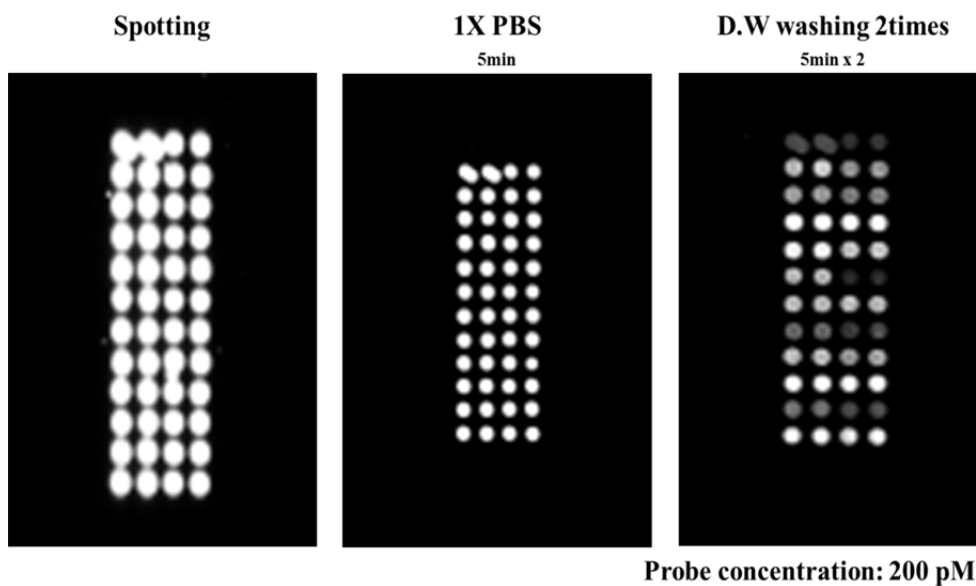


Figure 3-31. Fluorescence results after PBS and distilled water washing.

In the figure 3-32, the eight gold spot is patterned on a slider glass to examine molecular binding efficiency. 11-MUA is immobilized on the gold spot, and then the carboxylic function of 11-MUA is connected with 3 different amine terminated ssDNA probe which vary in 3, 6 and 12 thymine [T] spacer linker between amine and oligonucleotides. For identifying the efficiency of molecular interaction, target protein is conducted with mono-biotinylation and the protein reacts with the probes. The biotin of target protein is bonded with Cy-3 modified streptavidin through bicinchoninic acid (BCA) assay method, which is the highly quantitative data from fluorescence optical measurement as depicted in table 8. Immobilization density at each slide is very uniform, but the longer DNA has high bonding because the amine chain of DNA is reacted with non-specific adsorption at the 11-MUA. Also,

the efficiency of molecular interaction is the highest intensity of fluorescence at the 6 spacer linker and 100 ng/ml concentration of target molecule.

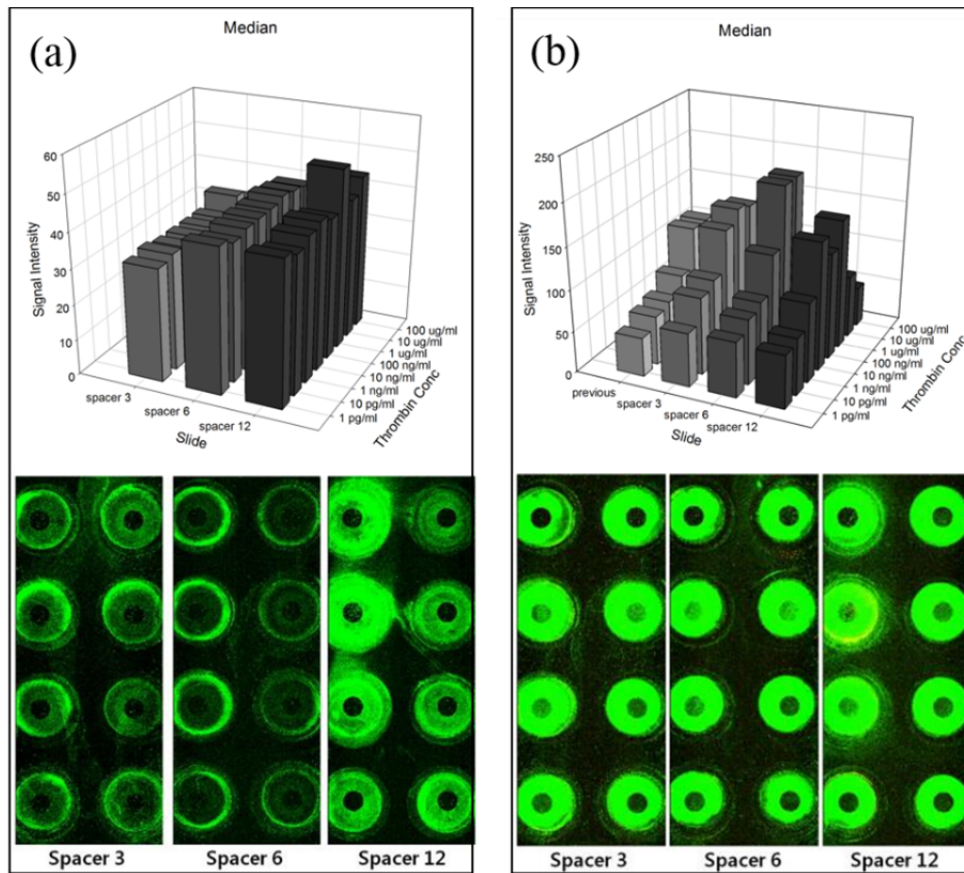


Figure 3-32. Fluorescence scan image and signal intensity after (a) immobilization and (b) protein interaction.

Table 8. Molecule interaction efficiency with median signal intensity after target molecules are interacted with probe.

Target Protein Concentration	spacer 3	spacer 6	spacer 12
1 pg/ml	65	67	64
10 pg/ml	93	79	69
1 ng/ml	101	86	96
10 ng/ml	148	129	154
100 ng/ml	162	198	128
1 ug/ml	155	198	156
10 ug/ml	49	56	75
100 ug/ml	41	45	48

However, the fluorescence signal out of gold spot is stronger than that of gold region because of non-specific adsorption. Therefore, we utilize the molecular ladder of maleimide to increase the selectivity of peptide bonding and a thiolated ssDNA probe also increase the selectivity.[21] The protocol is used for the receptor structure of thrombin binding aptamer intimately described in chapter 4.4.

3.3 Capacitive Measurement System

3.3.1 Analogue to Digital Converter

Electronic system measures the capacitance of membrane transducer and converts it into digital signal in figure 3-33. The capacitance to digital converter (CDC) chip of AD7746, Analog-Devices Inc., is utilized in the measurement system with low pass filter. The CDC chip measures capacitance by using switching capacitor technology to build up a charge balancing circuit. As charge is proportional to the product of voltage and capacitance, $Q = V \times C$, the conversion result represents the ratio between the input capacitance, C_{SENS} , and the internal reference capacitance, C_{REF} , as the excitation voltages EXC_x and the internal reference voltage V_{REF} have fixed known values [22] depicted in figure 3-34. The measurement principle is equivalent resistor model for switched capacitor circuit.

$$R_{eq} = \frac{V_1 - V_2}{I_{avg}} = \frac{1}{C \cdot f_{clk}} \quad \text{Equation 3.3.1-1}$$

The capacitance value is inversely proportional with frequency of clock. In the circuits like as figure 3-35, a low-level high frequency measurement signal is applied to the driven node of the device. If the membrane transducer has some chemo electric effects because of high aspect ratio between very large area ($70650 \mu\text{m}^2$) and just $2 \mu\text{m}$ distance gap of electrodes. To reduce the effect of circuit noise, voltage excitation (EXC) node has been connected with lower electrode.

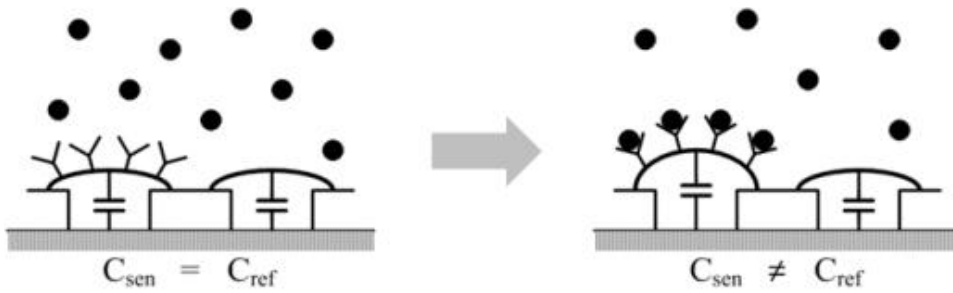


Figure 3-33. Schematics of membrane transducer system.[23]

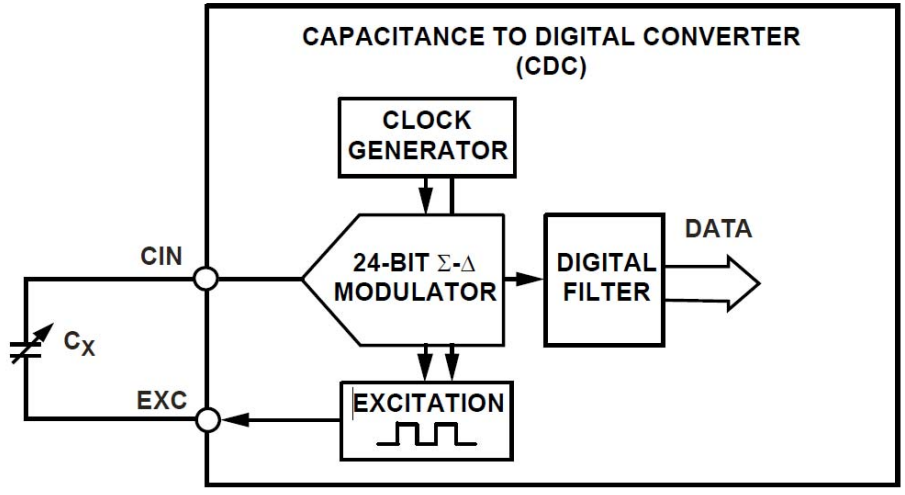


Figure 3-34. CDC simplified block diagram in AD7746 chip.[24]

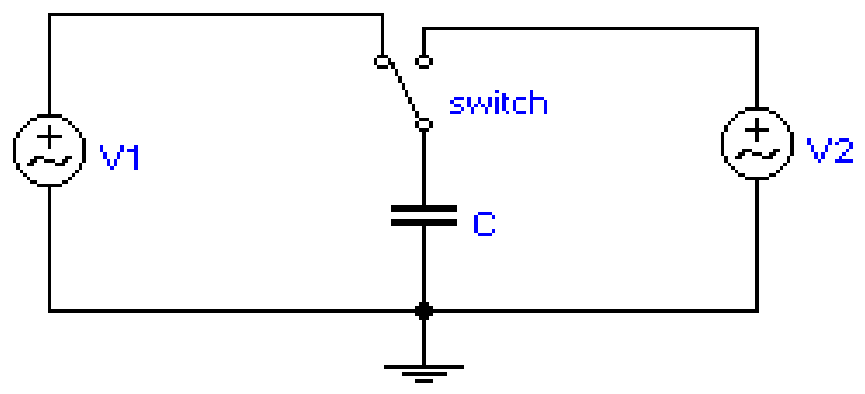


Figure 3-35. Equivalent resistor model for switched capacitor circuit

High pass filter circuit has a clock delay as time constant changes described in figure 3-36. The time constant is related with capacitance in (CIN). Therefore, the CDC chip confuses the change of capacitance value (C_m) rather than resistance because notwithstanding fixed resistance R_{ref} , the total resistance is changed due to charge leakage on the electrode explained in equation 3.3.1-2.

$$Q = Q_0(1 - e^{-\frac{t}{R_{ref} \cdot C_m}}) \quad \text{Equation 3.3.1-2}$$

where R_{ref} is fixed resistance of $1M\Omega$ and C_m is the measured capacitance value. In the p-spice simulation, the measurement circuit is drawn as figure 3-37. Green probe is input voltage excitation and the red probe is output signal in ideal mode circuit. Blue one is EXC signal connected with lower electrode. Pink and yellow probe indicate charge leakage when CIN is connected to lower electrode. Simulation result shows that the time constant is dramatically changed as the resistor, which is connected to CIN, decreases from $200k\Omega$ (yellow) to 200Ω (pink) in the input square voltage like figure 3-38. The time constant is like the equation 3.3.1-3 in RC circuit.

$$\tau = R \times C \quad \text{Equation 3.3.1-3}$$

In this equation, leakage resistance changes included in circuit total resistance induce the noise of capacitance change without chemical interaction because the circuit recognize capacitance change rather than fixed resistance. Therefore, lower electrode of the membrane transducer is connected with EXC node, and upper electrode is connected with CIN node. However, the noise signal from the charge

leakage can be ignored because the resistance between ground and electrode is very stable with $100\text{M}\Omega$ in real sensor system like figure 3-39.

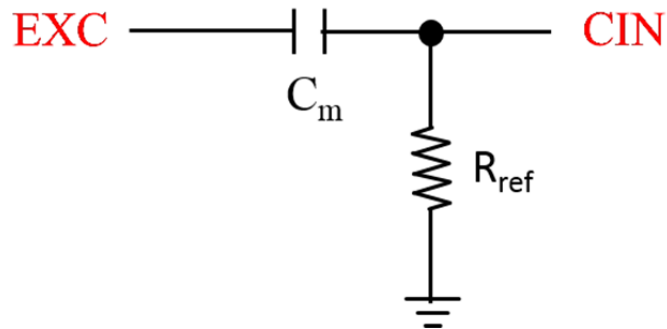


Figure 3-36. High pass filter (HPF) circuit.

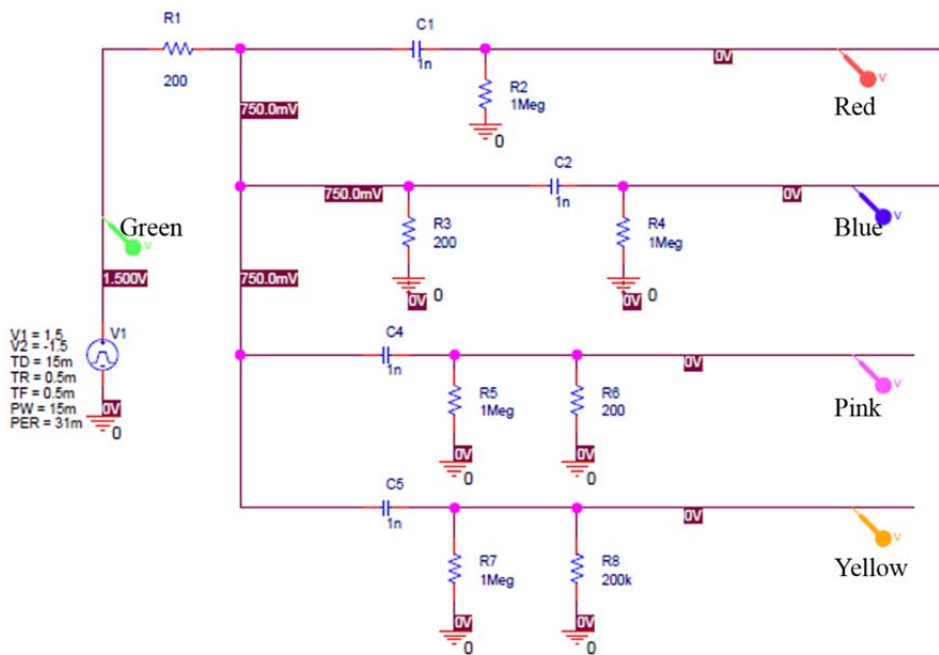


Figure 3-37. P-spice simulation of measurement circuit.

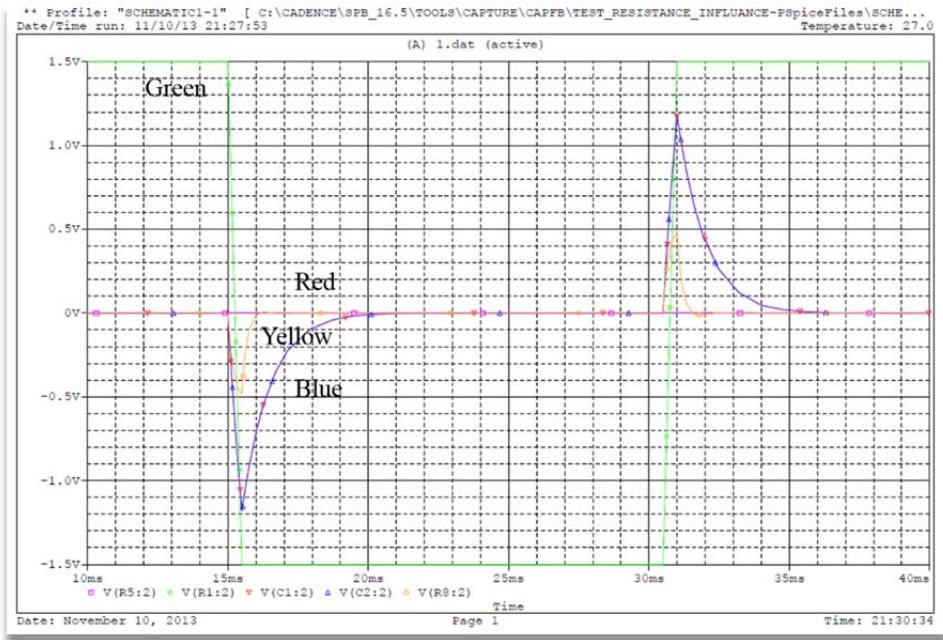


Figure 3-38. Simulation results for stable circuits.

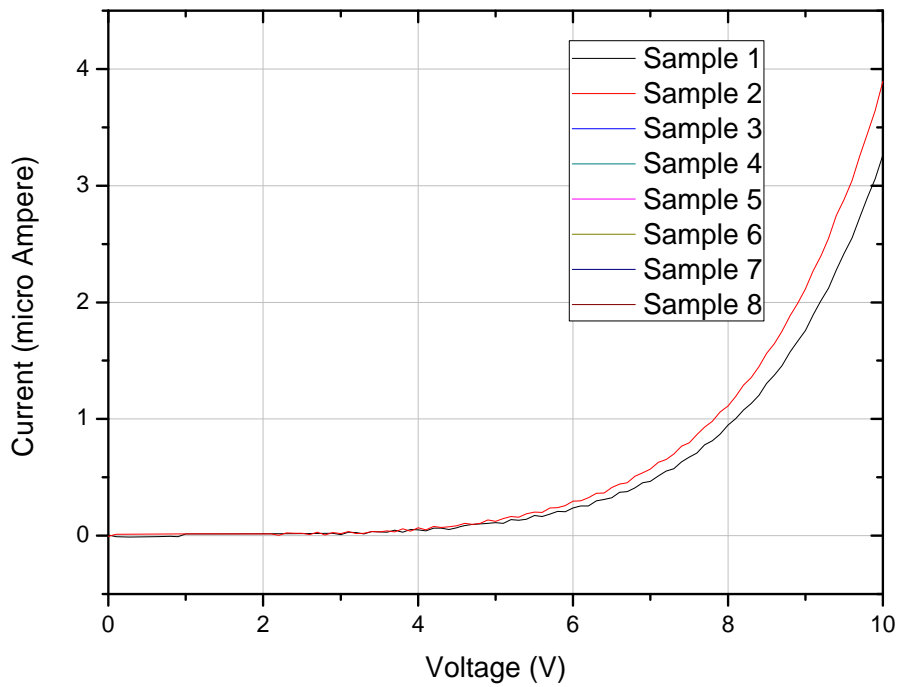


Figure 3-39. Current vs. voltage curve between Ground and lower electrodes.

3.3.2 Capacitive Measurement Circuit

These days, most sensor systems have to detect simultaneously multiple biomarker to increase sensitivity of the screening test for early diagnostics. A single membrane transducer measure the signal from one biomarker interaction, so we design the transducer array for the system, which can detect hundreds of biomarker at every second because of electrical measurement. The capacitance measurement system play a role to control the CDC connected with membrane transducer and gather the capacitance digital data. Figure 3-40 describe the block diagram of capacitive measurement system.

The micro-processor use the I²C standard communication to control the CDC (AD7746) with SDA (Serial Data) and SCL (Serial Clock) signal, and the multiplexer change the serial port to connect array transducer. Micro-processor select the number of channel to communicate signal and commend measurement method for the AD7746 IC. The AD7746 has memory register where the capacitance value is stored with digital data. The data is transferred with USART standard communication to virtual COM Port (VCP) IC. The VCP IC change the signal from USART communication to USB communication, and deliver the transformed signal to PC. In the PC, window graphical user interface (GUI) is developed with C# language to embody the functions such as real-time graph, signal processing and file recording. The USB form signal is connected with serial port of GUI. Also, the GUI can commend the functions of CDC like as measurement method, velocity and data filtering.

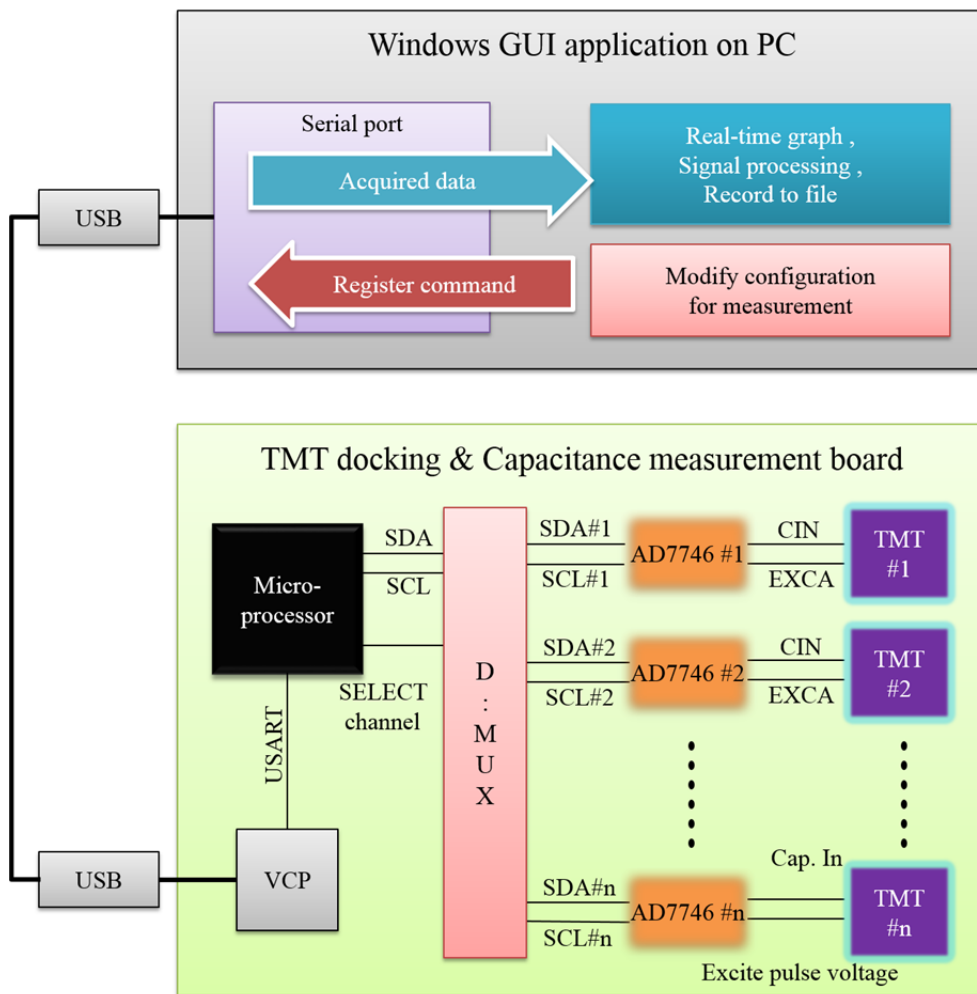


Figure 3-40. Schematics of overall measurement system included with hardware and software.

Figure 3-41 show the hardware layout of capacitance measurement circuit with small module, and figure 3-42 is manufactured measurement circuit. The prototype can measure simultaneously two CDC connected with membrane transducer utilizing MUX. The measurement circuit use the 2.54mm pinch standard Pin-socket to easily replace membrane transducers and choose the power source to get more stable signal ether USB power or 5V adaptor.

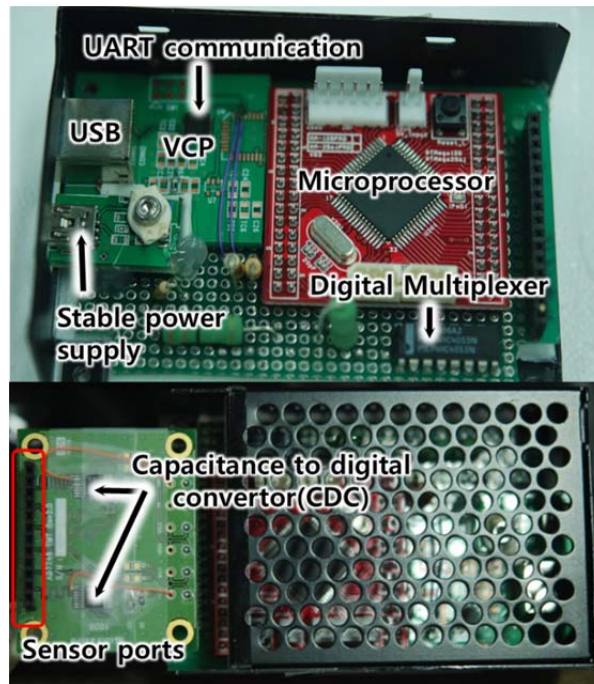


Figure 3-42. Differential capacitance measurement system.

GUI has 2 page with separating tab described in figure 3-43. The first tab show the real-time data with graph from the acquired data of CDC and the signal is displayed after IIR-filtering of raw data. There are two channel and differential signal of two data. Moreover, data acquisition, sensor mode and data save velocity are immediately changed in this page. Another tab has a lot of function mode with CDC. The capacitance measurement port configuration, AC level voltage and temperature controls are controlled. Also, we can see the register value of CDC and change the value of digital data such as capacitance measurement mode, sampling rate, conversion time, offset and gain. Especially, the differential measurement mode is much more appropriately suited for sensing in liquid environments, where common mode rejection is very important to obtain a good signal-to-noise ratio.

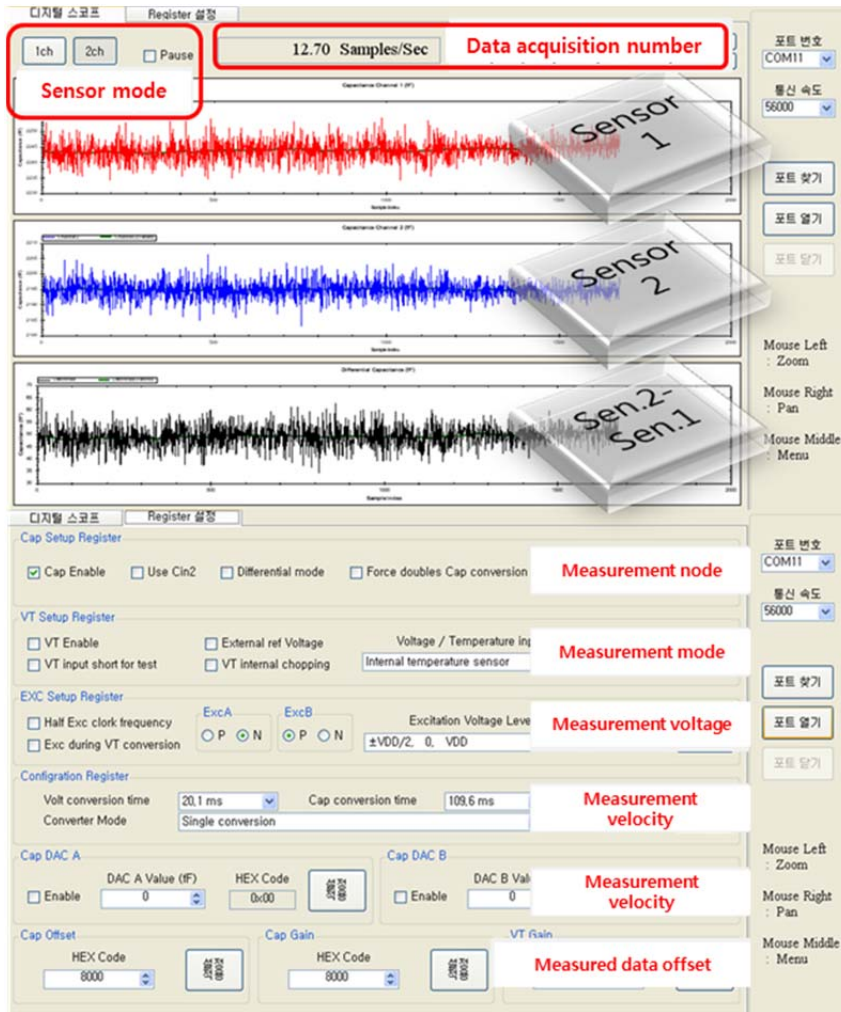


Figure 3-43. Window Graphical-User-Interface(GUI).

3.4 References

1. Lee, J., *Microactuation by Continuous Electrowetting and Electrowetting: Theory, Fabrication, and Demonstration*, in *Mechanical Engineering* 2000, University of California, Los Angeles.
2. Bao, M., et al., *Squeeze-film air damping of thick hole-plate*. *Sensors and Actuators A: Physical*, 2003. **108**(1–3): p. 212-217.
3. Alexander Bietsch, J.Z., Martin Hegner, Hans Peter Lang and Christoph Gerber, *Rapid functionalization of cantilever array sensors by inkjet printing*. *Nanotechnology*, 2004. **15**: p. 873–880.
4. Arun Majumdar, S.-H.L., *Compensated membrane capacitive bio-chemical sensor*, T.R.O.T.U.O. California, Editor. 2007: US.
5. Stoney, G.G., *The Tension of Metallic Films Deposited by Electrolysis*. *Proceedings of the Royal Society of London. Series A*, 1909. **82**(553): p. 172-175.
6. DelRio, F.W., et al., *Elastic and adhesive properties of alkanethiol self-assembled monolayers on gold*. *Applied Physics Letters*, 2009. **94**(13): p. -.
7. Kobayashi, D., C.-J. Kim, and H. Fujita, *Photoresist-Assisted Release of Movable Microstructures*. *Japanese Journal of Applied Physics*, 1993. **32**(Part 2, No. 11A): p. L1642-L1644.
8. Hwang, H.-S. and J.-T. Song, *An effective method to prevent stiction problems using a photoresist sacrificial layer*. *Journal of Micromechanics and Microengineering*, 2007. **17**(2): p. 245.
9. Chen, S., C. Chang, and W. Hsu, *Improved model of rectangular scratch drive actuator*. *Journal of Micro/Nanolithography, MEMS, and MOEMS*, 2011. **10**(1): p.013016-013016-10.
10. Molinero, D. and L. Castaner. *MEMS switches fabrication using photoresist as a sacrificial layer*. in *Electron Devices, 2009. CDE 2009. Spanish Conference on*.

2009.

11. Homentcovschi, D. and R.N. Miles, *Viscous damping of perforated planar micromechanical structures*. Sens Actuators A Phys, 2005. **119**(2): p. 544-552.
12. Bayiati, P., et al., *Biofluid transport on hydrophobic plasma-deposited fluorocarbon films*. Microelectron. Eng., 2007. **84**(5-8): p. 1677-1680.
13. Kummamuru, R.K., et al., *A close proximity self-aligned shadow mask for sputter deposition onto a membrane or cavity*. Journal of Micromechanics and Microengineering, 2008. **18**(9): p. 095027.
14. <http://www.imego.com>. *Sensor-system packaging*.
15. Buck, M., et al., *Adsorption kinetics of n-alkyl thiols on gold studied by second harmonic generation and x-ray photoelectron spectroscopy*. Journal of Vacuum Science & Technology A, 1992. **10**(4): p. 926-929.
16. WIKIPEDIA. *Fourier transform infrared spectroscopy*. [cited 2013 Nov. 6].
17. Stettner, J., et al., *A study on the formation and thermal stability of 11-MUA SAMs on Au(111)/mica and on polycrystalline gold foils*. Langmuir, 2009. **25**(3): p. 1427-33.
18. Godin, M., et al., *Cantilever-based sensing: the origin of surface stress and optimization strategies*. Nanotechnology, 2010. **21**(7): p. 75501.
19. Rüdiger Berger, E.D., Hans Peter Lang, Christoph Gerber, James K. Gimzewski, Ernst Meyer, Hans-Joachim Güntherodt, *Surface Stress in the Self-Assembly of Alkanethiols on Gold*. Science, 1997. **276**(27): p. 2021-2024.
20. Godin, M., et al., *Surface stress, kinetics, and structure of alkanethiol self-assembled monolayers*. Langmuir, 2004. **20**(17): p. 7090-6.
21. Houseman, B.T., E.S. Gawalt, and M. Mrksich, *Maleimide-functionalized self-assembled monolayers for the preparation of peptide and carbohydrate biochips*. Langmuir, 2003. **19**(5): p. 1522-1531.
22. www.analog.com, *Extending the Capacitive Input Range of the AD7745/AD7746 Capacitance-to-Digital Converter*. 2009, Analog Devices.

23. Dong-Yong, S., L. Hyunjoong, and K. Suhwan, *Improving the Accuracy of Capacitance-to-Frequency Converter by Accumulating Residual Charges*. Instrumentation and Measurement, IEEE Transactions on, 2011. **60**(12): p. 3950-3955.
24. Devices, A., *24-Bit Capacitance-to-Digital Converter with Temperature Sensor*.

Chapter 4. System Design and Manufacturing

4.1 Membrane Transducer System

4.1.1 Temperature Response

4.1.2 Pressure Response

4.2 Common Mode Rejection

4.3 Ion Detection with Membrane Transducer System

4.3.1 Chemo-Electrical Detection

4.3.2 Chemo-Mechanical Design

4.3.3 Molecular Immobilization

4.4 Molecular Recognition with Aptamer Receptor

4.4.1 Thrombin Protein and Thrombin Binding Aptamer

4.4.2 Immobilization of Thrombin Binding Aptamer

4.4.3 Thrombin Protein Detection and FE Simulation

4.5 Reference

Chapter 4

Chemo-Mechanical Detection

4.1 Membrane Transducer System

4.1.1 Temperature Response

Thermal characterization of the sensor are performed to evaluate sensor performance and also to test if the membranes are fully released from the substrate. The thermal test chip did not have the microfluidic cover bonded to it. For the temperature test, an adjustable temperature chamber is built to maintain the sensor chip at a constant temperature. A commercially available PID controller with adjustable set-points is used to control the chamber temperature. The sensor capacitance during the temperature test is measured using an Agilent 4280a LCR meter with an excitation voltage of 1V at 100 kHz. The plot of normalized sensor capacitance versus temperature for a fully released membrane is shown in figure 4-1. The thermal response of released membrane capacitor is 9.0 fF/K. The large signal change comes from the composite membrane which is coated with metal layers of different area and shape to enhance the sensitivity. These values clearly indicate that the sensor is released.

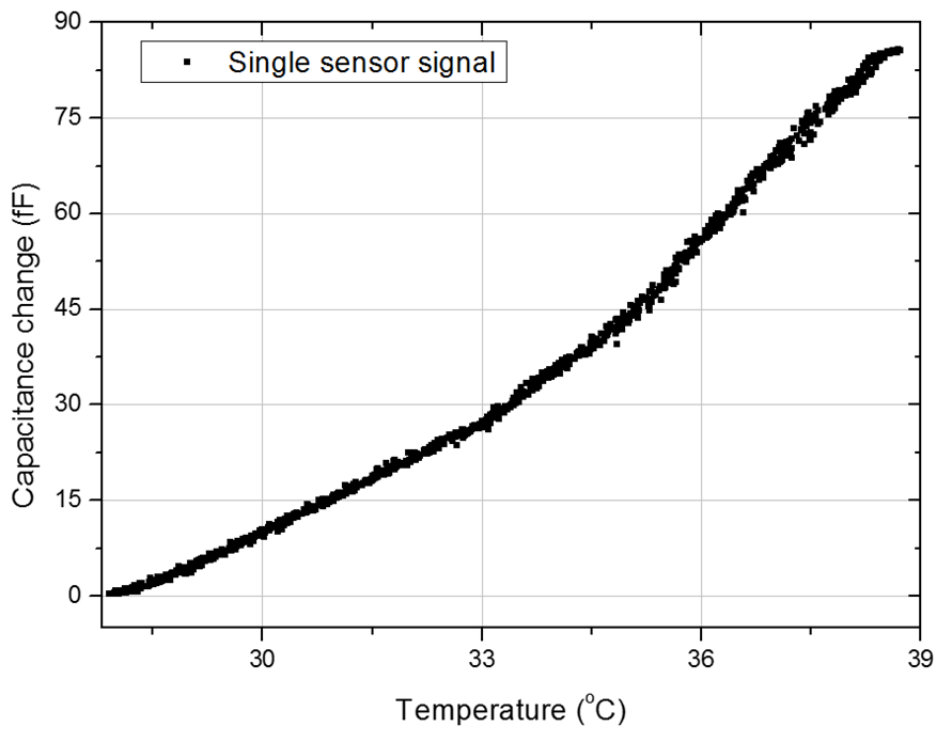


Figure 4-1. Temperature signal single sensor signal from 28 to 38 degree Celsius

4.1.2 Pressure Response

The structure of thin membrane transducer is really similar with normal pressure sensor. The confined reaction chamber of membrane is very sensitive to normal direction force. For the bio molecular detection, we use a PDMS micro channel which attaches the reaction chamber of membrane transducer. When a bio medium liquids are flowed in the micro channel, the membrane transducer has fluidic pressure depending on Hagen-Poiseuille equation.[1]

$$\Delta P = \frac{8\mu LQ}{\pi r^4} \text{ or } \frac{128\mu LQ}{\pi d^4} \quad \text{Equation 4.2.1-1}$$

where ΔP is the pressure loss, L is the length of pipe, μ is the dynamic viscosity, Q is the volumetric flow rate, r is the radius and d is the diameter. The equation informs the pressure drop in a fluid flowing through a long cylindrical pipe. In the membrane transducer, the velocity of micro channel is measured from 0.1 $\mu\text{l}/\text{min}$ to 2000 $\mu\text{l}/\text{min}$, and the perpendicular pressure of membrane transducer is calculated with COMSOL 6.1 FEM simulation. Through the simulation, the vertical pressure on the membrane is 0.136 Pascal when the flow velocity of micro channel is 1 $\mu\text{l}/\text{min}$. Figure 4-2 show the capacitance change of membrane transducer when the flow velocity is increased at every one minute. When we consider the noise level of capacitance value at 1 $\mu\text{l}/\text{min}$, the transducer of 100 nm thickness membrane can detect 0.03 Pascal pressure. The value is 30 times sensitive than the most sensitive pressure sensor recorded until now.[2] Furthermore, the membrane transducer can measure 23 Pascal pressure with distinct signal depicted in figure 4-3. The membrane transducer has very large dynamic range like as over 10,000.

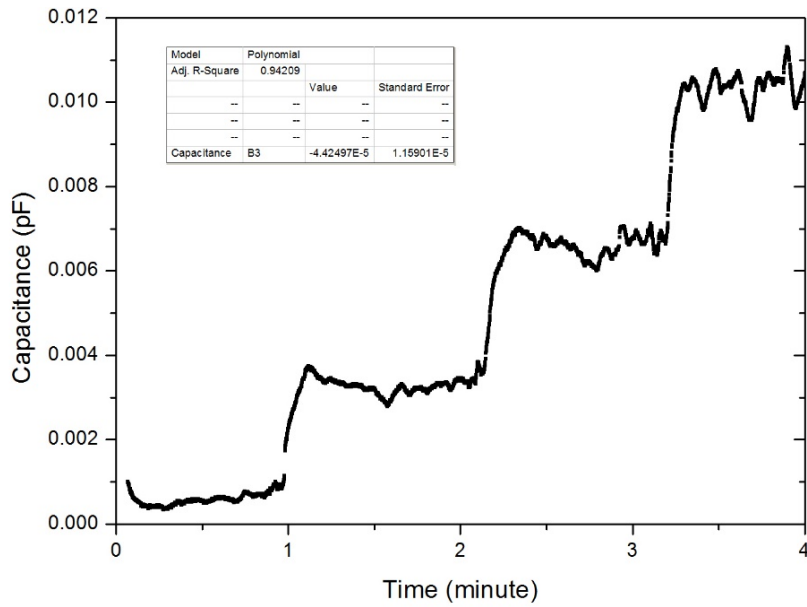


Figure 4-2. Pressure sensitivity of membrane transducer. This membrane transducer use 100nm thickness silicon nitride film.

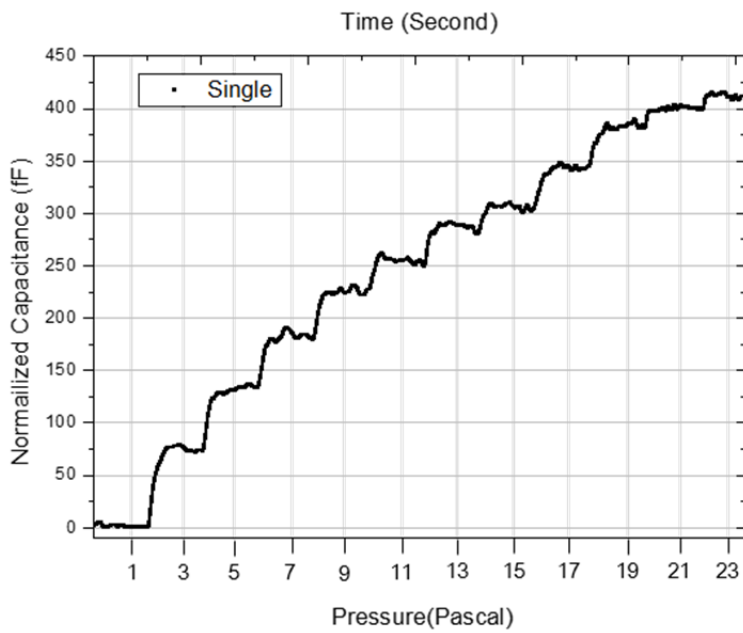


Figure 4-3. Pressure signal of thin membrane transducer single sensor signal from 1 to 23 Pascal.

4.2 Common Mode Rejection

One of the major challenges and priorities in sensor technology is reliability. Reliability, however, isn't necessarily a measurable single point; it's the result of a number of considerations, among them: the complexity of today's sensor systems and networks, sensor "consensus," required in sensor fusion, integration of diverse sensors and electronics into ever-smaller devices, the addition of advanced-degree sensor intelligence and the harsh and extreme environments into which sensors are placed.[3] On occasion, at least some sensor data is going to be imprecise or inconsistent. What is more, based on signal strength and transmission accuracy, another dimension of failure may be added: the possibility of not receiving the data at all, due to transmission failure. Sensor data is also susceptible to errors and interference such as noise. It is for all of these reasons that engineers must also be able to measure imprecision and true reliability for data that is gathered.

One of the key challenges of the membrane-based chemo-mechanical transduction is regarding how the external disturbances can be overcome. There are two major sources that contribute to the external disturbances: pressure and temperature. The overall configuration of the membrane-based technology results in the pressure sensor of high sensitivity. Moreover the use of sandwiched metal and other structural layers leads to a temperature-sensitive bimetallic effect. One of the previous approaches to address the temperature sensitivity is to use the metal layers of the exactly same shape and size.[4] Therefore, rather than removing the noise of

an individual sensor, it is more effective to kill the noise in an array of sensor via common mode rejection.

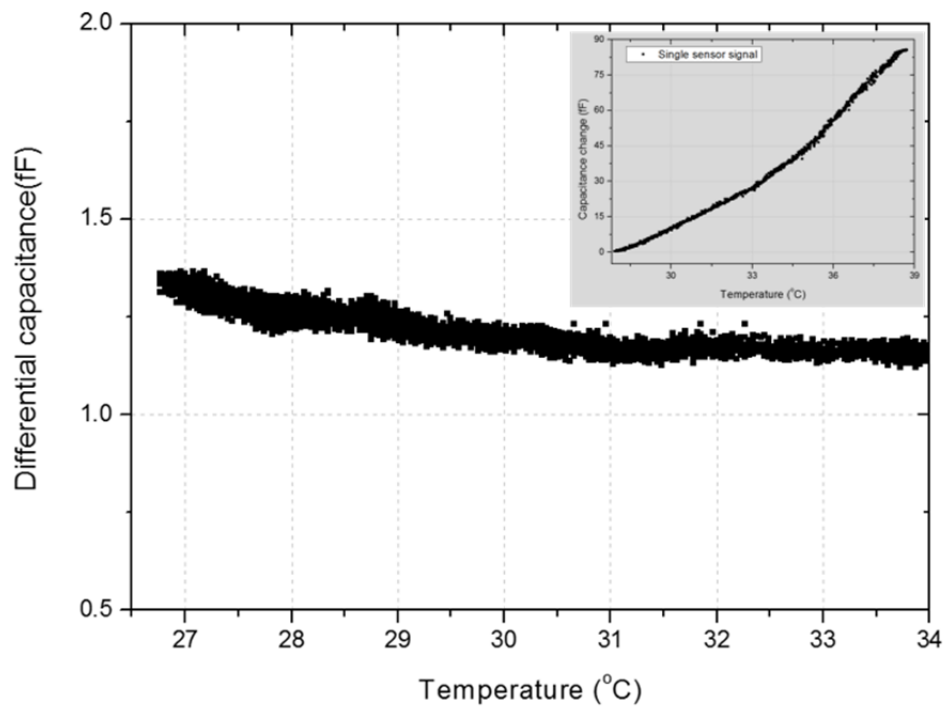


Figure 4-4. Temperature differential signal from 27 to 34 degree Celsius

Common mode rejection also helps find some specific signals. Figure 4-4 shows the response of the array sensor to the change of temperature from 27°C to 34°C, with the inset displaying result of the individual sensor. The array of sensor collectively reads a trial differential signal of less than 1fF, which is relatively lower than 9fF, read out by an individual sensor. Likewise, pressure noise experiment is performed on both sensor configurations which result is shown in Figure 4-5. The individual sensor displays a significant signal, of 400 fF compared to only 1 fF by the array sensor. These two experiments reveal the excellent

uniformity of the silicon nitride membrane transducer that allows differential mode measurement which leads to the detection of specific molecular interaction.

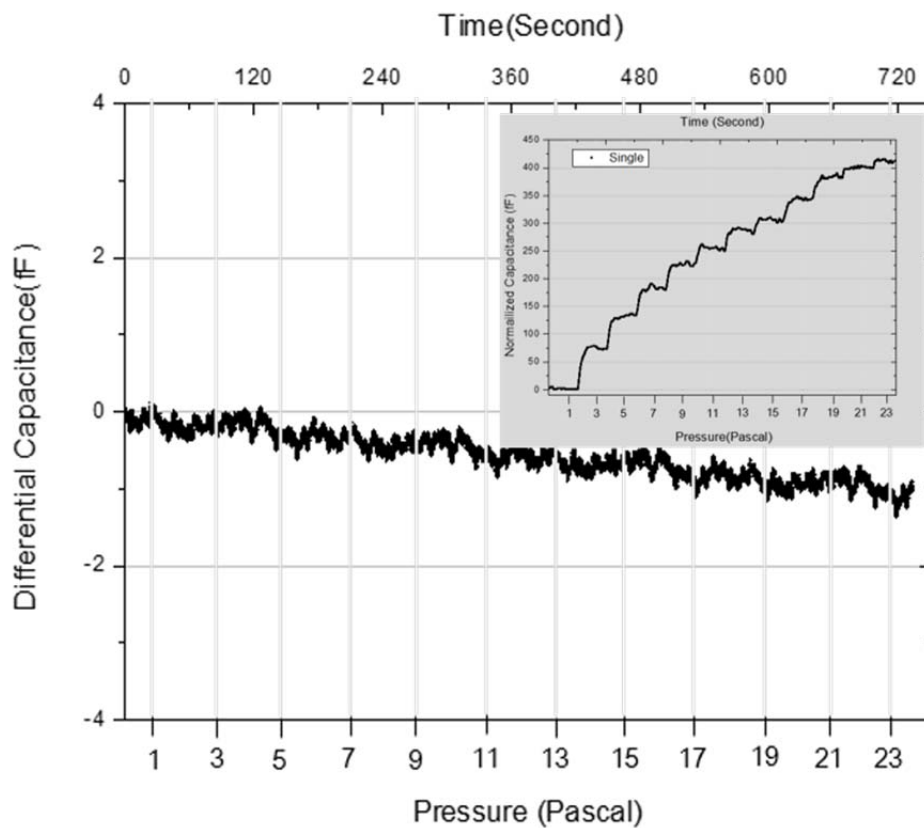


Figure 4-5. Pressure signal of thin membrane transducer. Differential signal from 1 to 23 Pascal.

Real-time monitoring of membrane deflection through the change of capacitance value is achievable. Figure 4-6(a) is the real time response of the sensor, showing decrease in capacitance with magnitude proportional to the amount of subjected hydraulic pressure when 10 μ l and 200 μ l deionized water is added in sequence. Abrupt thermal noise can be neutralized and filtered, as seen in Figure 4-6(b).

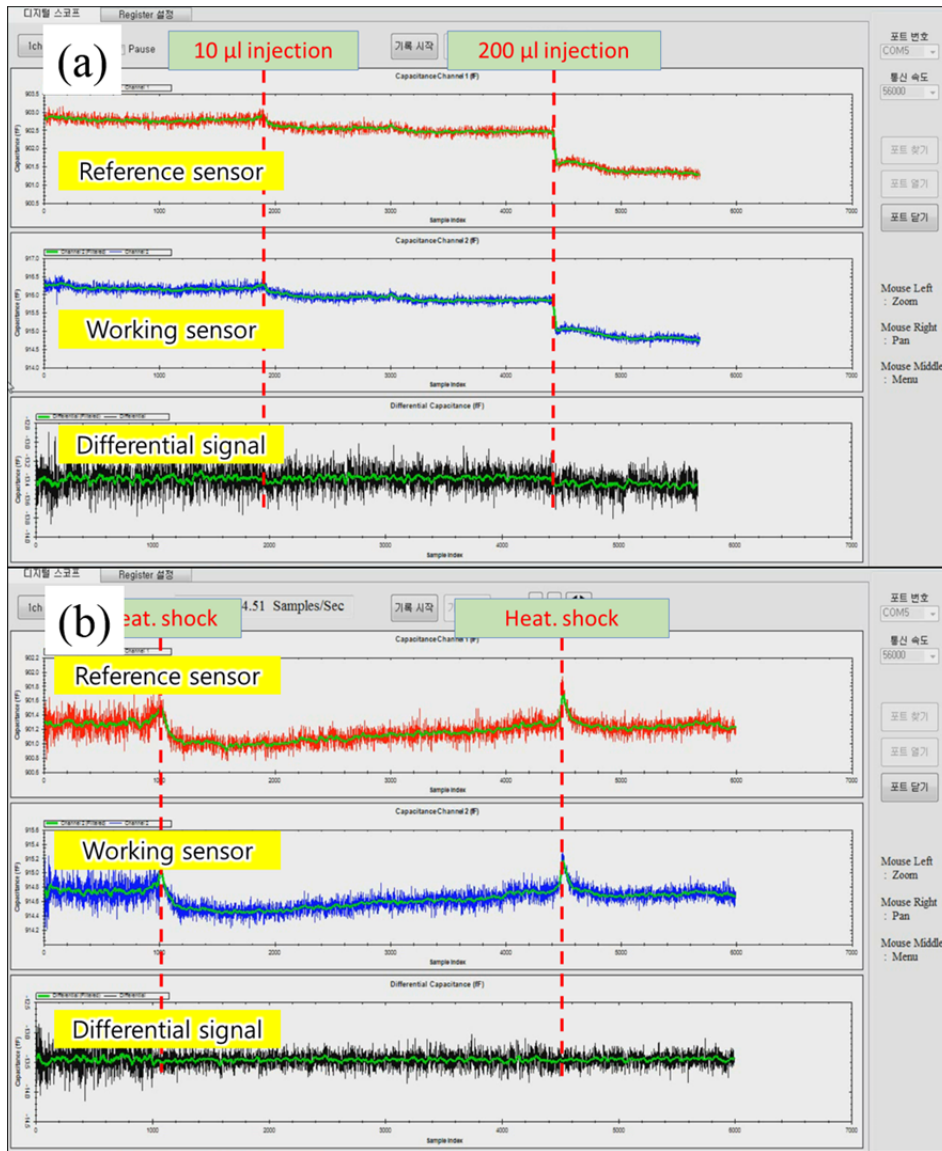


Figure 4-6. The common mode rejection of pressure(a) and temperature(b)

Even if chemical reaction takes place on the sensor, the identical signal produced will be eradicated and differential signal will remain neutral. This can be explained with the working principle of the commercialized cantilever. The upper schematics of a figure 4-7 show the structure of a cantilever on which negative charged glutathione protein molecules are immobilized. The glutathione is an antioxidant

that protects important cellular components from harms by reactive oxygen species such as free radicals and peroxides.[5] Its two carboxylic acid groups are exposed and the thiol group of the cysteine allows itself to be immobilized on gold-covered sensor surfaces. When charged molecules attracted onto cantilever surface, electrostatic repulsion generates surface stress that causes the bending of cantilever. The bottom graph of a figure 4-7 shows the bending response of the cantilever when 250 μl Tris buffer with various CaCl_2 concentrations is injected into the chamber where the cantilever is immersed by TE buffer (4 $\mu\text{l/s}$). The functionalization with negatively charged glutathione builds up an initial surface stress, which is then released with the introduction of positively charged Ca^{2+} ions. The average differential deflection of three cantilevers upon binding of divalent cations is completely reversible by removing Ca^{2+} with TE buffer containing EDTA.

By applying the same working principle, 11-MUA is densely coated on the reaction gold surface of the membrane transducer. 11-MUA has carboxylic acid and thiol groups that enable immobilization of the molecules on the gold surface. Reaction chamber is filled with 500 μl deionized water before the injection of 10 μl 1xPBS buffer containing 5mM CaCl_2 . The membrane budes up due to the release of compressive stress when the molecular repulsion is neutralized by the cations. Identical signals from both individual sensors can be filtered with the use of sensor array, as shown in figure 4-8. This is extremely crucial for the rejection of signals produced by non-specific adsorption without stringent washing process.

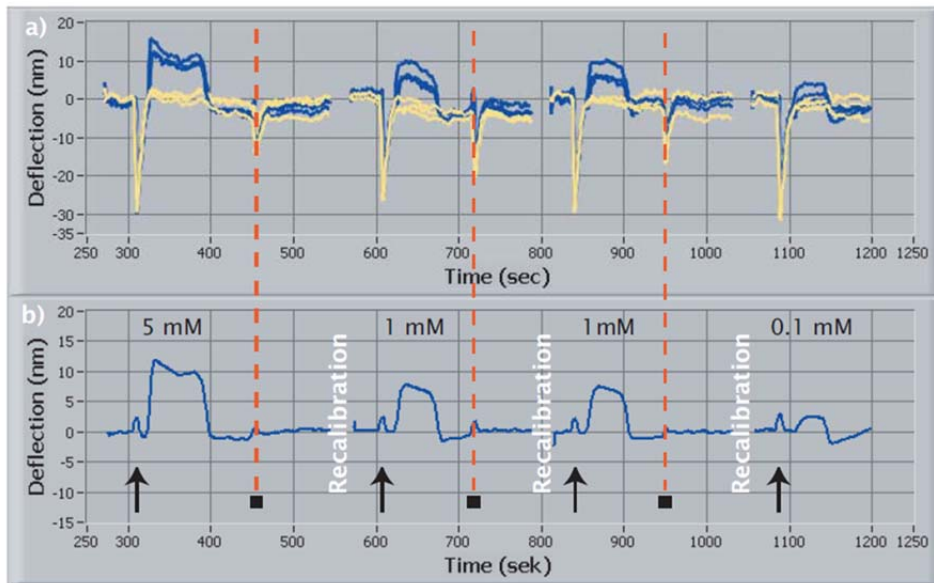
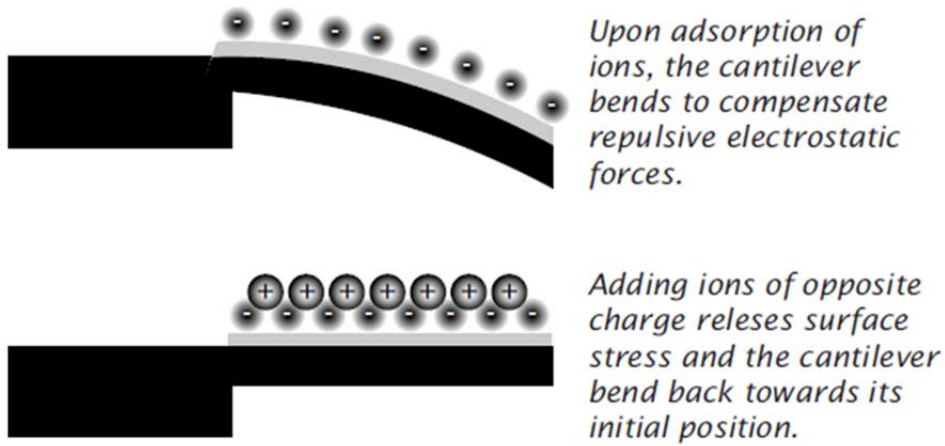


Figure 4-7. Detection of divalent cations with cantilever biosensors is based on the affinity of these ions to a variety of bio-molecules. (a) The mechanism of cantilever deflection is originated from electrostatic repulsion. (b) Cantilever arrays are deflected in constant buffer TE flow followed by injecting various concentration of CaCl_2 . [6]

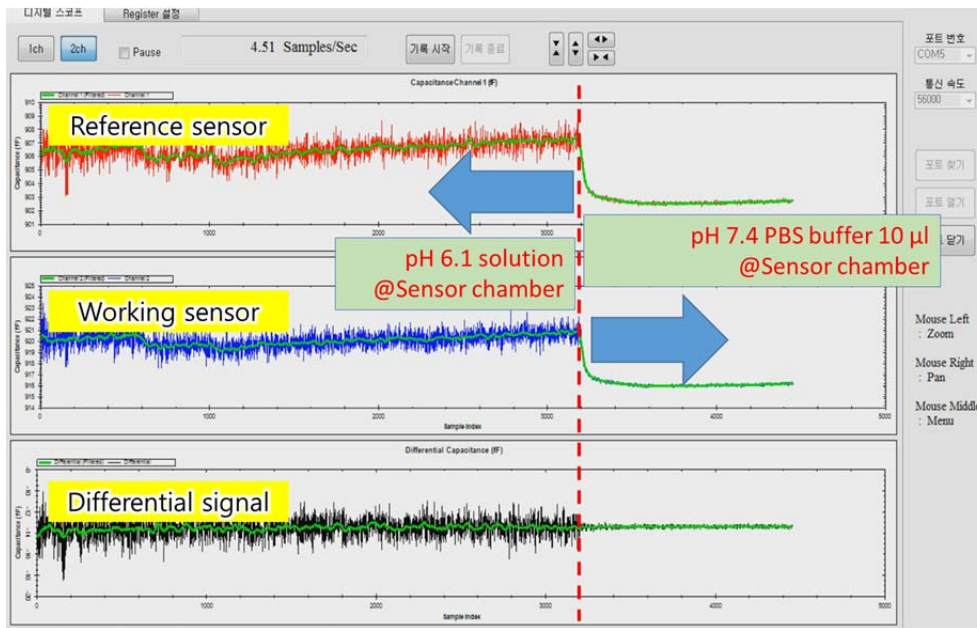


Figure 4-8. Chemical common mode rejection with non-specific adsorption.

4.3 Ion Detection with Membrane Transducer System

4.3.1 Chemo-Electrical Detection

Our membrane transducer has high aspect ratio structure with the area of $750\ \mu\text{m} \times 750\ \mu\text{m}$ and only $2\ \mu\text{m}$ electrode gap. The membrane structure uses the capacitance measurement, so some electric field penetrates silicon nitride membrane. A capacitive sensor has been developed for measuring the vertical deflection, but the electric fields distribute not only electrode sides facing each other but also the other sides explained in figure 4-9. Therefore, the membrane transducer can be affected by the charge of molecule and the change of liquid analyte environment.

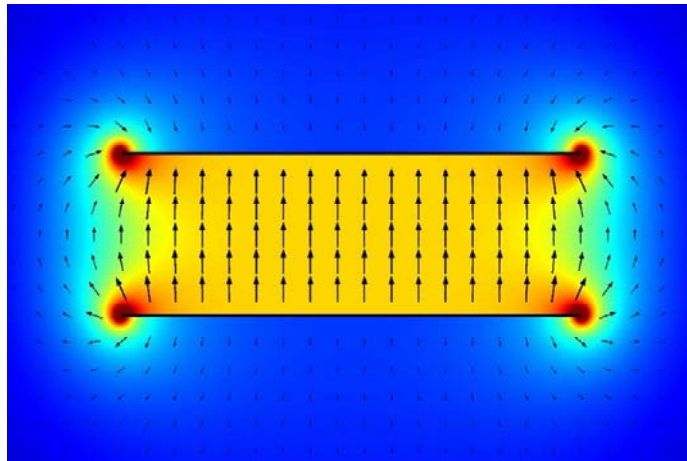


Figure 4-9. The electric field distribution of two oppositely charged metal plates. [7]

As showing figure 4-10, the membrane transducer has different size of electrodes. Lower electrode is much smaller than upper rigid electrode, so electric fields easily

travel more long distance than that of parallel electrodes with same size. Also, electric field penetrates dielectric materials such as silicon nitride, PDMS and parylene. Therefore, capacitance is affected by the properties of liquid in the reaction chamber such as dielectric constant, charge distribution and molecular density because electric field passes through silicon nitride membrane with the thickness of 500nm. We demonstrate the phenomena utilizing the membrane transducer system. First, ultra-pure water (Biosesang.inc, Reverse osmosis filtered and Autoclaved at 121°C and 151/sq in. 20min, ph. 5.6 and dielectric constant ~80) is filled into the chamber without reaction gold while membrane transducer capacitance is measured by the capacitance measurement system. There is some drift in the capacitance signal of the membrane transducer due to temperature variation and hydraulic pressure.

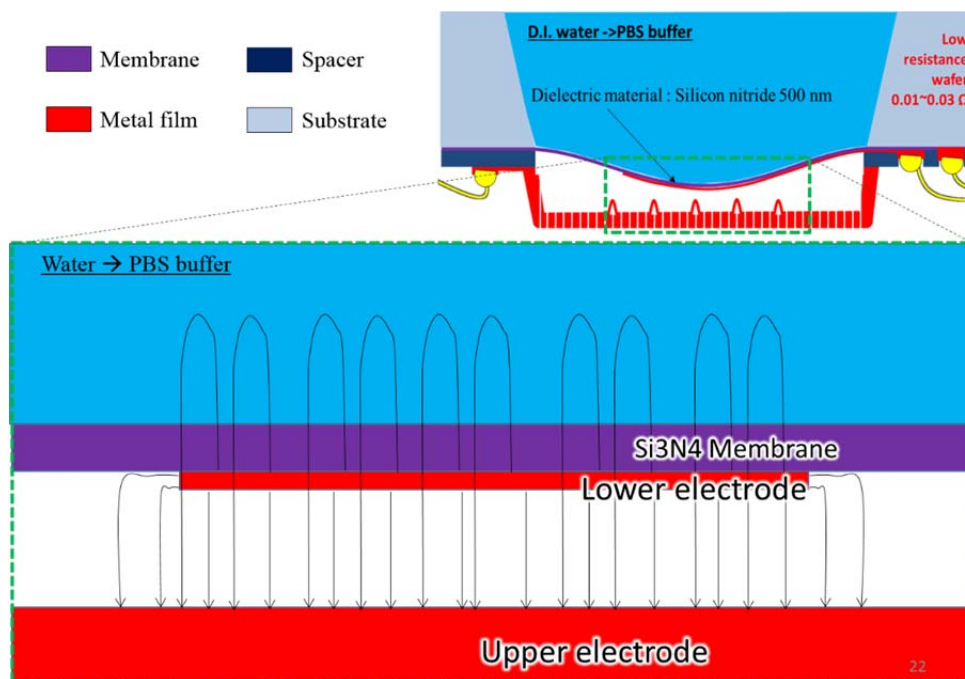


Figure 4-10. Chemo-electrical measurement.

We wait until the signal enters steady state and then put 1x PBS buffer with the volume of just 5 μ l (ph. 7.4, relative dielectric constant \sim 76 [8]) into the reaction chamber. Ingredient of 1x PBS buffer is normally NaCl 137 mM, KCl 2.7 mM, Na₂HPO₄•2H₂O 10mM and KH₂PO₄ 2mM. The buffer drop the corner of 16 array membrane transducer, the buffer is diffused into ultra-pure water according to Fick's laws. The capacitance value of the sensors which are near the position where the buffer solution is dropped changes a lot and faster the others such as 1 ~ 4 in figure 4-11. That is because that the buffer concentration is lower as it diffuses from the drop point and the diffusion speed also decreases. Therefore, the capacitance measurement can detect analyte solution variation. The capacitance change from the variation is significant which is about 230fF.

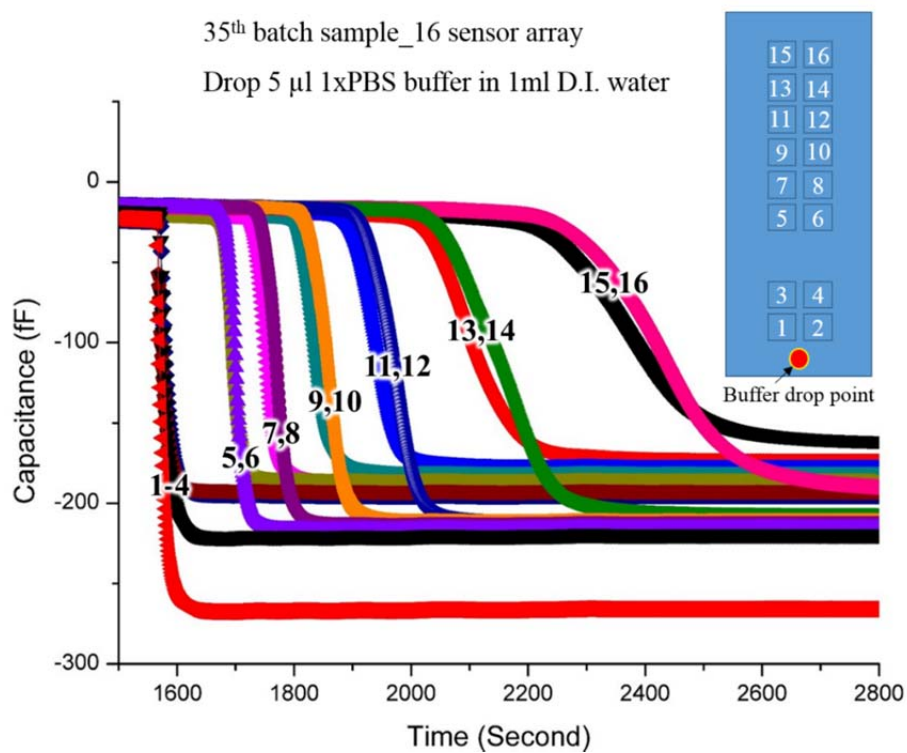


Figure 4-11. The signal of chemo-electrical transducer

4.3.2 Chemo-Mechanical Design

In the membrane chemomechanical transducer system, we cover the gold metal layer on the whole membrane to protect chemo-electrical signal and the gold layer is connected to the ground on capacitance measurement circuit. In this case, the electric field of capacitance is theoretically shielded, which is described in figure 4-12.

We also confirm the phenomena by using the membrane transducer system. The experimental protocol is same with above experiments. However, there is no signal changes when the grounded gold metal layer shields electrical field and keeps the field penetrating the liquid in the reaction chamber in the capacitance measurement system even after the PBS buffer drops in a pure water shown in figure 4-13.

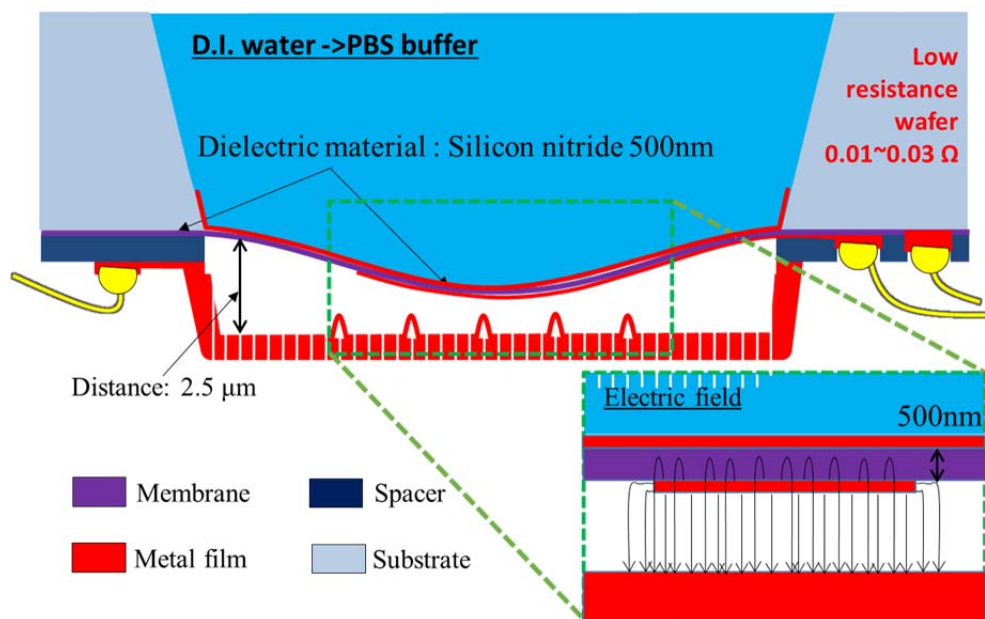


Figure 4-12. Schematics of electric field shielding by depositing metal layer.

Also, the metal shielded membrane transducer shows very small capacitance noise of individual membrane transducers in steady state. In addition, the capacitance signal is not affected even after 5 μl of 1x PBS is added more. Differential signal noise level between 8 samples on the left and the other 8 ones on the left is under 100 aF.

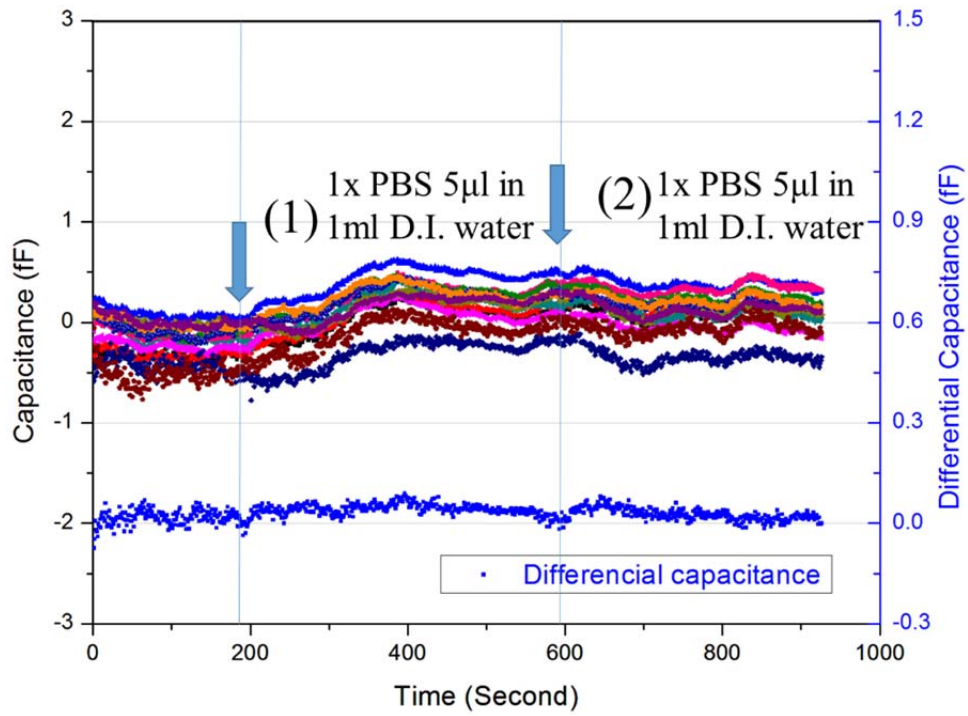


Figure 4-13. Experimental result of electric field shielding with metal layer.

4.3.3 Cation Detection

11-MUA is immobilized on the reaction gold of the grounded metal shield membrane transducer. The 11-MUA (Sigma-Aldrich cop. #450561) has one carboxylic acid group and thiol group which reacts with the reaction gold on the membrane surface. When ultra-pure deionized water of 500 μl is filled into the reaction chamber on the membrane transducer, carboxylate ion (RCOO^-) makes the membrane deflected downside because its negative charge generates the compressive stress of the membrane surface as shown in figure 4-14. However, after 10 μl 1xPBS buffer which has the abundance of cations is injected into the chamber, the carboxylate ion on the membrane absorbs the counter-ions. The adsorptions reduce the electrostatic repulsion in the monolayer and decrease the bending of the membrane. However, this phenomena cannot be analyzed with a simple electrostatic repulsion in the monolayer because the population of charged surface groups are constantly kept[9]. .

Figure 4-15 shows the results. The capacitance value drops as we expected and noise signal also dramatically decreases. This distinct noise is from the auto-ionization of water [10]. The auto-ionization phenomenon is to lose the nucleus of one of its hydrogen atoms and it becomes a hydroxide ion, OH^- , and the hydroxide ion makes hydrogen nucleus, H^+ and finally H^+ does association and dissociation with negative charge carboxylate ion. On the other hands, the noise is stable after the ion bonding between cations and carboxylate ions on top of the surface. In conclusion, energy of chemical reaction is transduced into mechanical deformation of membrane.

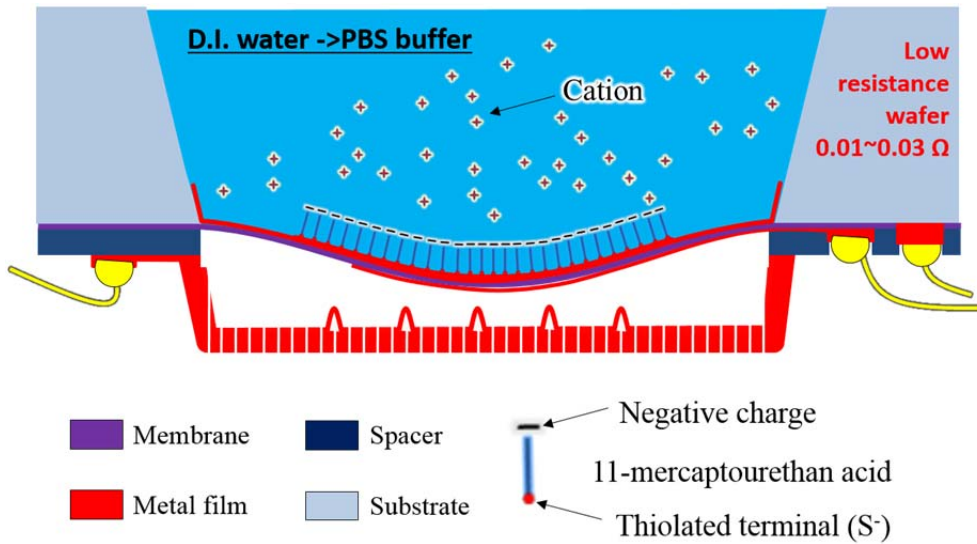


Figure 4-14. Negative charge molecule immobilization at the deposited reaction gold on the backside of membrane.

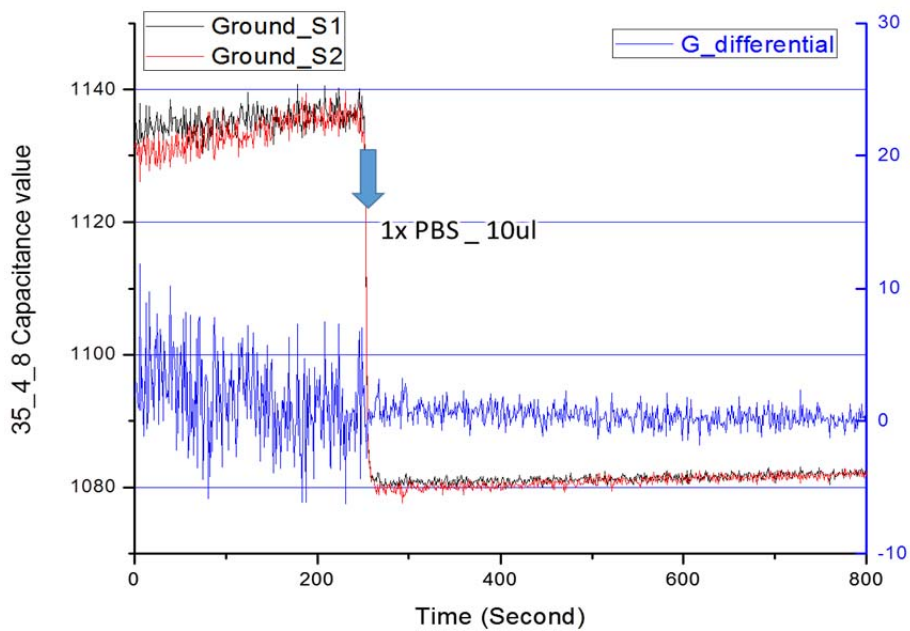


Figure 4-15. Negative electrostatic forces are released by adding cation charge on the buffer.

4.4 Molecular Recognition with Aptamer Receptor

The quantitative and qualitative detection of specific target molecule need high quality transducers, receptor structure and sensitive measurement system. In this work, the membrane transducer of 33th batch sample show the high quality detection results of thrombin protein. The 32 ~ 33th batches utilize a highly controlled material such as low stress silicon nitride, high density nickel structure and the reaction gold of large grain size. In the membrane transducer of 32th batch sample, the specific recognition of thrombin protein is confirmed, so I made 52 number chips at the 33th batch and the 37 chips of them were selected to detect thrombin protein with identical performance of capacitive value. Subsequently, the special receptor structures of thrombin aptamer were designed with the reference of SPR measurement protocol and the recipe was applied in the experiment of thrombin detection. However, the non-specific signal of bovine serum albumin (BSA) was also detected on the both transducers of sensing and reference. 2-aminoethanol and 2-mercaptoethanol were blocked to reject the extra functional groups of linker molecules such as carboxylic acid and maleimide after 19 sample experiments. After the blocking, the capacitance change of thrombin protein interacted with thrombin binding aptamer is reduced, but the differential capacitance value of BSA was eliminated with common mode rejection of reference transducer. The modified receptor protocol was confirmed with fluorescence measurement by using gold pattern slide and our membrane transducer. And then the rest of 18 number of membrane transducers were examined to detect the different concentration of thrombin protein with duplicated receptor structures.

4.4.1 Thrombin Protein and Thrombin Binding Aptamer

Thrombin is a serine protease that in humans is encoded by the *F2* gene. Prothrombin which is coagulation factor II, is proteolytically cleaved to form thrombin in the coagulation cascade, which ultimately results in the reduction of blood loss. Thrombin in turn acts as a serine protease that converts soluble fibrinogen into insoluble strands of fibrin, as well as catalysing many other coagulation-related reactions[11]. Since thrombin is a key protein in the regulation of thrombosis and haemostasis, the aptamer that recognizes thrombin has been extensively investigated. Aptamers are synthesized oligonucleotides (DNA or RNA) that can form tertiary structures that recognize and bind to their respective targets with high specificity and affinity equal or often superior to those of antibodies. Furthermore, thrombin plays a central role in a number of cardiovascular diseases[12], and is thought to regulate many processes in inflammation and tissue repair at the vessel wall[13]. The DNA aptamer against thrombin is the first one selected in vitro, specific for a protein without nucleic acids-binding properties, and has been studied as an ant clotting therapeutic tool. When bound to thrombin, the aptamer exists primarily in its quadruplex form described in figure 4-17, while in a solution free of the target protein, especially in the solution with low ionic strength, it adopts a more relaxed random coil conformation[14]. We assume that the immobilized aptamer is in a conformational equilibrium between its unfolded state and the folded, binding-competent G-quartet conformation[15]. Since thrombin binds only with the G-quartet conformation, the target protein drives the equilibrium towards this state. We used the following thrombin binding buffer (TBB) condition for the reaction of thrombin to the aptamer: 20 mM Tris-acetate

pH 7.4, 140 mM NaCl, 5 mM KCl, 1 mM CaCl₂, 1 mM MgCl₂ to stable G-quartet conformation.

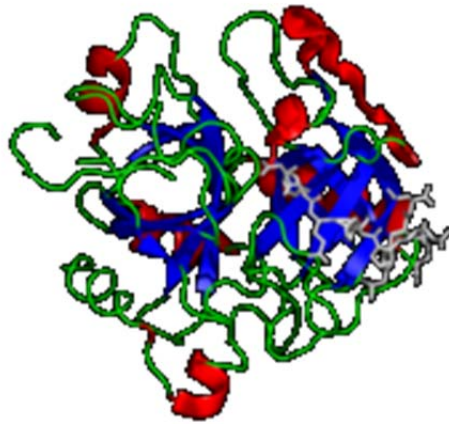


Figure 4-16. Thrombin protein which is coagulation factor II. The structure of human thrombin in complex with the inhibitor hirudin. [11]

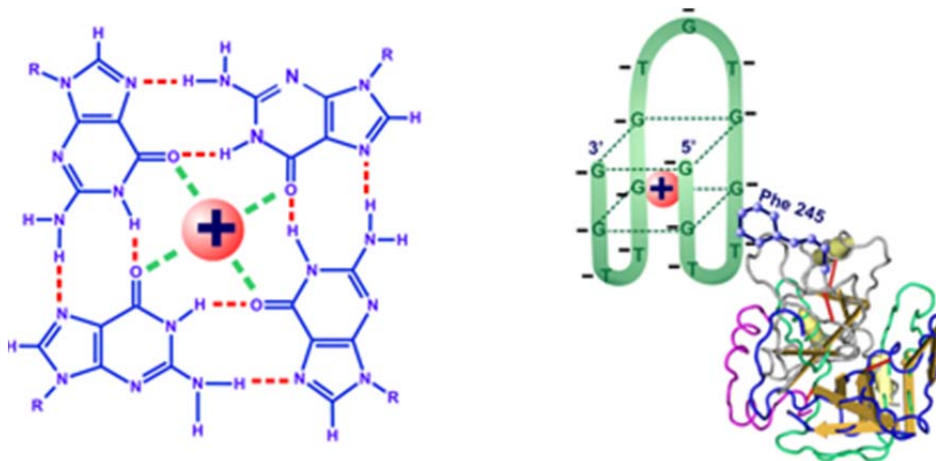


Figure 4- 17. G-tetrad structures in the presence of K and Na cation, and thrombin binding aptamer (TBA)[16].

4.4.2 Immobilization of Thrombin Binding Aptamer

Nanomechanical receptor structures have to be controlled to overcome the limitations imposed by non-specific binding and increase target capture specificity. The high specificity and affinity of aptamer make it possible to achieve higher detection sensitivity and selectivity. Therefore, aptamer-based bioassays can adopt special assay configurations to enhance the chemo-mechanical transduction of bio-recognition events. Special assay for stable and sensitive receptor structure is developed to adapt for our membrane-based transducer system by using optical measurements. For the dense self-assembled monolayer SAM formation, the completely fabricated membrane sensor wafers are immersed over 12 hours in ethanol based 5 mM concentration 11-mercaptopropionic acid (MUA), right after MEMS process to protect the contamination of gold surface during chip package which reduce the effect of ion charge variation on exposure gold surface due to defect of SAM and prohibit non-specific molecular adsorption[17-19]. Also, the dense SAM prevents the surface stress due to adsorption of ion charge on the defect sites which include Au binding sites unoccupied with SAM. Before packaging with the PCB circuit, the SAM is thoroughly washed with 100% ethanol to create a monolayer of 11-MUA. When the sensor has been packaged, a brief cleaning-cum-stabilization with a 100 mM MES buffer is initiated for 5 minutes. The next step is in-situ activation of SAM by immobilizing NHS-EDC reagent (1:1 aqueous solution of 100 mM NHS and 400 mM EDC) followed by immobilization of 11MUA-amine modified maleimide conjugate, which promote the orientation and flexibility of receptor to binding site of target protein.

Also, the unbound reactive ester groups are deactivated by a 1 M aqueous ethanolamine solution (pH 8) over the sensor surface to prevent non-specific binding. Finally, 100 μ M thiol-modified thrombin binding aptamers (TBA; HTQ) are covalently bound to the maleimide with the low density of receptor to increase the efficiency of interaction with thrombin protein. Density is controlled by mixing 10 % volume ratio of 1mM 6-mercaptoethanol to the HTQ aptamers. Once the sensor surface is covered with anchored TBA receptor, the analytic thrombin is injected over the sensor surface. The HTQ receptor- thrombin analyst interaction is studied with different concentrations of analyte.

Table 9 shows the detail bio assay protocol to form thrombin binding aptamer. There are information for reaction such as buffer pH, reaction time, types of analytes, the amount and the concentration of analytes. Fluorescence dye (Cy-3) modified-TBA is immobilized gold patch to check the protocol. The eight gold patches are patterned on a slide glass with circle shape and the receptor molecules are immobilized on the slide glass by using the developed assay protocol with different base buffer shown as figure 4-18(a). On the figure, there are also two control experiments which are written with “No-MUA, DTT”. At the control patch, 11-MUA alkanethiol is not immobilized to confirm non-specific adsorption of 4-aminopenyle maleimide and TBA probe. We observe the strongest fluorescence signal in the case that 10X PBS is used as base buffer. However, not strong signal is showed when 5X TBE and 25X TAE which is not optimized for maleimide and thiol reaction (require pH 6.8 ~7.5). Cy-3 modified TBA immobilization is also check with Tris-HCl buffer that is good for the reaction on reaction gold on the membrane, which is shown as figure 4-18(b). There are some non-specific

adsorptions on the edge of membrane, but TBA probes are not immobilized on the silicon nitride membrane without gold patch.

Table 9. Assay protocol of thrombin binding aptamer.

Thiol linked DNA immobilization on thiol linked maleimide modified gold surface								
Seq.	Protocol	BASE Buffer	Concent.	time	stable time	revision	Total step time (min)	etc.
1	Active gold deposition							
2	immediatly, pour 11-MUA on gold	99% Ethanol	1mM	1440		1	1440	Protect contamination of gold
3	take out 11-MUA & ethanol cleaning	99% Ethanol		10		2	20	make monolayer of 11-MUA
4	Dry			30		1	30	
5	chip package(UV-treatment)			5		1	5	UV glue curing-Wall type
6	chip package(soldering)			5		1	5	consider thermal damage
7	pour 11-MUA	99% Ethanol	1mM	120		1	120	activate carboxyl terminal
8	take out 11-MUA & ethanol cleaning	99% Ethanol		10		1	10	
9	take out ethanol & MES cleaning	0.1M MES		10		2	20	
10	Pour 0.1 M MES buffer and add EDC (10ul)	0.1M MES	51.16mM	5	5	1	10	EDC Conc. 8mg/ml
11	Add NHS (10 ul) in above solution	0.1M MES		25		1	25	NHS conc. 12mg/ml
12	Change buffer MES(pH 6.1)->1XPBS(7.4)			10		3	30	
13	Add 10 ul, 4-amino phenyl maleimide	1X PBS(7.4)	500uM	180	10	1	190	
14	Washing with Tris-HCl(7.4)	0.5M Tris-HCl		10		3	30	
15	Prepare and immediate use thiol modified ssDNA	0.5M Tris-HCl	100uM	300	10	1	310	DTT treated ssDNA aptamer 20ul
16	Add 50 ul, 6-MCH	0.5M Tris-HCl	1mM	120	10	1	130	
17	Wash with Tris-HCl buffer(50mM)	50mM Tris-HCl		10		3	30	
18	BSA 5ul injection in 500ul buffer	50mM Tris-HCl	100uM	150	20	1	170	
19	Wash with Tris-HCl buffer(50mM)	50mM Tris-HCl		10		3	30	
20	Thrombin 5ul injection in 500ul buffer	50mM Tris-HCl	100uM	150	20	1	170	
	Total						1275	total process time after package chip (120min=20hr)

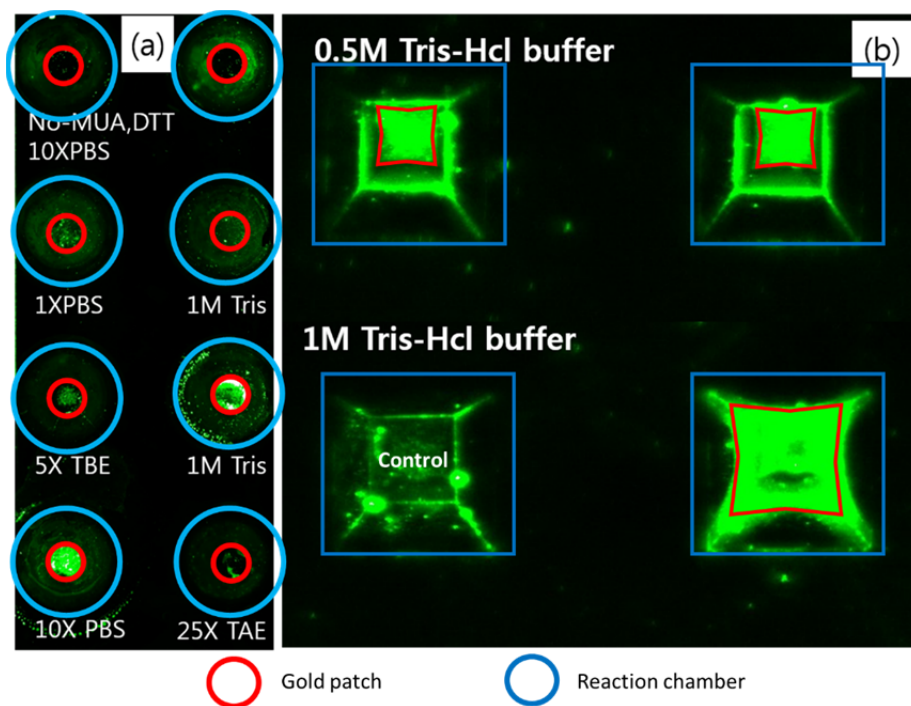


Figure 4-18. Confirm the molecular immobilization with laser scanning for fluorescence dye.

Figure 4-19 is the schematic of the molecular structure formed by the protocol. Thiol terminal on the 11-MUA is react with Au (111) and carboxylic terminal on another side of 11-MUA bind the amine terminal of maleimide. Also, maleimide and the thiol of TBA are bond together. Finally, extra functional groups of carboxylic terminal and maleimide are blocked respectively with 2-aminoethanol and 2-mercaptoethnol to reject the signal from non-specific adsorption of protein.

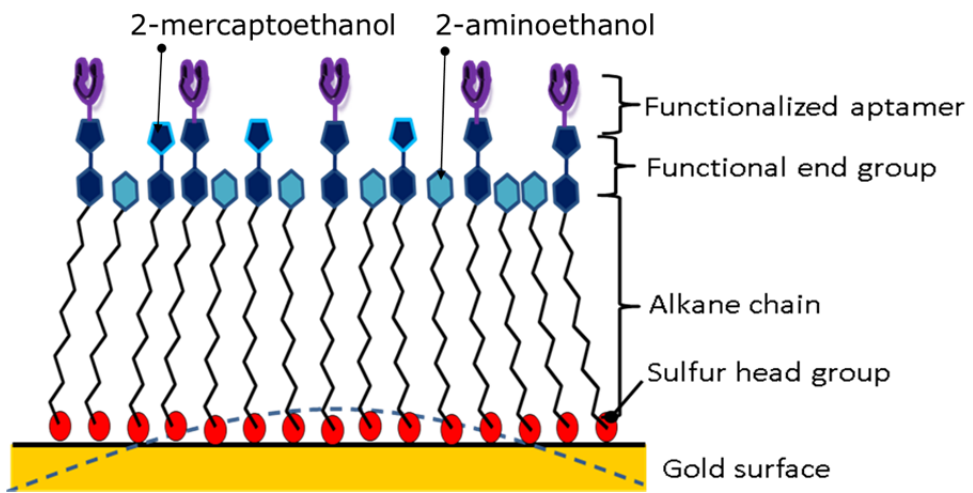


Figure 4-19. Highly stable thrombin protein probe structure

4.4.3 Thrombin Protein Detection and FE Simulation

The designed receptor structure is adapted in membrane-based chemomechanical transducer system. For the chemo-mechanical transduction, the reaction chamber is contained in thrombin binding buffer of 500 μl before injecting thrombin protein to stabilize the signal from both transducer depicted in figure 4-20. We just inject the 10 μl drop of thrombin binding buffer, spiked with the amount concentration of thrombin protein, into the reaction chamber on top of the membrane transducer without external pump system. There are two array membrane transducers to reject common noise with reference sensor. The reference sensor is immobilized with similar structure of probe molecule which replaces 2-mercaptoethanol with thrombin binding aptamer.

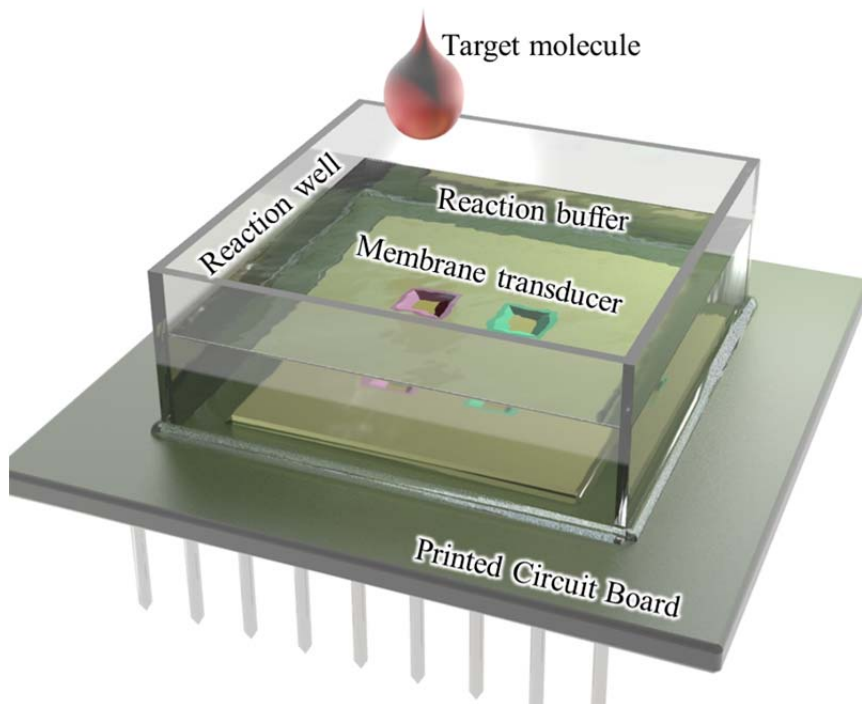


Figure 4-20. Experimental set up for bio molecular interaction.

When we inject the thrombin protein of 10 μ l drop with 5 μ M concentration at the reaction chamber and the final concentration is diluted with 100 nM. In the figure 4-21, the capacitance value of reference transducer is moved to the Y-axis of \sim 35 fF from the original data shown in appendix A. The differential value of capacitance indicates the specific molecular interaction between TBA and thrombin protein. Thrombin protein is diffused without external force to mix the solution injected at 20min. Therefore, the capacitance value of both of sensor and reference transducer are slowly increased with about 16 fF due to non-specific adsorption, but the distinct signal from the sensor transducer is higher changed with about 12 fF because of specific molecular interaction.

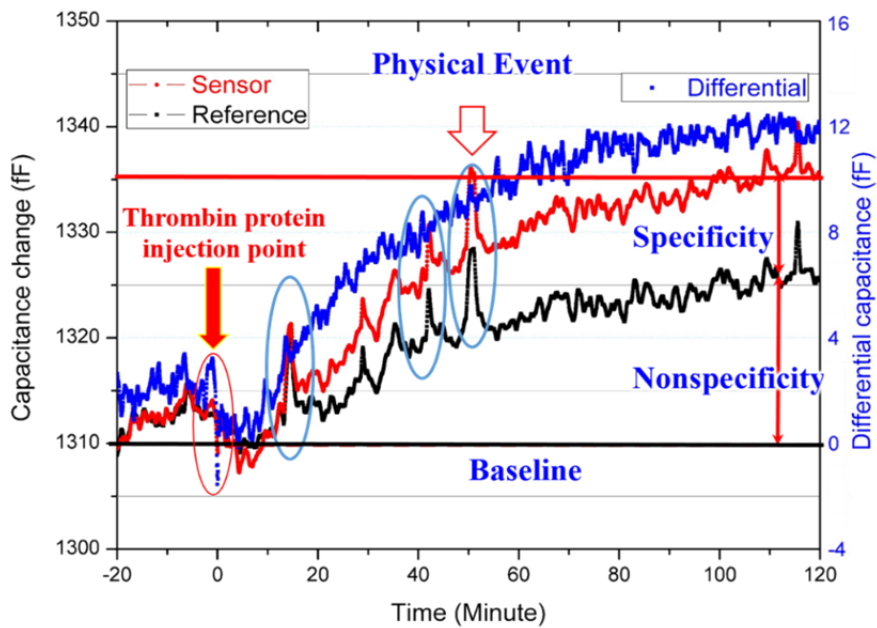


Figure 4-21. Specific molecular interaction result with array of membrane transducer to reject common noise.

The thrombin binding aptamer recognize thrombin proteins and the reaction induce the increase of intermolecular repulsion force which cause the compressive stress on the membrane. The compressive surface stresses normally bulge up the membrane, so the distance between electrodes increases, which lowers the capacitance. However, the membrane of our membrane transducer is deflected downside and the capacitance rises. That is because 500 μl base buffer already generates significant deflection due to its hydraulic pressure before the injection of thrombin protein into the reaction chamber. The deflection from the hydraulic pressure affects body elongation rather than residual stress release according to the plate theory of large deflection region in terms of surface stress.

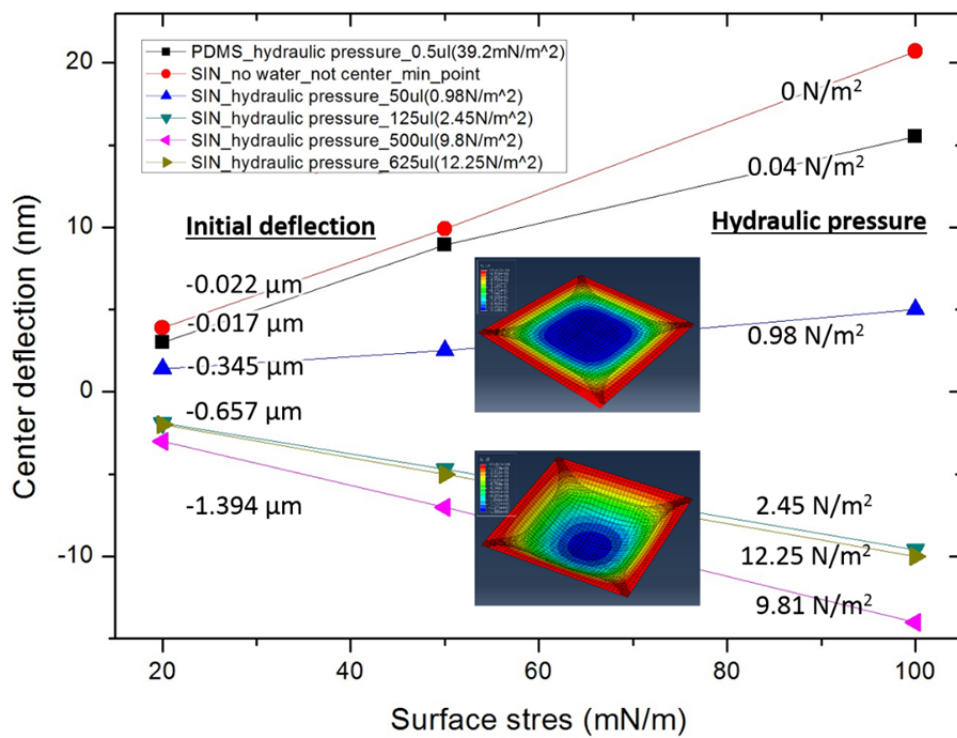


Figure 4-22. The center deflection verse surface stress. The direction of membrane deflection is decided with hydraulic pressures that cause the large deformation.

The compressive surface stresses (20, 50 and 100 mN/m) apply the membrane surface of the curved membrane due to hydraulic pressure to verify the experiment of thrombin protein described in figure 4-22. In our thrombin experiment, the compressive stress from the thrombin protein-aptamer interaction deflects down the membrane which is similar with FE simulation due to large deflection according to hydraulic pressure. According to the amount of perpendicular forces, a plate theory is decided with either small deflection or large deflection. When the amount of membrane deflection is in a small deflection range, compressive surface stress release the tensile stress of membrane due to hydraulic pressure. On the other hands, when the deflection is in the large deflection range, compressive surface stress stretches the membrane body.

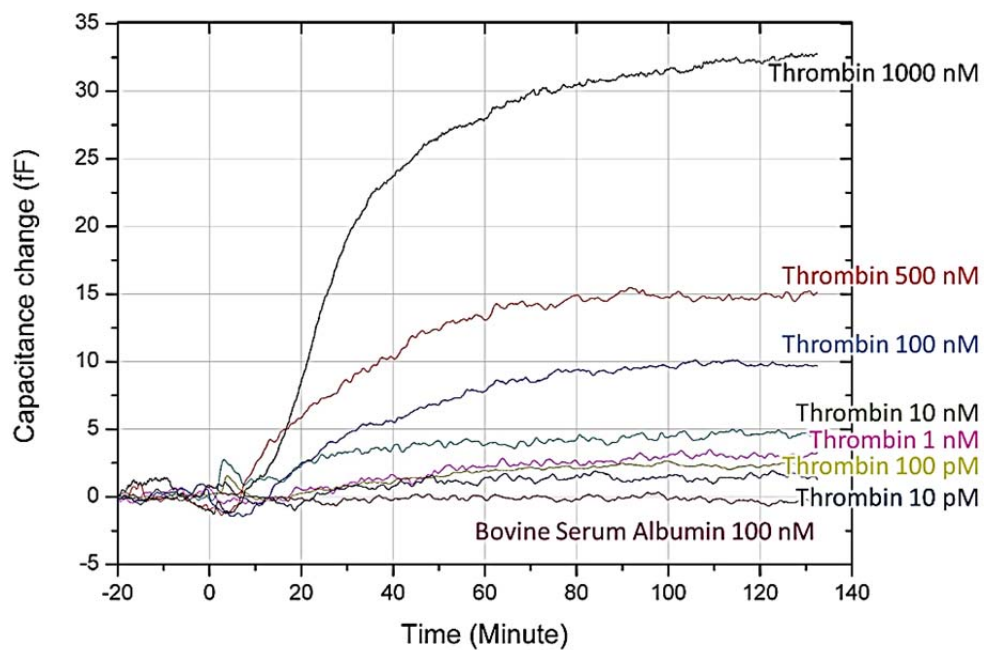


Figure 4-23. Qualitative, Quantitative molecular information result with membrane-based chemomechanical transducer system.

Variation of the concentration of thrombin protein is spiked into 10 μl of base buffer. Limit of detection sensitivity is 10 pM (0.37 ng/ml) like figure 4-23 and the data in the graph are filtered with the low pass filter (Cut-off: 0.1 Hz) of Butterworth IIR type described in appendix A. The center deflection of membrane according to the thrombin protein interaction of 500 nM is 24 nm calculated with integrating the differential area element of capacitance change with 15 fF explained in appendix B.

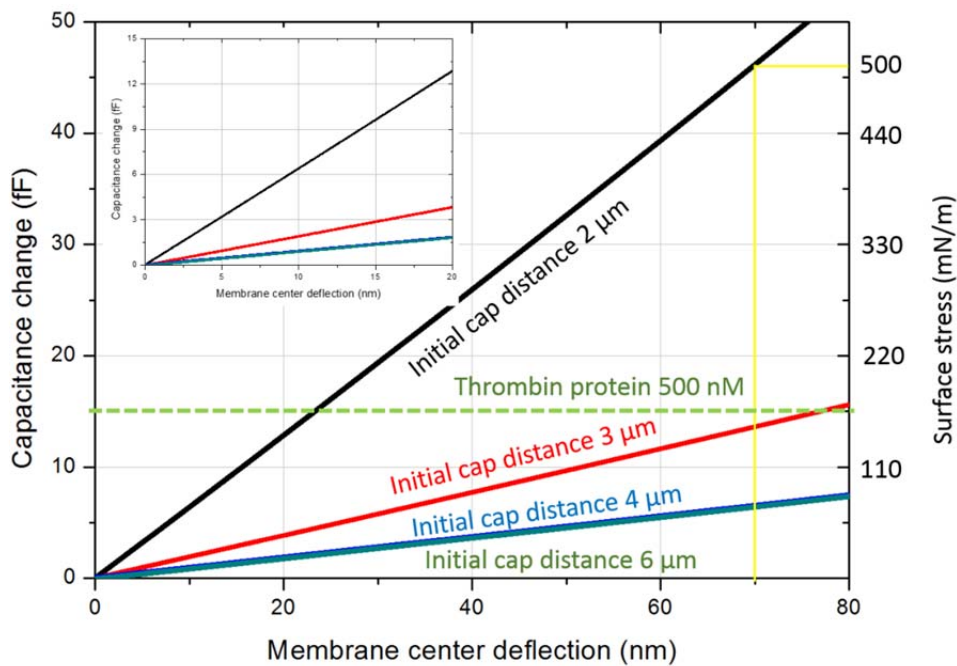


Figure 4-24. Capacitance calculation according to membrane deflection

The distance of electrodes depending on the thickness of sacrificial layer is 2 μm which have to be subtracted with the deflection of 1.3 μm due to hydraulic pressure. According to the FE simulation shown figure 4-24, the amount of deflection is correspond to the compressive surface stress of 165 mN/m. Therefore, the surface stress of 165 mN/m is quite larger than that of aptamer interaction with 500 nM

thrombin protein that might be involved with other incomprehensible effects because the surface stress of 51mN/m is calculated with the signal of aptamer-based cantilever sensor at the cocaine detection of 500 μ M [20]. Therefore, extra experiments are required to confirm the other effects.

4.5 Reference

1. <http://en.wikipedia.org/wiki/Hagen-Poiseuille>. *Hagen-Poiseuille equation*. [cited 2013 Nov. 18th].
2. Liu, X., et al., *A highly sensitive pressure sensor using a Au-patterned polydimethylsiloxane membrane for biosensing applications*. *Journal of Micromechanics and Microengineering*, 2013. **23**(2): p. 025022.
3. Mathas, C. *Sensor Reliability: Challenges and Improvements*. 2012 [cited 2013 Nov. 18th].
4. Arun Majumdar, S.-H.L., *Compensated Membrane Capacitive Bio-Chemical Sensor*, in *United States Patent*. 2010, THE REGENTS OF THE UNIVERSITY OF CALIFORNIA, Oakland, CA: United States.
5. www.wikipedia.org. *Glutathione*. [cited 2013.
6. concentris.ch, w., *Cantilever Sensor Detection of Divalent Cations*. 2013.
7. Nagel, J.R. *The Beauty of Electromagnetics The Parallel Plate Capacitor* 2013.
8. Yoon, G., *Dielectric Properties of Body Fluids with Various Hematocrit Levels*. *World Academy of Science, Engineering and Technology*, 2011. **60**: p. 1645 - 1649.
9. J. Fritz, M.K.B., H. P. Lang, T. Strunz, E. Meyer, H.-J. Gu" ntherodt, E. Delamarche, Ch. Gerber, and J. K. Gimzewski, *Stress at the Solid-Liquid Interface of Self-Assembled Monolayers on Gold Investigated with a Nanomechanical Sensor*. *Langmuir*, 2000. **16**: p. 9694-9696.
10. http://en.wikipedia.org/wiki/Self-ionization_of_water. *Self-ionization of water*.
11. <http://en.wikipedia.org/wiki/Thrombin>. *Thrombin*.
12. Holland, C.A., et al., *Effect of oligodeoxynucleotide thrombin aptamer on thrombin inhibition by heparin cofactor II and antithrombin*. *FEBS Lett*, 2000. **484**(2): p. 87-91.
13. Inuyama, H., et al., *Factor X-dependent, thrombin-generating activities on a neuroblastoma cell and their disappearance upon differentiation*. *Journal of Cellular*

Physiology, 1997. **173**(3): p. 406-414.

14. Baldrich, E., A. Restrepo, and C.K. O'Sullivan, *Aptasensor development: elucidation of critical parameters for optimal aptamer performance*. Anal Chem, 2004. **76**(23): p. 7053-63.

15. Zhang, H., et al., *Ultrasensitive Detection of Proteins by Amplification of Affinity Aptamers*. Angewandte Chemie International Edition, 2006. **45**(10): p. 1576-1580.

16. Schon, P., et al., *Charge propagation in "ion channel sensors" based on protein-modified electrodes and redox marker ions*. J Am Chem Soc, 2005. **127**(32): p. 11486-96.

17. Balamurugan, S., et al., *Effect of linker structure on surface density of aptamer monolayers and their corresponding protein binding efficiency*. Anal Chem, 2008. **80**(24): p. 9630-4.

18. White, R.J., et al., *Optimization of electrochemical aptamer-based sensors via optimization of probe packing density and surface chemistry*. Langmuir, 2008. **24**(18): p. 10513-8.

19. Godin, M., et al., *Cantilever-based sensing: the origin of surface stress and optimization strategies*. Nanotechnology, 2010. **21**(7): p. 075501.

20. Kang, K., et al., *Aptamer functionalized microcantilever sensors for cocaine detection*. Langmuir, 2011. **27**(23): p. 14696-702.

Chapter 5. Conclusion and Outlook

5.1 Conclusion

5.2 Future Work

5.2.1 Sensitivity Enhancement with Gold Nano Rod

5.2.2 Sensitivity Compensation for Quantitative Detection

Chapter 5

Conclusion and outlook

5.1 Conclusion

This research is dedicated to the development of membrane-based chemo-mechanical transducer system. The mechanical bending of a nano scale structure is caused by chemical or biological reaction induced surface stress, which is dominant under the scaling effect. For further experimental studies, a membrane-type chemo-mechanical transducer is fabricated with MEMS technology. It is noteworthy that using silicon nitride as the core material for the transducer has successfully overcome the challenges encountered by current technologies. Furthermore, integrated membrane transducer for chemomechanical transduction is developed for considering capacitance measurement and reaction chamber with total analysis system.

The response of the membrane-based chemo-mechanical transducer system towards temperature and pressure stimuli had been demonstrated. The sensitivity of the sensor is quantitatively confirmed by applying electrostatic force onto the membrane by using a bias voltage through the capacitance measurement circuit. Furthermore, common mode rejection is proven advantageous in the elimination of the signals from environmental disturbances such as temperature change, hydraulic

pressure and non-specific adsorption. This is crucial to the verification of pure chemo-mechanical transduction that arose from specific molecular interaction.

In-depth studies on the immobilization and interaction of biomolecules are important for the successfully molecular immobilization on the gold surface and molecular interaction to generate large surface stress. Moreover, the main principle of chemo-mechanical transduction regarding electrostatic force that causes repulsion between molecules is investigated with the introduction of cations contained in bio buffer solution. After gaining insights into chemo-mechanical transduction, investigations are carried out in search of the molecules that are responsive to thrombin protein which plays pivotal role in blood coagulation. Specific molecule interacting with thrombin is identified, which chemical reaction can be explained by thermodynamic principle. They are then adopted into the membrane transducer system. Lastly, the signal produced from thrombin protein detection is analysed through finite element simulation (ABAQUS).

Ongoing research work will be focused on the integration of gold nano rod in the membrane transducer and the suppression of non-specific adsorption taking place in bio molecular immobilization to further improve the performance. Also, the reaction gold partially covers the sensing surface while the rest of the surface (silicon nitride) is open and vulnerable to the non-specific adsorption of target molecules. The non-specific adsorption event alters the wettability of the open surface and eventually produces undesirable signal that impacts the sensing accuracy. Thus, the wettability alterations have to be prevented by means of coating with bio-repellent hydrophilic polymers, such as polyethylene glycol

(PEG), vinyl acetate (VA) and acrylic acid (AA). In future, one can hope to see the application of the system in the diagnosis of disease like cardiac vascular and leukaemia that requires multiple detection.

5.2 Future Work

The membrane transducer system shows the attractive points such as robust structure, electric measurement and real-time monitoring, but large constrains of membrane structure decrease the sensitivity of molecular interaction. We will investigate the integration of developed nano-rod on the membrane to increase the sensitivity. Furthermore, at the mass array system, we will apply the corresponding factor of sensitivity of each membrane transducer for the quantitative detections of multiple biomarkers.

5.2.1 Sensitivity Enhancement with Gold Nano Rod

The fabricated GNAs peripherally suspended on Si₃N₄ thin membrane enhance the surface stress from molecular interaction described in figure 5-1 which are grown on the nano-pore templates using AAO of an electrochemical perforation on the wafer. The template-based techniques provide cost-effective processes to fabricate metallic nanostructure arrays for diverse device applications. The techniques are innovative and reproducible fabrication method for realizing highly ordered arrays of freestanding GNRs perpendicular to substrates. Using an electrochemical perforation, chemical etching and cathodic polarization to the barrier layer of the

AAO templates, large-scale (about 775 mm²) and well-aligned GNRs are achieved without wire agglomeration, and the length of the nanowires can reach more than 170 nm.

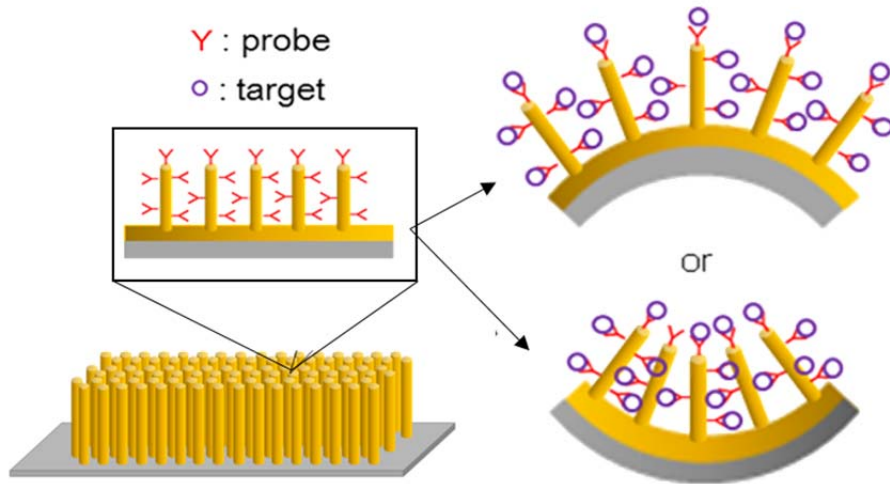


Figure 5-1. Signal enhancement approach to use nano structures which are made of anodic alumina oxide template.

The process for the fabrication of GNAs on thin membranes is schematically shown in figure 5-2. Firstly, a thin silicon nitride layer is deposited on both sides of a 4 inch, [100] direction, silicon wafer by low pressure chemical vapour deposition (LPCVD) 5-2(b). A square pattern is defined on the silicon nitride layer by photolithography and then the dry etch of silicon nitride film 5-2(c) and the silicon wet etching are used to float the silicon nitride membrane 5-2(d). The seed layers of 10 nm Ti / 20 nm Au and the aluminium film of 2 μm thickness are sequentially evaporated in the vacuum of 5×10^{-6} torr on a whole silicon substrate by electron beam evaporation 5-2(e). The samples are anodized as deposited to form the nanopore templates 5-2(f). The anodization is carried out with constant voltage mode

with 40 V in a 0.3M oxalic acid solution of 17°C until the aluminium is fully anodized with confirming current flow. A platinum mesh is employed as a counter-electrode. The barrier layer of AAO is removed by 10wt% phosphoric acid (H₃PO₄) solution for 40 minutes at 17°C. Electroplating is then performed with a dc voltage of 3.0 V shown in figure 5-2(g). The AAO employed as a template is removed with 10wt% phosphoric acid (H₃PO₄) solution for 1 hour at 60°C 5-2(h). The samples are finally rinsed with distilled water and dried in an oven at 70°C.

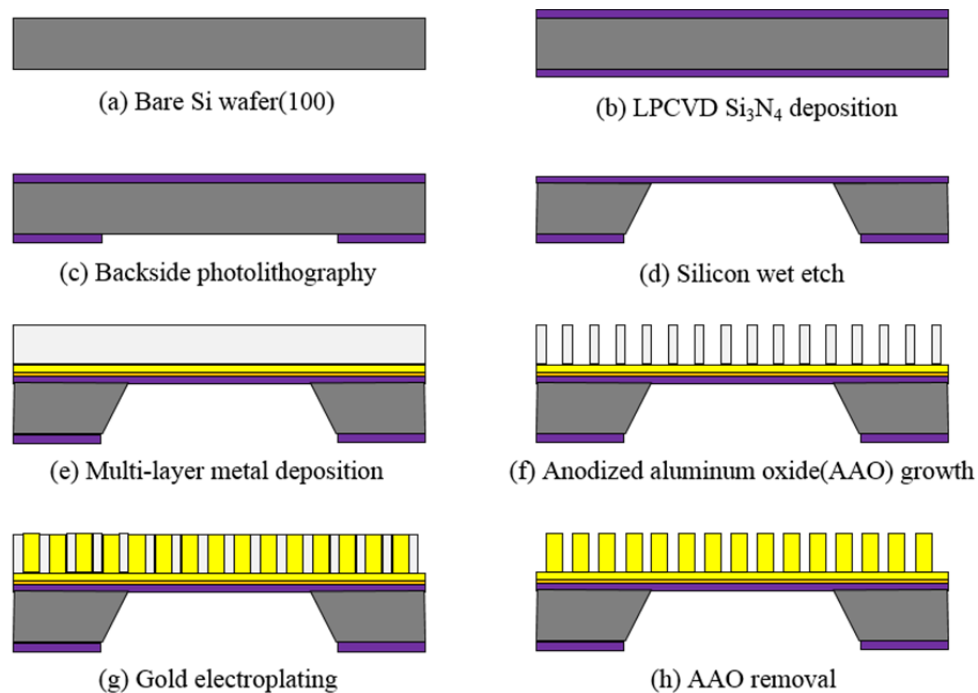


Figure 5-2. Fabrication process flow of GNR on silicon nitride membrane.

The morphologies and the structures is examined by FE-SEM. Figure 5-3 show the surface morphology of a 2µm-thick anodic aluminium oxide film before the electroplating of GNRs. The AAO film is the state to be formed on a 100 nm thickness and 500 µm x 500 µm peripherally suspended silicon nitride membrane

by an anodization after the removal of the oxide barrier layer at the bottom of the pores which is an insulating layer to obstruct the direct special and electrical contact to a substrate. In the Figure 5-3(a), (b), it clearly show nano-pores but it seems to be disordered distribution because the evaporated aluminium on a substrate is anodized with only the one step anodization due to the thickness limitation.[1] The vertical nano-pores are clearly shown in the cross-sectional view of figure 5-3(c). After removal of barrier layer form AAO template and pore widening process, the electroplating of gold is carried out with DC, with the Au layer exposed to the pores as the cathode shown in figure 5-3(d).

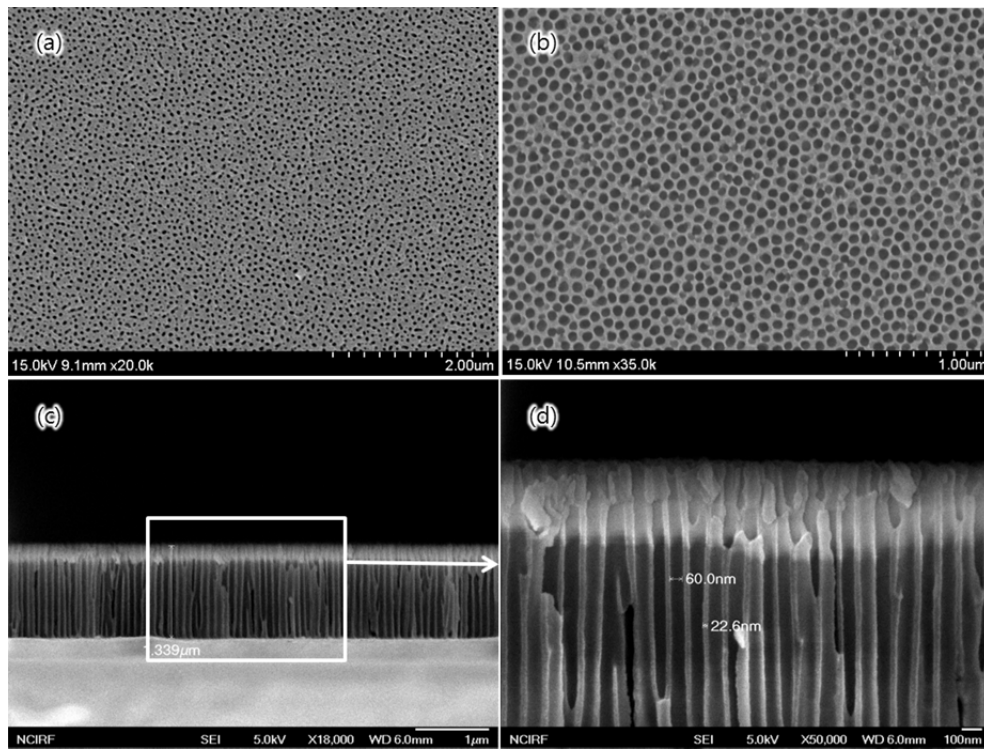


Figure 5-3. SEM images of the anodized aluminum oxide for nano rod template on suspended membrane.

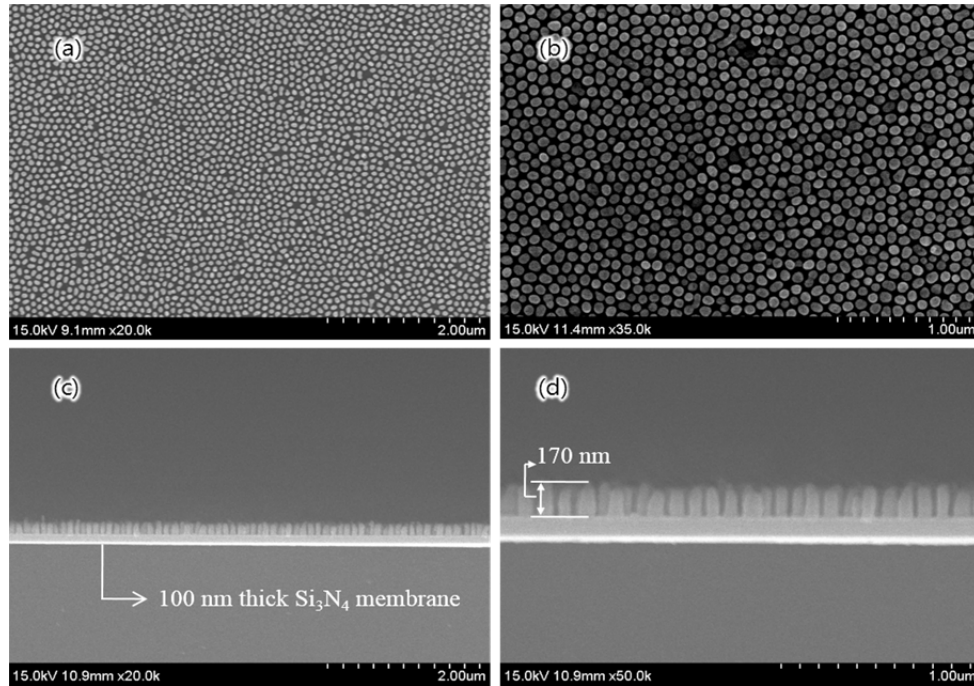
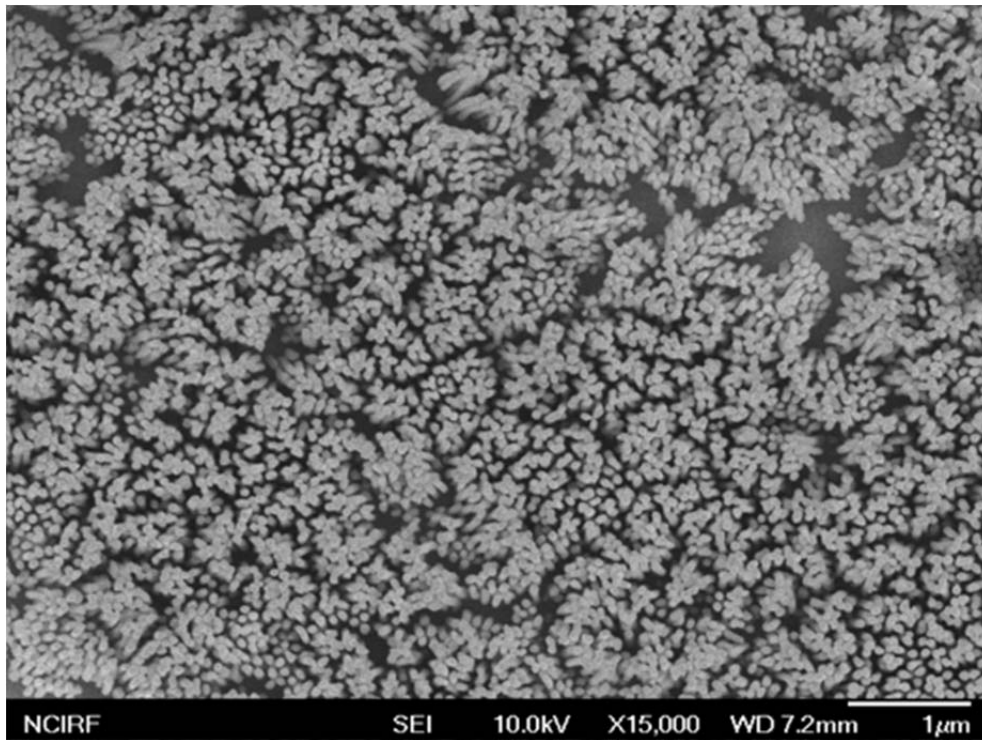


Figure 5-4. SEM images of the GNRs on 100 nm-thickness suspended Si₃N₄ membrane.

The pores are completely occupied with GNRs from their bottom and the length of GNRs is highly uniform. After removing the AAO layer with 60 °C, 10wt% H₃PO₄, the SEM image of GNRs is shown in Figure 5-4. Figure 5-4(a) shows highly uniform GNRs growing vertically without aggregation. Pore widening minimizes the distance between pores, leading to a densely GNR packed structure. In addition, a layer of silicon nitride membrane with 100 nm thickness is deposited beneath the gold structure in order to verify the fact that increase of surface stress enhances the response of chemo-mechanical transduction. Furthermore, a higher aspect ratio GNR array is grown on the membrane which is increased to the length of 170 nm from 70 nm without aggregation. Figure 5-4(d) shows densely standing together on

the membrane. However, super high aspect ratio of about 500 nm long GNR array is shown in Figure 5-5, where agglomeration of the GNRs takes place.



**Figure 5-5. High aspect ratio of GNRs after removal of an AAO template
(Length: ~ 500 nm, Diameter: ~70nm, aspect ratio: 7.14).**

5.2.2 Sensitivity Compensation for Quantitative Detection

The deflection of membrane on membrane transducer system is measured with the capacitance value between flexible membrane electrode and rigid nickel metal electrode. The material properties of membrane is crucial factor for the response performance of the transducer depending on the Plate.[2] In the semiconductor industry, the uniformity of thin film deposition on the wafer and in the batch has been researched to obtain reliable products. Although silicon nitride for membrane transducer is very stable material compared with polymers such as PDMS[3, 4] and parylene[5], it also has reliability problem due to demanding wide dynamic range and high sensitivity. To reduce the variation, silicon nitride is growth with mass production, low pressure chemical vapor deposition equipment on the strictly controlled condition. Nevertheless, it has inevitable variation on the wafer, as described in figure 5-6. The effect of thickness variation for the performance not clear, but it make some difference within chips for highly quantitative data.

The 4 inch wafer deposited with silicon nitride is constructed to integrate membrane transducer through surface and bulk micromachining. Most of the fabrication process uses the equipment rather than manual handwork. The integrated membrane transducer consists of rigid nickel structure, thin metal electrode on top of the membrane, oxide spacer, electrode contact pads and reaction chamber. The two parallel electrodes conduct capacitive measurement to measure the amount deflection of flexible membrane. In the wafer, over five thousand of sensors are well fabricated without one defect sample shown in figure 5-7. The mass produced micromachined membrane transducers show the highly identical

feature without some deformation of nickel and membrane structure, but the performance of sensors has some difference due to a stack of tiny variation on each step during the fabrication. The membrane transducer can be characterized by commercial LCR meter (Agilent E4980A) to measure the capacitance value of sensors.

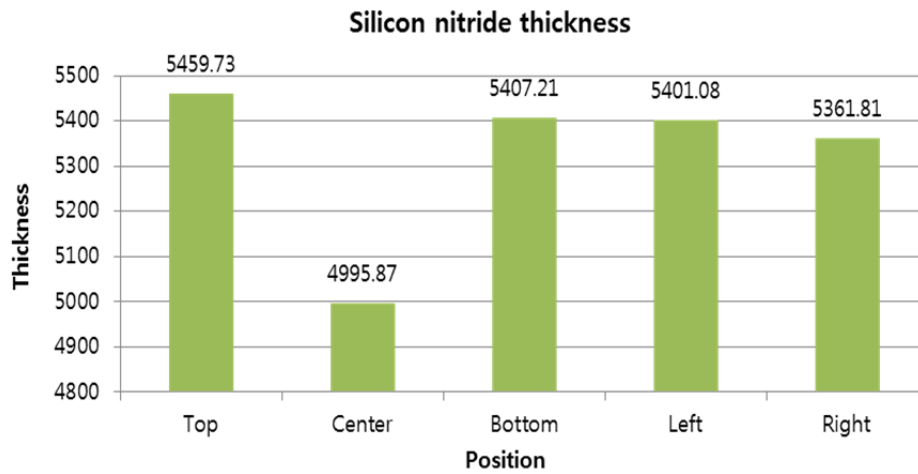


Figure 5-6. A 15 wafer average thickness of silicon nitride deposited by LPCVD at Inter-university Semiconductor Research Center at Seoul National University.

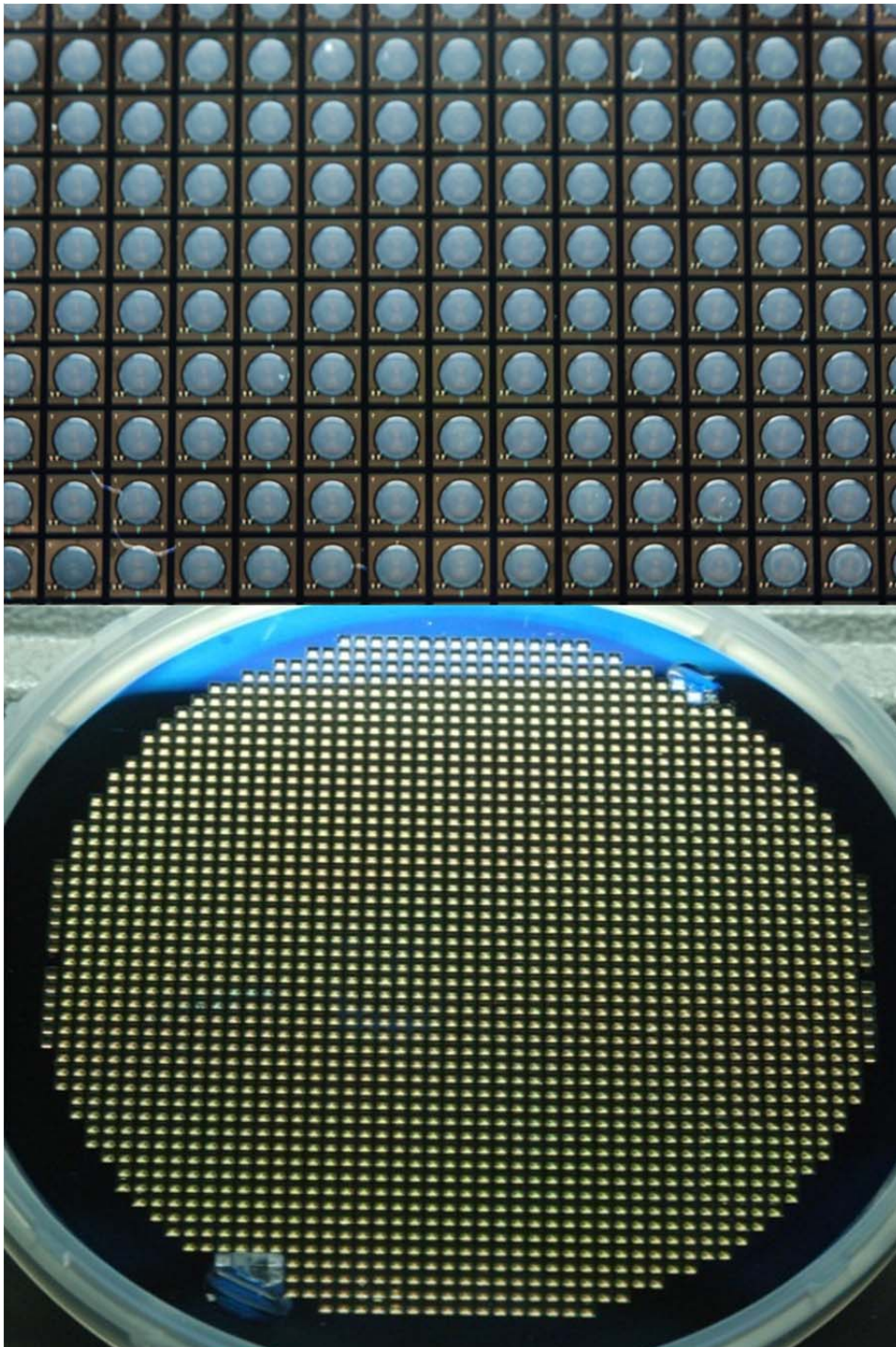


Figure 5-7. Thin membrane transducers are fabricated with MEMS technology

In the figure 5-8, an initial capacitance value of every sensor is measured with LCR meter of 100mV and 100 kHz. The equipment can apply bias voltage at the parallel plates which make electrostatic force between rigid nickel electrode and flexible membrane electrode. Thereby, the flexible silicon nitride membrane is deflected by the electrostatic force. The amount of deflection is decided with balancing between electrostatic force and mechanical restoring force of membrane body. Thus a sensitivity of the membrane sensor is defined with the change value from initial value of capacitance to the value of capacitance applying a certain bias voltage. In the figure 5-9, the initial capacitance values and capacitance changes from initial capacitance value to the capacitance applying 40 bias-voltage are mapped at the position of the wafer, and the performance of membrane transducer is affected by the properties of silicon nitride.

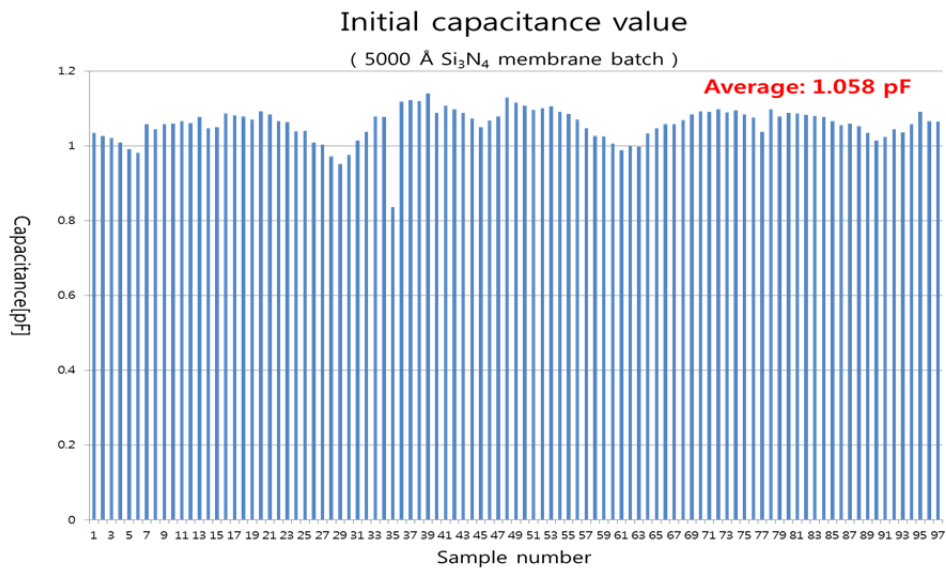


Figure 5-8. Initial capacitance value of membrane transducer.

4 inch wafer

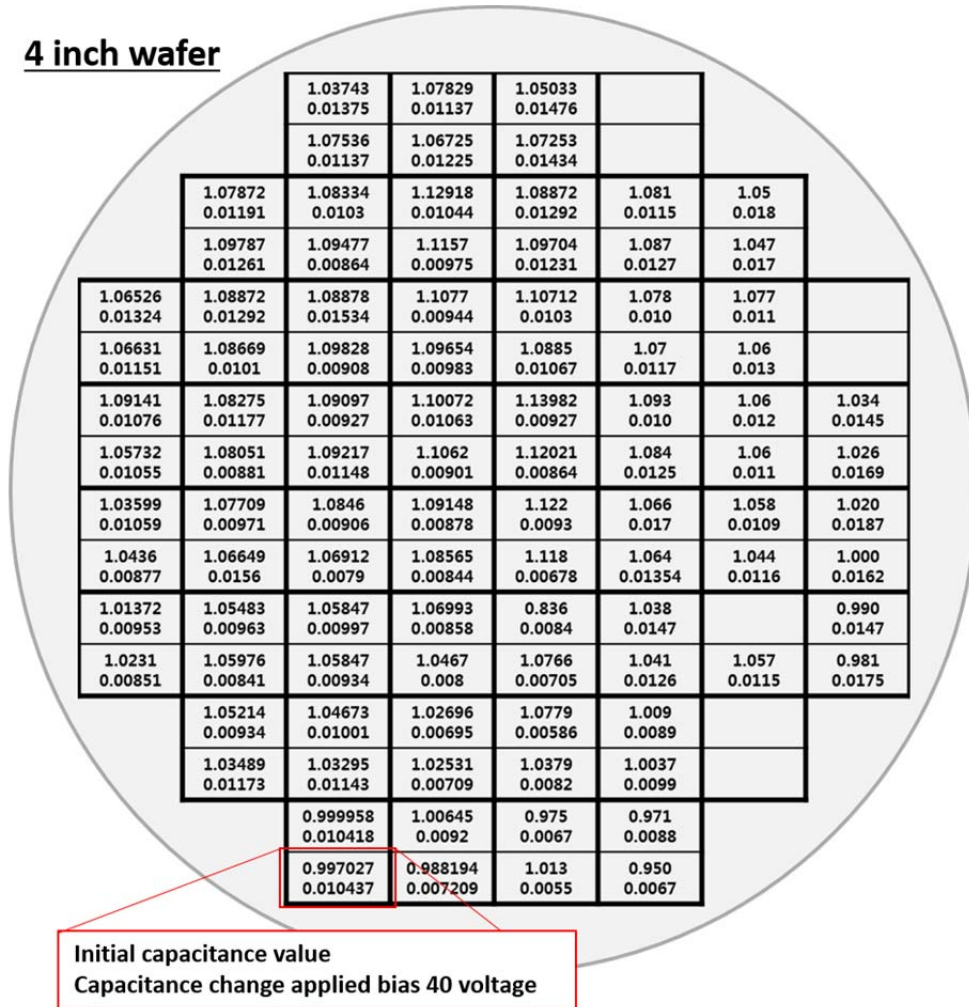


Figure 5-9. The initial capacitive value and capacitive change of transducers applied with a 40 bias-voltage. Also, this four inch wafer map shows the difference of sensor sensitivity.

Although these micro structure systems are highly irritable due to tiny variation, our thin membrane transducer has powerful structures to not only measure the capacitance of sensor, but also confirm the sensitivity of sensor by using electrostatic force.

We choose 50 samples randomly from the membrane transducer and deposit gold layer for molecular reaction on the backside of them with a self-aligned shadow mask. 11-MUA is coated to protect the contamination of gold and then PCB package is done by wire bonding. The initial capacitance uniformity of the membrane transducer sensor decreases after the package process (figure 5-10) which is caused by the parasitic capacitance's change from wire and PCB.

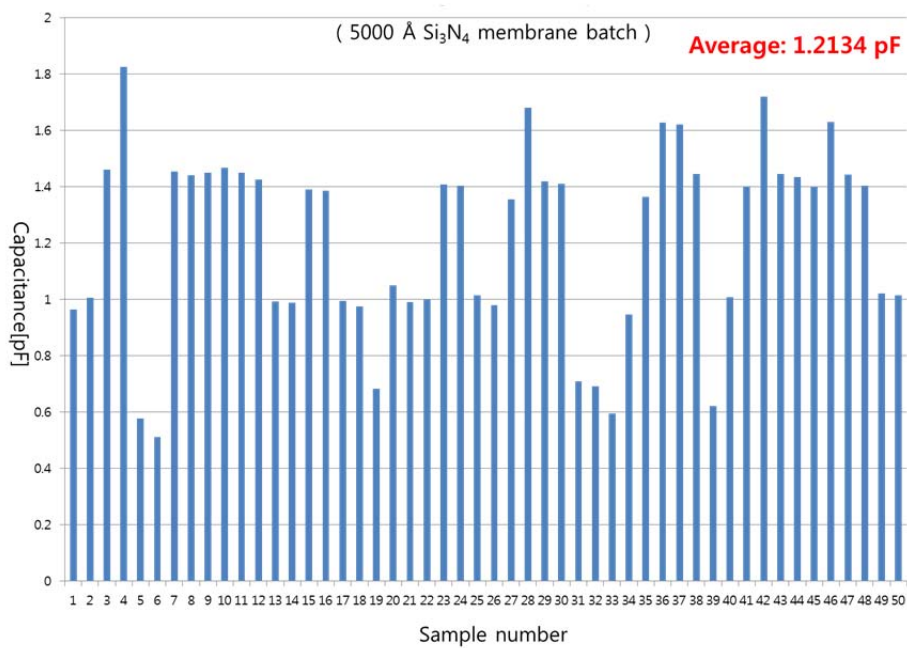


Figure 5-10. The initial capacitive values of the membrane transducer after the packaging with PCB.

In addition, we measure the capacitance of membrane transducer by LCR meter as change the bias voltage from 0 to 40 V in every 0.2 V steps with 0.5 second time interval (total 200 data). Figure 5-11 shows the difference between the capacitance measured at 40 V bias voltage and initial capacitance. The difference indicates

membrane deflection due to electrostatic force and it is strongly related to the sensitivity of the sensor.

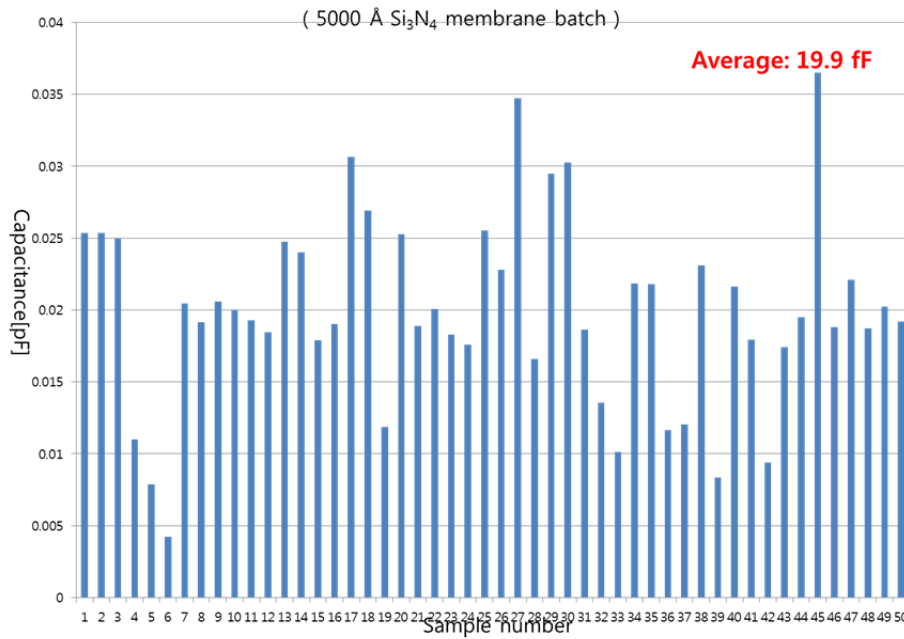


Figure 5-11. The change of capacitive value applied with the bias voltage of 40V.

200 data measured by LCR meter according to bias voltages are normalized by dividing with the average and plotted in terms of apply voltages. The results of the every 50 sensors meet at 24 V. This means all the 50 sensors has the same specification. In other words, if each sensor has the function of apply voltage and membrane deflection, the function, $f(x)$, will be high order and expressed like below.

$$F(x)_i = \alpha f(x) + \beta$$

Equation 5.2-1

, where α is the sensitivity of membrane transducer, β is initial capacitance value included with parasitic capacitance of PCB package.

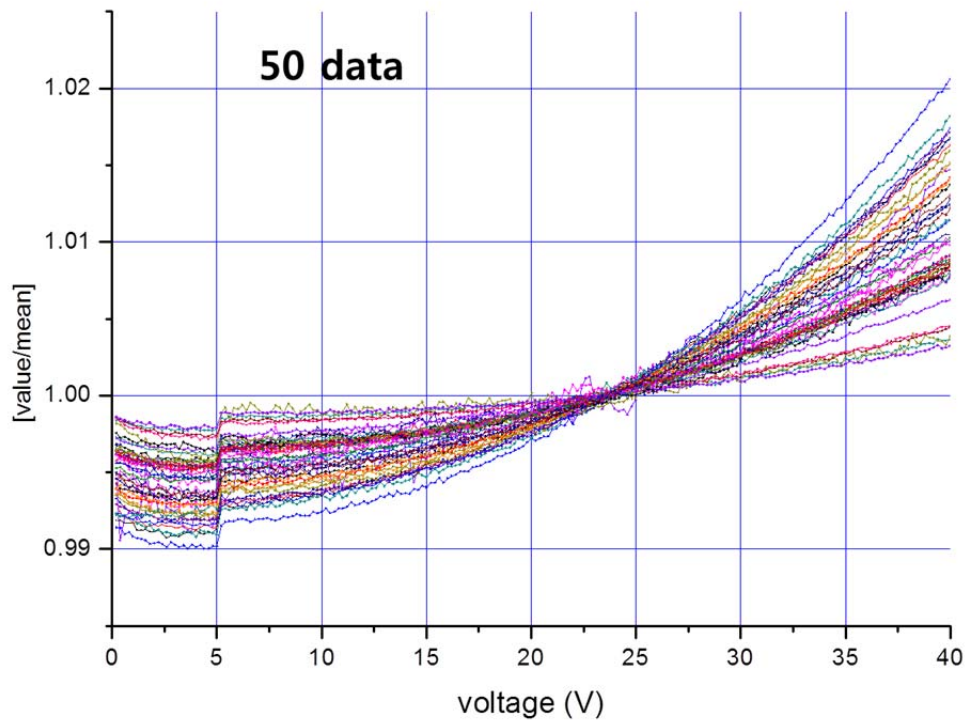


Figure 5-12. The normalized capacitive changes are induced due to the electrostatic force of the applied voltages

Figure 5-12 shows the C-V graph of 50 transducers. The results indicate that 50 sensors have identical function $f(x)$ in equation 5.2.1. However, these have different sensitivity that allows using the least square fitting describe in equation 5.2-2. Firstly, one membrane transducers is chosen for the criteria from the normalized capacitance values. In this case, 27th sample is a criterion, and other samples, except for 27th one, are multiplied by K which is fitting value. K is the

minimum value that makes the square of the difference between criteria data and fitting data, equation 5.2-2.

$$\sum_{i=1}^n [kF_i(x_i) - F_{criteria}]^2 = \text{Minimum} \quad \text{Equation 5.2-2}$$

Calculate the K value using the measurement results of 50 sensors like table 10 and multiply it with capacitance values. Every capacitance graphs according to applied voltage converges into one fitting data graph (blue) in figure 5-13. $F_i(x_i)$ is the function of capacitance values according to electrostatic force, i is sensor number, and x is the applied bias voltage in equation 5.2-3. Fitting value, k , is the value that results 0 of the differential of equation 5.2-3 in terms of k .

$$\frac{\partial \{\sum_{i=1}^n [kF_i(x_i) - F_{criteria}]^2\}}{\partial k} = 0 \quad \text{Equation 5.2-3}$$

Table 10. The sensitivity compensation factor of membrane transducer

	1	2	3	4	5	6	7	8	9	10
0	1.2078	1.2405	1.8298	5.6413	2.7641	5.8730	2.2562	2.3593	2.2371	2.3060
10	2.3420	2.4408	1.2019	1.5672	2.4586	2.3549	1.0000 criteria	1.1322	1.9524	1.2975
20	1.6608	1.5813	2.4409	2.5527	1.2300	1.3602	1.2095	3.2968	1.4985	1.4491
30	1.4698	1.7871	2.1002	1.3618	1.9524	4.7478	4.5445	2.0001	2.6300	1.4726
40	2.4986	6.4541	2.5909	2.4394	1.1878	2.7314	2.0400	2.4224	1.6141	1.6946

It is an essential technology for quality control of membrane transducer with a simple electrical way. Furthermore, these data can be used for quantitative detection of chemo-mechanical transduction for chemical/biological detection.

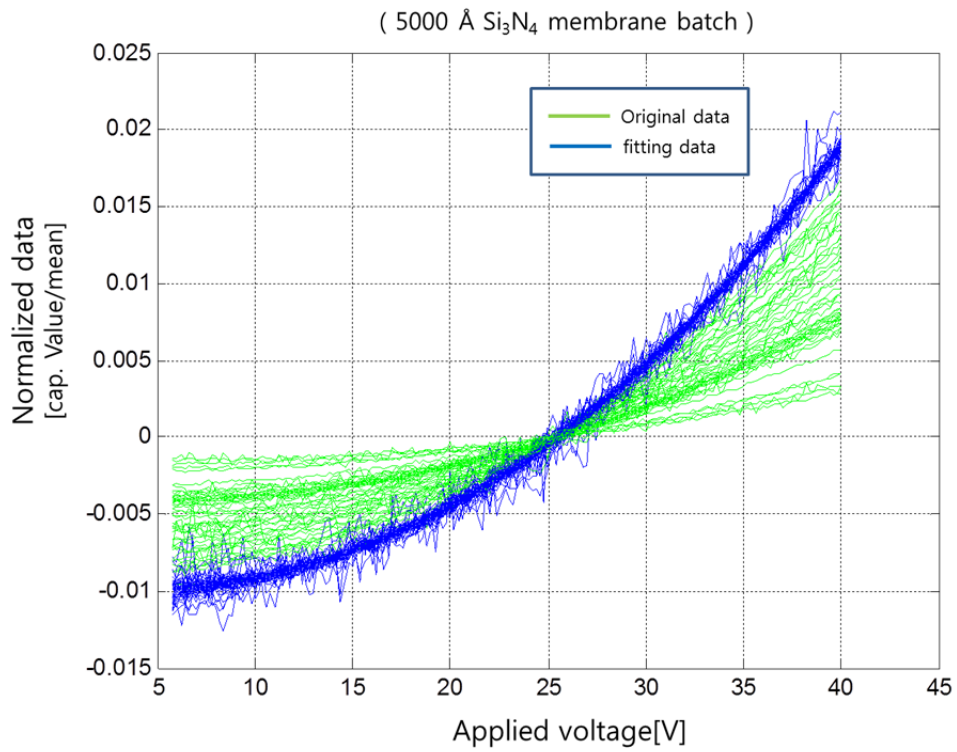


Figure 5-13. The compensation data of capacitance change according to the applied voltage.

Figure 5-14 is the sensitivity test results of capacitance measurement circuit for bio molecule detection as AC level voltage changes with 2.3, 1.68, 1.12, 0.56V. Chips are selected from the results.

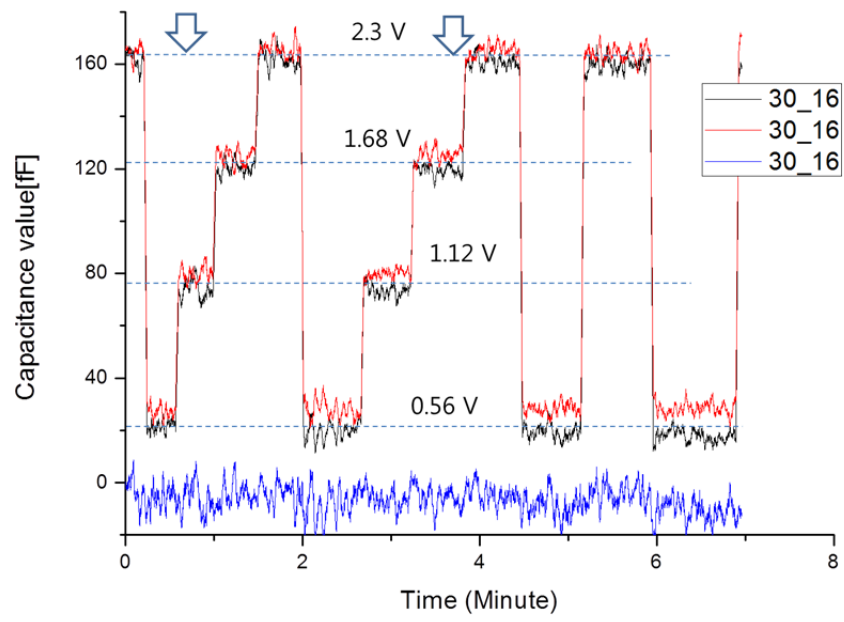


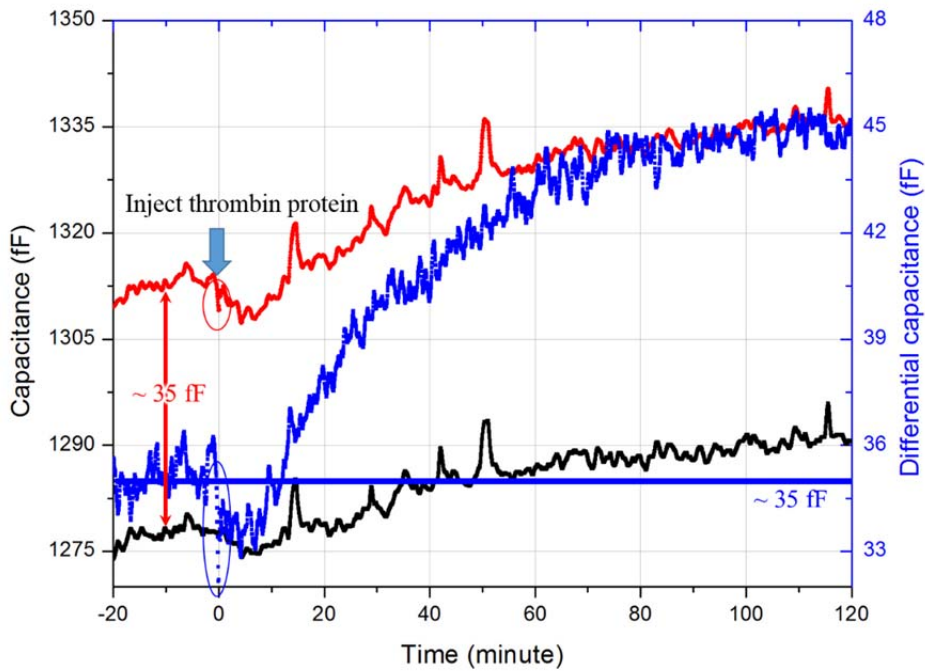
Figure 5- 14. The sensitivity of membrane transducer is confirmed by changing AC level voltage on the capacitive measurement system.

5.3 Reference

1. Mao, R.W., S.K. Lin, and C.S. Tsai, *In situ preparation of an ultra-thin nanomask on a silicon wafer*. Nanotechnology, 2009. **20**(2): p. 025301.
2. Cardinale, G.F., et al., *Analysis of residual stress in cubic boron nitride thin films using micromachined cantilever beams*. Diamond and Related Materials, 1996. **5**(11): p. 1295-1302.
3. Cha, M., et al., *Biomolecular detection with a thin membrane transducer*. Lab Chip, 2008. **8**(6): p. 932-7.
4. Sang, S. and H. Witte, *A novel PDMS micro membrane biosensor based on the analysis of surface stress*. Biosens Bioelectron, 2010. **25**(11): p. 2420-4.
5. Satyanarayana, S., D.T. McCormick, and A. Majumdar, *Parylene micro membrane capacitive sensor array for chemical and biological sensing*. Sensors and Actuators B: Chemical, 2006. **115**(1): p. 494-502.

Appendix

A. Data polishing



Appendix 1. The raw data graph is original of figure 4-21

The raw data of figure 1 is from the aptamer interaction with 100nM thrombin protein which is original graph of figure 4-21. The difference of initial capacitance from between sensor and reference transducer is $\sim 35\text{fF}$. To compare the quantitative signal from the concentration of target molecule, the differential valve

is moved to zero point at the injection time of target molecule. The table 11 show the Y axis offset value on the each experiment of target concentration.

Table 11. The capacitance offset value of reference transducer

Concentration	2000	2000	1000	500	500
Y axis-Offset	1	-8	0	71	23
Concentration	500	100	100	50	50
Y axis-Offset	52	83	35	38	3.5
Concentration	10	10	10	1	0.1
Y axis-Offset	9	24.2	22.3	20	32.5
Concentration	0.1	0.01	0.01	0.01	0.01
Y axis-Offset	36.2	9.8	36.1	38.5	22

This is the code of MATLAB program for filtering the data of biomolecular experiment.

```
%%%%%%%%%%%% Butterworth IIR Low pass filter %%%%%%%%%%
```

```
Clear
```

```
format long;
```

```
data=xlsread('Before_Every concentration.xlsx');
```

```
%%%%%%%%%
```

```
sample_num=size(data,2)-1;
```

```
time_num=size(data,1)-2;
```

```
%%%%%%%%%
```

```
timelength=data(time_num+2,1)-data(3,1);
```

```
Ts=timelength/(size(data,1)-2);
```

```
Fs=1/Ts; %sampling freq.
```

```
x=zeros(time_num,1);
```

```

y=zeros(time_num,sample_num);

for i=1:1:time_num
    x(i,1)=data(i+2,1);
    for j=1:1:sample_num
        y(i,j)=data(i+2,j+1);
    end
end

%%%%%% Cut-off frequency %%%%%%%
n=1;
Wn=0.05; % cut off freq.
%%%%%%%%%%%%%%%%%%%%%%%%%%%%%%%%%%%%%%%%%%%%%%%%%%%%%%%%%%%%%%%%%%%%%%%%

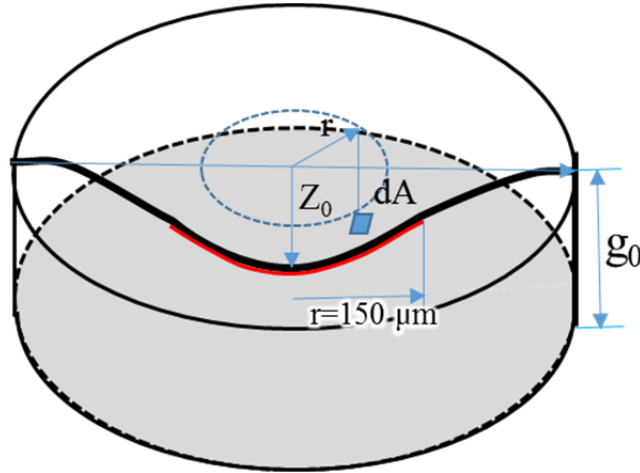
Fn=Fs/2; % Nyquist frequency
Ftype='low';
[b,a]=butter(n, Wn/Fn, Ftype);
y_filtered=zeros(time_num,sample_num+1);
y_1=zeros(time_num,1);
for j=1:1:sample_num
    y_1=filter(b,a,y(:,j));
    for i=1:1:time_num
        y_filtered(i,1)=x(i);
        y_filtered(i,j+1)=y_1(i);
    end
end

```

end

xlswrite('Filtered_data.xlsx', y_filtered);

B. Membrane deflection according to Capacitance change



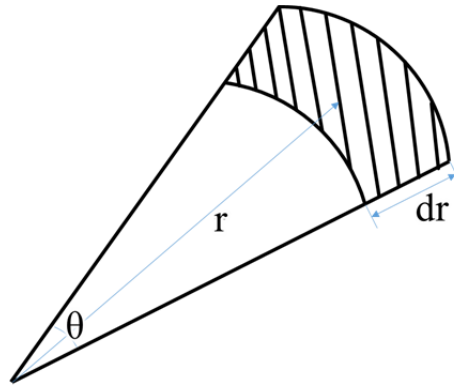
Appendix 2. Schematics of capacitance calculation

We can calculate the capacitance change using the approximation profile of the membrane. One critical assumption to close form calculation is that the membrane is circular, homogeneous, all clamped. It is also assumed that the profile assumption is equation A-1.

$$Z(r) = Z_0 \left[1 - \left(\frac{r}{R} \right)^2 \right]^2 \quad \text{Equation A-1}$$

where Z_0 , r and R is the initial deflection of membrane, the radius of electrode and the radius of membrane, respectively. Z_0 is not zero due to hydraulic pressure. The capacitance value is integral of differential area element shown in equation A-2. Capacitance is proportional with area and inversely proportional with distance of electrodes.

$$C = \int dc = \int_0^{2\pi} \int_0^r \frac{\epsilon_0 dA}{g_0 - z(r)} \quad \text{Equation A -2}$$



Appendix 3. The infinitesimal area of curved membrane

The infinitesimal area element is equation A-3.

$$dA = r dr d\theta \quad \text{Equation A -3}$$

the equation, A-3, is substituted in equation A-2,

$$C = \int_0^{2\pi} \int_0^r \frac{\epsilon_0 * r * dr * d\theta}{g_0 - z_0 \left[1 - \left(\frac{r}{R}\right)^2\right]^2} \quad \text{Equation A -4}$$

With integral equation A-4 with lower electrode size

$$C = \int_0^{2\pi} \frac{1 * \epsilon_0 * R^2 * \tanh^{-1} \left[\frac{\sqrt{z_0} * (R^2 - r^2)}{\sqrt{g_0} * R^2} \right]}{2 * \sqrt{g_0} * z_0} \Bigg|_0^{150e-6} \quad \text{Equation A -5}$$

The capacitance equation of curved membrane is

$$C = \frac{\pi * \epsilon_0 * R^2 * \tanh^{-1} \left[\frac{\sqrt{z_0} * (R^2 - r^2)}{\sqrt{g_0} * R^2} \right]}{\sqrt{g_0} * z_0} \Bigg|_0^{150e-6} \quad \text{Equation A -6}$$

This is the code of MATLAB program for calculating the capacitance according to membrane deflection.

```

%%%%%%%%%% Transducer design parameter %%%%%%%%%%%

Clear

e0=8.854e-12;          %% Dielectric constant
g0=6.0e-6;            %% Electrode gap
R=375e-6;            %% Radius of membrane
v=0.27;              %% Poisson ratio
E=310e9;             %% Young's modulus
t=500e-9;            %% Thickness
D=E*t^3/(12*(1-v^2));  %% Flexible rigidity
q=1000*9.8*4e-3;     %% Hydraulic pressure
r=150e-6;            %% the radius of lower electrode
%%%%%%%%%%
z0=1.3*10^-6;        %% Initial deflection
C0=(pi*e0*R^2)*atanh(sqrt((z0/g0)*((R^2-r^2)/R^2)))/(sqrt(g0*z0));
z=linspace(z0,z0+80*10^-9,10001); %% The deflection according to surface stress
CC=zeros(1,10001);  %% 10000 point loop
for k=1:1:10001
    xx=z(k);
    C=(pi*e0*R^2)*atanh(sqrt((xx/g0)*((R^2-r^2)/R^2)))/(sqrt(g0*xx));
    CC(k)=C;
end

plot(z-z0,CC-C0);    %% Plot the graph

```

```

array(:,1)=z-z0;                                %% Data out
array(:,2)=CC-C0;                               %% Data out
xlswrite('data_6.xls',array);                   %% Data out
%%%%%%%%%%%%%%%%%%%%%%%%%%%%%%%%%%%%%%%%%%%%%%%%%%%%%%%%%%%%%%%%%%%%%%%%

```

C. Dissociation Constant

The dissociation or affinity constant, K_D , of thrombin binding aptamer is calculated by using the experimental data for the capacitance change versus concentration measured at equilibrium state of the reaction. One critical assumption to guarantee the accuracy of the calculation is that the reaction is reached to the equilibrium at 120 minute. It is also assumed that the surface coverage is linearly related with the magnitude of the capacitance change. Thus the reactant coverage on the sensor surface can be normalized by the maximum capacitance change.

Langmuir isotherm is expressed by the equation below.

$$S = \frac{K_e P}{1 + K_e P} \quad \text{Equation B -1}$$

where K_e is the equilibrium constant and P is the concentration of the target molecule, i.e., the thrombin protein. In the simple ligand-receptor binding process, the dissociation constant is the reciprocal of the equilibrium constant, thus

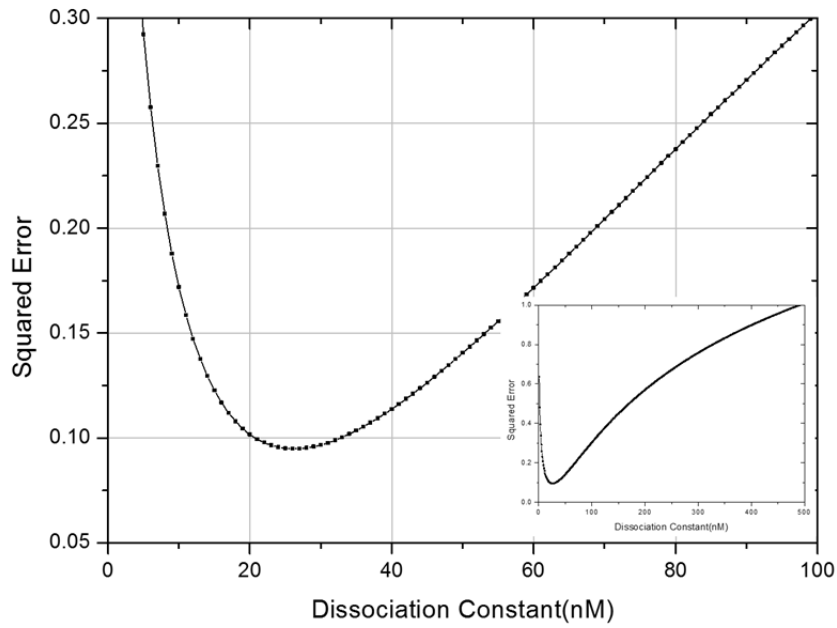
$$K_D = \frac{1}{K_e} \quad \text{Equation B -2}$$

The result of thrombin experiment is summarized in the table 12.

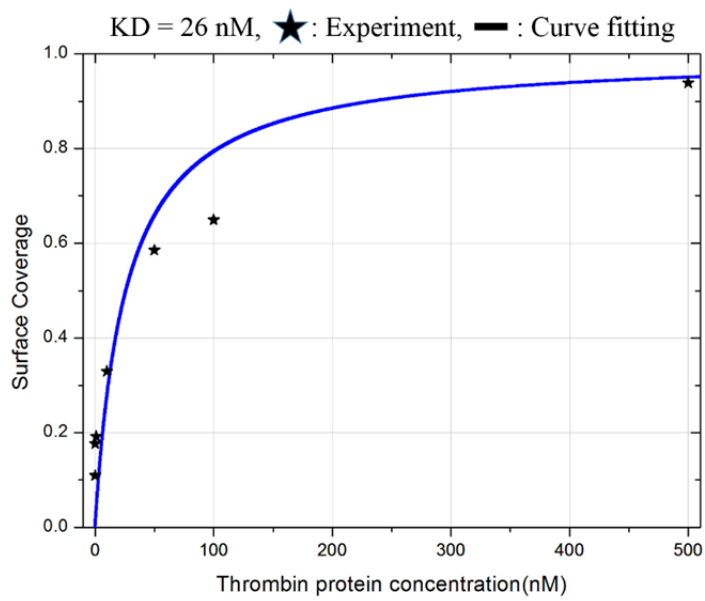
Table 12. The thrombin detection result of membrane-based chemomechanical transducer system.

Protein concentration [nM]	0.01	0.1	1	10	50	100	500	1000	2000
Average Capacitance Change [fF]	1.64	2.65	2.88	4.94	8.78	9.74	14.08	32.16	31.08

We will curve fit the given data above to find the best value of KD that minimizes the square error between the capacitance change normalized by the largest value and the surface coverage at the given KD. However, extra functional terminals are not blocked at the experiment of 1,000 nM and 2,000 nM, so we exclude the two data points at 1000 nM and 2000 nM. We try the curve fitting process and the square error vs. KD value graph is shown in figure 4. Furthermore, the graph inform that the dissociation constant to achieve the minimum square error is at KD = 26 nM. We can draw the Langmuir isotherm at this condition as below. The curve fitting appears reasonably consistent with the experimental results. It is concluded that the affinity of the thrombin on the aptamer with current molecular configuration on the surface is 26 nM described in figure 5.



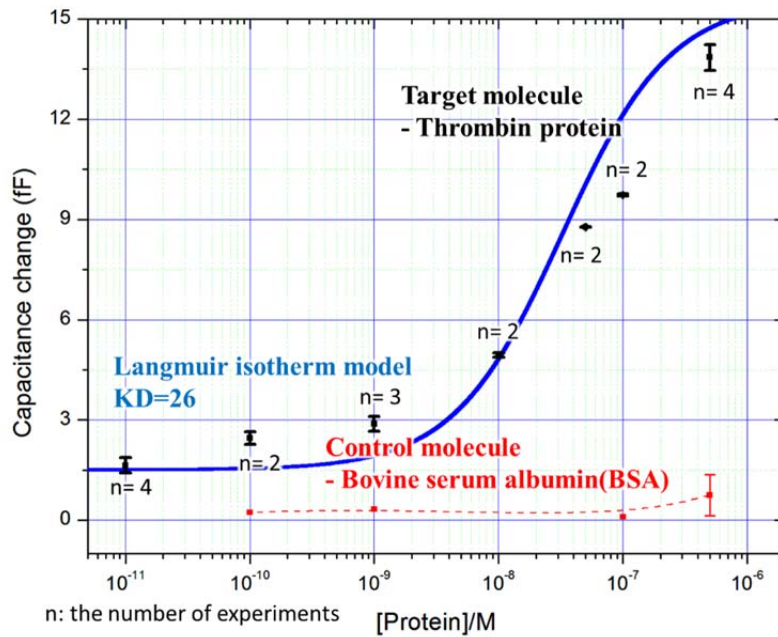
Appendix 4. The curve fitting of square error vs. KD value.



Appendix 5. The curve fitting with experimental result at the dissociation constant of 26 nM.

The sensitivity of micromechanical detection is investigated by performing binding experiments at a total of seven different thrombin concentrations (over 2 times for

each concentration). Figure 6 shows the differential capacitance change due to membrane deflection as a function of thrombin concentration (logarithmic scale). The sensor response follows a Langmuir isotherm-type behavior, and the resulting curve can be fit using the least squares method to reveal a dissociation constant of 26 nM explained.



Appendix 6. Repeat experimental result and large dynamic range of membrane transducer.

%%%

clear

cc=[0.01 0.1 1 10 50 100 500]; %% Thrombin concentration

S=[1.64 2.65 2.88 4.94 8.78 9.74 14.08]; %% Experimental cap. data

S=S/14.08; %% assumption

gap=zeros(1,10000); %% Define

```

S_real=zeros(1,10000);          %% Define
array=zeros(10000,4);          %% Define

for KD=1:1:10000
    for i=1:1:7
        s1=cc(i)/(KD+cc(i)); %%KD:dissociation constant, cc:target concetration
        s2=(s1-S(i))^2;
        gap(KD)=gap(KD)+s2;    %% The sum of squared error
    end
    array(KD,1)=KD;            %% Data out
    array(KD,2)=gap(KD);      %% Data out
end
for KD=1:1:10000
    if (gap(KD)==min(gap))    %% Minimum of KD
        KD
        xx=logspace(-4,log10(2000),10000);  %%%Range of concentration
        for i=1:1:10000 %%%
            s1=xx(i)/(KD+xx(i));
            S_real(i)=s1;
        end
        break;
    else
        end
end
% plot(xx,S_real);          %%Plot graph
array(:,3)=xx;             %% Data out
array(:,4)=S_real;        %% Data out
xlswrite('data.xls',array); %% Data out

```

%%%%%%%%%

D. The code of sensitivity compensation factor

Clear

Format long

%% Change the value %%%%

%% The number of gizun is the sensor for criterion %%%%

%% The number of delete is the number of excepted sensors, default value is
zero %%

gizun = 5;

delete = 0;

raw_data=xlsread('test_linear.xls');

%% data = (measured capacitance value, the number of sensor)

%% voltage = The value of x axis

data=zeros(size(raw_data,1)-1,size(raw_data,2)-1);

voltage=zeros(size(raw_data,1)-1,1);

for i=2:1:size(raw_data,2)

 for k=2:1:size(raw_data,1)

 data(k-1,i-1)=raw_data(k,i);

 end

end

for k=2:1:size(raw_data,1)

 voltage(k-1)=raw_data(k,1);

end

```

row=size(data,1);
col=size(data,2);

%% sum ← the sum of measured capacitance value of each sensor
sum=zeros(1,col);
%% nor_data ← Normalized value which the value is divided by average of
capacitance value
nor_data=zeros(row,col);
nor2_data=zeros(row,col);
%% fitted ← fitting value of each sensor
fitted=zeros(row,col);

for i=1:1:col
    for k=1:1:row
        sum(i)=sum(i)+data(k,i);
    end
    for k=1:1:row
        nor_data(k,i)=data(k,i)/(sum(i)/row);
        nor2_data(k,i)=nor_data(k,i)-1;
    end
end

%% f2 ← criterion function , f1 ← The other function
%% f1f2 ←  $\sum f1 * f2$ , f1f1 ←  $\sum f1^2$ , f2f2 ←  $\sum f2^2$ 
f1f2=zeros(1,col);
f1f1=zeros(1,col);
f2f2=zeros(1,col);
kk=zeros(1,col);

```

%%% dist ← The amount of difference between criterion sensor and fitted value of the other sensor

```
dist=zeros(1,col);
```

```
temp_dist=zeros(1,col);
```

```
temp2_dist=zeros(1,col);
```

```
sort_dist=zeros(1,col);
```

```
number1=zeros(1,col);
```

%%% $d(\sum(kf1-f2)^2)/dk = 0$ %%% the function of fitting number (k) %%%%

```
for i=1:1:col
```

```
    for k=1:1:row
```

```
        f1f2(i)=f1f2(i)+polyval(polyfit(voltage,nor2_data(:,gizun),2),voltage(k))*polyval(polyfit(voltage,nor2_data(:,i),2),voltage(k));
```

```
            f1f1(i)=f1f1(i)+polyval(polyfit(voltage,nor2_data(:,i),2),voltage(k))^2;
```

```
            f2f2(i)=f2f2(i)+polyval(polyfit(voltage,nor2_data(:,gizun),2),voltage(k))^2;
```

```
        end
```

```
        kk(i)=f1f2(i)/f1f1(i);
```

```
    end
```

%%% dist function %%%%

```
for i=1:1:col
```

```
    for k=1:1:row
```

```
        dist(i)=sqrt((kk(i)^2*f1f1(i)-2*kk(i)*f1f2(i)+f2f2(i))/row);
```

```
    end
```

```
    %fprintf('%6.0f 번 %6.3f%% 차이\n',i,100*dist(i));
```

```
end
```

%%% The output from a large number of the errors in aligning after
correcting

```
temp_dist=roundn(100*dist,-5);
```

```
for i=1:1:col
```

```
    temp2_dist(i)=temp_dist(i)+(i*10^-7);
```

```
end
```

```
sort_dist=sortrows(transpose(temp_dist));
```

```
sort2_dist=sortrows(transpose(temp2_dist));
```

```
number1=round((sort2_dist-sort_dist)*10^7);
```

%%% Text print out %%%

```
fprintf(' ===== Result =====\n');
```

```
for i=col:-1:col-delete+1
```

```
    fprintf('%6.0f번 %6.3f%% 차이남 ← [제외됨]\n',number1(i),sort_dist(i));
```

```
end
```

```
for i=col-delete:-1:1
```

```
    fprintf('%6.0f번 %6.3f%% 차이남\n',number1(i),sort_dist(i));
```

```
end
```

```
for i=1:1:col
```

```
    for k=1:1:row
```

```
        fitted(k,i)=kk(i)*nor2_data(k,i);
```

```
    end
```

```
end
```

%%% Part for selecting the eliminated sensor

```
temp_num=zeros(1,delete);
```

```
for k=1:1:delete
```

```

    temp_num(k)=number1(col-k+1);
end
temp_num2=sortrows(transpose(temp_num));

%%% plotting without part for selecting the eliminated sensor
k=1;
for i=1:1:col
    if (k<(delete+1) && round(i-temp_num2(k))==0)
        k=k+1;
    else
        plot(voltage,fitted(:,i));
        hold on;
        plot(voltage,nor2_data(:,i),'g');
        %plot(voltage,fitted(:,i),'r');
    end
end
end.

```

국문초록

분자 상호작용 측정을 위한 박막 화학기계변환 시스템

화학기계변환은 실시간으로 표지 인자 없이 빠르고 효율적으로 대량의 분자 반응을 측정할 수 있는 큰 장점을 가지고 있다. 이 원리의 생화학 반응에 대한 측정은 유전 정보학과 단백질 유전학의 넓은 응용분야에 대한 흥미를 유발시켰다. 마이크로 외팔보 (cantilever)형 센서가 주류를 이루고, 구조와 재질 그리고 에너지 변환 원리에 따라 매우 다양하게 연구되었다. 이를 통해 유전자 상보결합, 항체-항원, 심지어 세포 결합의 유용한 측정을 보였지만, 광학적 측정 방식은 소형화를 어렵고 불투명한 액상 분석물질의 측정이 불가능하다. 더 나아가, 유체의 흐름에 취약한 구조와 외팔보 뒷면의 비특이적 결합으로 비이상적 구조 변형을 일으키기 쉽다. 이러한 구조적 취약점을 극복하기 위하여 박막 구조의 화학기계변환이 개발되었다. 박막은 분자 반응부와 측정부를 물리적으로 분리하여 전기적 측정의 적용이 용이하다. 또한 박막 구조의 안정성으로 반응부에 특이적 반응분자 고정화가 쉬우며, 상용적인 프린트 기술의 접목으로 표면 기능화도 용이하다. 마지막으로 고립된 분자 반응부는 마이크로 유체라인과의 통합이 용이하여 액상과 기상에 모두 접합하다. 그러나 이전 박막 센서 연구의 재료에 따른 신뢰성 문제는 연구의 발전을 저해하고 있었다.

이 연구를 통해 매우 안정적인 박막 변환 시스템이 개발되었다. 이 플랫폼은 박막 센서와 정전 측정 회로 그리고 압타머 수용기(receptor)를 통합하였다. 특히, 본 연구의 박막센서는 획일화된 센서 제작 공정을 통하여 시스템의 신뢰성을

획기적으로 높였다. 이 제작 공정을 위하여 화학적 반응이 없고, 생체 적합하며 얇은 박막에서도 구조적 안전성을 가지는 질화막 (silicon nitride)을 최초로 이용하였다. 또한, 감광 수지(photoresist)를 이용한 희생층 공정(sacrificial process)의 개발은 전극의 균일한 간격과 보(dimple)구조의 제작을 가능하게 하였다. 또한 이층 감광 수지 공정은 낮은 잔류 응력의 두꺼운 견고한 전극을 도금으로 제작하기 위하여 개발되었다. 더 나아가 접촉 표면에서 500 μm 깊이에 있는 박막에 특정한 모양의 금 반응표면을 정교하게 증착하기 위하여 자가조립 근접 섀도우 마스크(shadow mask)가 개발되었다. 마지막으로 CMOS 통합을 고려하여 전체 공정은 표준 저온 공정으로 설계되었다.

개발된 박막 형 화학기계변환 집합체(array)의 센서 시스템을 통해 공통 모드 제거(common mode rejection)기술을 구현하였다. 이를 통해서 화학기계변환의 주요한 환경적 요인인 수압, 온도 변화, 그리고 비특이적 화학결합 등의 외란(disturbance)을 효과적으로 제거하였다. 박막 센서의 평행 전극은 매우 민감한 차등 정전용량 회로의 기계적 센서에 연결되어 있다. 그 변환기의 신호는 P-spice 시뮬레이션을 통해서 효과적으로 상용화된 정전용량 디지털 변환기(Capacitance-to-digital converter) 적용되었다. 그 변환기에 저장된 신호는 윈도우 그래픽 사용자 인터페이스의 제어를 통해 마이크로 프로세서와 다중통신장치에 전달된다. 그래픽 사용자 인터페이스는 C# 언어로 개발되어, 실시간 그래프 표시와 신호 처리 그리고 데이터 기록의 기능을 수행한다. 마지막으로 소형화 박막 변환 시스템을 실현화하기 위하여 인쇄회로 기판이 개발되었다.

이 논문은 박막 화학기계변환 시스템으로 바이오 분자의 측정 가능성을 증명하였다. 특별하게 구상된 DNA 수용체(aptamer) 분자 구조를 통해 트롬빈 단백질의 민감한 감지가 이루어졌다. 11-mercaptoundecanoic acid 분자는 금 반응면에 균일하게 높은

밀도로 부착되어 표면 잡음을 제거하고, 고온 건조의 거친 통합 조건도 견디기에
좋다. 펩타이드 결합을 통한 maleimide 분자는 11-MUA 에 부착되어
티올화(thiolated) 수용체 압타머의 분자 결합 선택비를 높인다. DNA 압타머의 부착
밀도는 박막의 표면 응력을 높이기 위하여 연결 분자의 길이를 조절함으로써
최적화하였다. 더 나아가 분자 화학적 연구를 통해 분자간의 결합시 적절한 완충액을
사용하였다.

이 박막 센서는 전기화학적 영향 없이 완충액 내의 양자를 감지하며, 정량적으로
트롬빈 단백질을 인식할 수 있다. 이중에 500nM 트롬빈의 실험결과로 미세
전극요소 적분방법을 통해 가장 큰 중앙 처짐은 24 nm 으로 계산되었다. 그러나
이는 유한요소해석(ABAQUS)분석에서 예상된 결과보다 3.2~8 배 큰 처짐량으로
단백질의 순전하 (net charge)나 다른 요소의 영향으로 보인다. 추가적인 생화학적
측정을 통하여 이 박막형 화학기계변환 시스템은 질병 진단의 유망한 미래를
지속시킨다.

.....

주요어: 화학기계변환, 박막 변환, 표면 응력, 분자진단, 트롬빈 압타머, 정전용량
측정 센서, 차등측정 시스템

학 번: 2008-30201